Magnetic Polarisation of Palladium in Palladium/Iron Multilayers

Li Cheng
Centre for the Physics of Materials
Department of Physics
McGill University
Montréal, Québec
Canada

A Thesis submitted to the
Faculty of Graduate Studies and Research
in partial fulfillment of the requirements for the degree of
Doctor of Philosophy

© Li Cheng, 2004

Library and
Archives Canada

Published Heritage
Branch

395 Wellington Street
Ottawa ON K1A 0N4
Canada

Bibliothèque et
Archives Canada

Direction du
Patrimoine de l'édition

395, rue Wellington
Ottawa ON K1A 0N4
Canada

Your file Votre référence
ISBN: 0-494-06285-1
Our file Notre référence
ISBN: 0-494-06285-1

NOTICE:
The author has granted a non-exclusive license allowing Library and Archives Canada to reproduce, publish, archive, preserve, conserve, communicate to the public by telecommunication or on the Internet, loan, distribute and sell theses worldwide, for commercial or non-commercial purposes, in microform, paper, electronic and/or any other formats.

The author retains copyright ownership and moral rights in this thesis. Neither the thesis nor substantial extracts from it may be printed or otherwise reproduced without the author's permission.

AVIS:
L'auteur a accordé une licence non exclusive permettant à la Bibliothèque et Archives Canada de reproduire, publier, archiver, sauvegarder, conserver, transmettre au public par télécommunication ou par l'Internet, prêter, distribuer et vendre des thèses partout dans le monde, à des fins commerciales ou autres, sur support microforme, papier, électronique et/ou autres formats.

L'auteur conserve la propriété du droit d'auteur et des droits moraux qui protège cette thèse. Ni la thèse ni des extraits substantiels de celle-ci ne doivent être imprimés ou autrement reproduits sans son autorisation.

In compliance with the Canadian Privacy Act some supporting forms may have been removed from this thesis.

While these forms may be included in the document page count, their removal does not represent any loss of content from the thesis.

Conformément à la loi canadienne sur la protection de la vie privée, quelques formulaires secondaires ont été enlevés de cette thèse.

Bien que ces formulaires aient inclus dans la pagination, il n'y aura aucun contenu manquant.

Canada

To my parents.

Contents

List of Figures

List of Tables

Abstract

This thesis is devoted to the studies of structural and magnetic properties of Pd/Fe multilayers with the principal goal of determining the extent to which the Pd layers are polarised by the Fe atoms and the average moment induced on each Pd atom. Although Pd/Fe multilayers have been the subject of several previous studies, no consensus on the behavior of magnetically polarised Pd has emerged. This work has the novel feature of applying a wide range of characterization techniques on the *same* sample. These techniques included x-ray diffraction, conversion electron Mössbauer spectroscopy (CEMS), magnetometry and polarised neutron reflectometry. Ag/Fe multilayers were first characterized to confirm the validity of the analysis of the small-angle x-ray reflectivity to obtain layer thicknesses, as well as to determine the temperature dependence of the Fe moment from CEMS data.

From the intersection of the results from the complementary measurements on Pd/Fe multilayers, for the first time, an unequivocal understanding of the behavior of magnetically polarised Pd has been achieved. We find, there is a clear excess magnetisation associated with Pd polarisation. At 4.5 K, the Pd in contact with an Fe surface is polarised with an average moment of $0.32 \pm 0.02\ \mu_B$ to a depth of 20 ± 4 Å (9 ± 2 atomic layers). These results indicate a large exchange splitting of the Pd *d*-bands for a significant distance from the Fe surface, leaving the spin-up band full, and a moment in the Pd arising from the 0.36 holes in the spin-down band. We also find that the Fe moment at the Pd/Fe interface is slightly enhanced to $2.42 \pm 0.05\ \mu_B$ for about 2.0 ± 0.3 atomic layers, suggesting that the magnetic properties of Fe is less affected by Pd as compared to the influence of Fe on Pd. Neither the extent of Pd polarisation nor the interface Fe moment agree with values predicted by theoretical calculations (the calculated Pd polarisation depth is 2 atomic layers, and the interface Fe moment is $2.7\ \mu_B$). The band structure calculations will have to be refined in the light of the results from current study.

Résumé

Cette thèse est dévouée à l'étude des structures et propriétés magnétiques du Pd/Fe multicouches, dont le but principal est de déterminer jusqu'à quel point les couches de Pd sont polarisées par les atomes de Fe ainsi que le moment moyen induit sur chaque atome de Pd. Bien que les multicouches Pd/Fe aient fait l'objet de nombreuses études précédentes, il n'y a pas encore de consensus sur le comportement du Pd polarisé magnétiquement. Ce travail propose la nouvelle caratéristique d'appliquer une grande variété de techniques de caractérisation sur le *même* échantillon. Ces techniques incluent diffraction par rayon-X, CEMS, magnétométrie, et PNR. Les multicouches Ag/Fe ont été caractérisées en premier pour confirmer la validité de l'analyse de la reflectivité par rayon-X à petits angles pour obtenir les épaisseurs des couches, ainsi que pour déterminer la dépendence des moments de Fe à partir des données CEMS.

À partir des résultats des mesures complémentaires sur les multicouches Pd/Fe, la compréhension non-équivoque du comportement du Pd polarisé magnétiquement a été atteinte pour la première fois. Nous avons trouvé qu'il y a un clair excès de magnétisation associée avec la polarisation du Pd. À 4.5 K, le Pd en contact avec la surface de Fe est polarisée avec un moment moyen de 0.32 ± 0.02 μ_B jusqu'à une profondeur de 20 ± 4 Å. Ces résultats indiquent un dédoublement d'échange complet des bandes-d du Pd à une distance significative de la surface de Fe, laissant la bande complétement occupée, et un moment de 0.36 μ_B/Pd associé avec les trous spin-down. Nous avons aussi trouvé que le moment du Fe à l'interface Pd/Fe est légèrement accrue jusqu'à 2.42 ± 0.05 μ_B sur à peu près 2.0 ± 0.3 couches atomiques, suggérant que les propriétés magnétiques du Fe sont moins affectées par le Pd par rapport à l'influence du Fe sur le Pd. À la fois l'extention de la polarisation du Pd et l'interface du moment du Fe ne concordent pas avec les valeurs prévues par les calculs théoriques. Les calculs de structure de bande sont supposés s'améliorer à la lumière des résultats de cette présente étude.

Acknowledgments

First of all, I'd like to express my gratitude to my supervisors, Professors John O. Ström-Olsen and Zaven Altounian, for their continued support and enlightening guidance throughout my graduate studies in McGill.

I am indebt to Dr. Zin Tun at NPMR, NRC, Chalk River, for his assistance and helpful discussion during the polarised neutron reflectivity (PNR) measurements. I am also thankful to NPMR for allowing me to carry out the PNR measurements.

I appreciate for the help I have received from the professors in the department of Physics. In particular, I would like to thank Professors Dominic H. Ryan for insightful discussions on the magnetometry, conversion electron Mössbauer microscopy, polarised neutron reflectivity data, and the phenomena of two-dimensional ferromagnetism. I would like also thank Professor Mark Sutton for his valuable help in x-ray reflectivity and polarised neutron reflectivity analysis. I am also grateful to Frank Van Gils, Robert Gagnon, and Steve Kecani for their technical support, and Paula Domingues, Diane Koziol, Louise Decelles, Elizabeth Shearon, Sonia Vieira, Joanne Longo, Lynda Corkum for their help in administrative matters.

I express my special thanks to Dok Won Lee, who introduced me to the sample preparation and characterization techniques of thin films, and Dr. Alex Kuprin, who introduced me to the technique of applying conversion electron Mössbauer spectroscopy to the study of thin films. I also thank Yanzhang Liu, Xiaobin Zhu, Randa Abdouche, Mary Dikeakos, Xubo Liu and two previous members of Prof. Robert W. Cochrane's research group at l'Université de Montréal, Meng Cai, and Veres Teodor, for their help in my experiments and fruitful discussions on the theories of magnetism and analysis of experimental data. I also sincerely thank Romain Stomp for translating the abstract to French.

I appreciate the friendship and help of all the fellow graduate students Ying Huang, Yali Wu, Hong Zhu, Huabin Wang, Yan Sun, Yongfan Zhang, Yi-ting Huang, Manuel Pumarol, Hatem Mehrez, Devrim Guclú, Chao-cheng Kuan, Quanyong Wang, Yi Liu, Ping Yang, Yi Sang, Wengang Lu, Na Wang, Andrei Fluerasu, Khosrow Hassani, Saeid Asgharizadeh, and all the rest.

Finally, I would like to thank my family for their support throughout the years of my study, especially my husband, Yongsheng Chen, for his encouragement and valuable help.

1

Introduction

This thesis is devoted to the study of the magnetic properties of metallic multilayers incorporating interfaces of ferromagnetic Fe with nonmagnetic Ag and strongly exchange-enhanced paramagnetic Pd.

A multilayer or superlattice is an artificial structure composed of alternating layers of two or more different materials or their alloys. The dimension of the layers is in the nanometer range. The wide range of novel and exotic physical properties exhibited by multilayers compared to bulk systems are promising for technological applications. These applications include high-critical-current superconductors[1], mirrors for soft x-rays[2] and neutrons[3], magneto-optical recording materials[4], and magnetoresistive heads[5]. A considerable effort has been dedicated to tailor structures with specific properties. Giant magnetoresistance (GMR) has been a particularly intriguing topic in recent years due to its application in magnetic recording head for information storage systems.

Scientific research on magnetic thin films is motivated by the fundamental magnetic phenomena associated with the surface, interface and low-dimensionality. The lively interplay between theory and experiment is mainly focused on three questions: 1) ground state magnetic moments; 2) spin-wave properties; 3) surface magnetic anisotropy.

At surfaces and interfaces, the ground state moment of a ferromagnet is expected to be modified from its value in the bulk. Theoretical calculations[6, 7, 8] suggest that the ground state moment is enhanced at the surface of magnetic transition metals. The enhancement in the moment is commonly explained as a consequence of the reduction in the coordination number and symmetry, which leads to narrowing of the *d*-band and an enhanced paramagnetic state density at the Fermi level. At the interface of a ferromagnetic metal with a nonmagnetic metal, the hybridization between the *d*-band of the magnetic metal and the *sp* conduction electron band and the *d*-band of the nonmagnetic metal also plays an important role in the interface magnetism. The hybridization in general tends to diminish the moment. With the advances in the theoretical and numerical methods, the theoretical prediction on the surface and interface moment is now considered to be physically meaningful. However, these calculations have not been experimentally proven since determining the atomic moment at surfaces and interfaces is still a challenging problem.

Among the studies of interface magnetism, Ag/Fe and Pd/Fe have received particular attention since they represent two extreme cases. The Ag/Fe is a relatively simple system with a sharp interface and no induced moment in the Ag layer, while in Pd/Fe there is a substantial induced moment in Pd.

Ag/Fe is a close approximation to a two-dimensional (2D) system due to the following unique properties. Ag/Fe has well-defined interfaces because there is no interdiffusion and also a high degree of epitaxy. The strong de-mixing tendency between Ag and Fe due to the large positive heat of mixing in the solid and liquid phases[9] makes Ag and Fe nearly immiscible. It has also been found that Fe(110) films grow epitaxially on Ag(111) films[10], while Fe(100) films grow epitaxially on Ag(100) films[11]. The latter system is particularly favorable for epitaxial growth. This is because the lattice constants of *bcc* α-Fe and *fcc* Ag differ by a factor of nearly $\sqrt{2}$, so that an almost perfect registry (0.8% mismatch) of the two surface nets is produced after a 45° rotation about the surface normal[12]. Furthermore, the epitaxial growth of Fe on Ag proceeds in a nearly layer-by-layer fashion. Last, according to band structure calculations[13, 14], there is only a small degree of band hybridization between Ag and Fe, thus the 2D magnetism of Fe is expected to be mostly unaffected by the presence of Ag.

There is a wide range of intriguing properties obtained in experimental investigations of the Ag/Fe system. First of all, the ground state moment of Fe atoms at Ag/Fe interface was found to be enhanced as compared to the bulk value of 2.22 μ_B. Bland and *et al.*[15] carried out polarized neutron reflectivity (PNR) and ferromagnetic resonance (FMR) studies on epitaxial Fe films prepared by molecular-beam epitaxy (MBE) on Ag(001) substrates. By fitting the neutron spin asymmetries measured at temperatures below 20 K, an average magnetic moment of 2.58 ± 0.09 μ_B was obtained for a Ag/Fe$_{5.5\ \mathrm{AL}}$ structure, where AL represents atomic layer. This moment is significantly enhanced from the value of 2.33 ± 0.05 μ_B determined for a Ag/Fe$_{10.9\ \mathrm{AL}}$ reference sample. The moment ratio between these two samples was found to be 1.06 ± 0.02 by FMR measurement at 77 K, which was in agreement with the ratio of 1.11 ± 0.04 yielded by PNR. This study provided evidence of an increase in moment with reduced Fe thickness, implying that the moment of Fe atoms at the interface was enhanced. Wooten *et al.*[16] performed SQUID magnetometry measurements on 1 – 5 AL of Fe(100) films epitaxially grown on Ag(100) substrates by electron beam evaporation. The interface moments were found to be enhanced as much as 29%. Nevertheless, this value is more than twice higher than that predicted by an *ab inito* calculation[17] (2.52 μ_B, corresponding to 14 % enhancement).

There have been numerous ^{57}Fe Mössbauer spectroscopy investigations of Ag/Fe system, because Mössbauer spectroscopy provides the most direct information of the magnetism at the Fe site. This information includes: the hyperfine field and its temperature dependence, the orientation of the magnetic moment, and the magnetic state (magnetically ordered or paramagnetic). The hyperfine field (B_{hf}) has been traditionally used to obtain the magnetic moment for the bulk material since B_{hf}, to a good approximation, scales with the moment with a single scaling factor. However, at a surface[6] or interface[17, 18], the contributions to the B_{hf} are different, and B_{hf} no longer scales with the moment the same way as in bulk. As a result, the B_{hf} can not be simply converted to a magnetic moment. However, it has been shown for molecular-beam-epitaxy(MBE) deposited thin films[19, 20] that the B_{hf} scales with the moment the same way at different temperatures, so that B_{hf} still measures the temperature dependence of the moment. For those sputtering-deposited multilayers with larger interfacial roughness, the validity of this rule is in question. This question was first answered in this thesis using Ag/Fe multilayers.

The second system, Fe-Pd, is of particular interest because the magnetic properties of palladium are so fascinating. Palladium is isoelectronic with nickel and is an "incipient ferromagnet"[21, 22]. Although the free palladium atom is nonmagnetic with a $4d^{10}5s^0$ configuration, in a metallic environment the palladium $4d$-band is not entirely filled, which gives rise to an anomalously large (enhanced) paramagnetic susceptibility (Pauli susceptibility)[23]. In fact, theoretical calculations predict an onset of an ordered moment in fcc Pd simply by expanding the lattice by 5 – 6 %[24, 25, 26]. This last result can be understood as a consequence of enhanced repulsive intra-atomic Coulomb interactions resulting from the increase in atomic volume. However, experimental attempts to induce ferromagnetism in Pd by growing Pd on Ag and Au to expand the lattice of Pd[27, 28, 29] have failed, even though the Pauli susceptibility of Pd was found to be significantly enhanced[27].

A particularly interesting and much studied property is that a long-range polarisation of the Pd d-band is seen in Pd alloys with dilute solute atoms of Mn, Fe, Co and Ni[30, 31, 32, 33]. The magnetization in these dilute alloys is far too large to be due to the impurity alone[34, 35] implying that the solute atom polarises the surrounding Pd atoms to form what is known as a "giant moment" associated with impurity atoms. In very dilute alloys, where the overlap between giant moments is minimal, the total moment for a polarised cloud may be as much as $\sim 10\ \mu_{\mathrm{B}}$[30, 36, 37], with an average on the Pd atom of 0.05–0.4 μ_{B}[30, 38, 39]. However, the spatial extent of the polarisation cloud has never been clearly established. Ascribing the onset of long-range ferromagnetic order to the formation of a percolating network implies a giant moment radius of ~30 Å[32]. However, assuming Pd carries a moment of 0.1–0.3 μ_{B}/atom (values taken from concentrated Pd-Fe alloys[40, 41]), a uniform, maximally polarised cloud would have to extend no more than 5–10 Å from the central impurity to account for the observed $\sim 10\ \mu_{\mathrm{B}}$ cloud moment. To add to the confusion, direct determination from small angle neutron scattering yields values ranging from 10 Å[39, 42, 43] to 50 Å[44]. While these scattering-based estimates of the cloud's extent have been questioned[45], band structure calculations confirm that many hundreds of Pd atoms should be polarised[46].

The wide range of estimates for both the size and amplitude of the polarisation cloud reflects the experimental difficulty associated with extremely dilute random alloys. For example, the small-angle neutron scattering signal is weak, and necessarily contains contributions from many dynamic and static disorder sources. The problem may be greatly simplified by studying Pd/Fe multilayers (where the materials involved are pure metals) rather than dilute $\underline{\text{Pd}}$Fe alloys. The magnetic behavior will be simpler as the Pd is in contact with bulk-like, ferromagnetically ordered iron layers rather than isolated, randomly ordered Fe impurity atoms.

Experimental investigations on Pd/Fe thin films and multilayers have given both qualitative[47, 48, 49, 50, 51] and quantitative[15, 52, 53, 54, 55] evidence of polarisation of the Pd atoms in close proximity to the Fe interface. However, no consensus on either the iron moment at the Pd/Fe interface or the extent and magnitude of the magnetic polarisation in the Pd layers has emerged. Most studies[15, 52, 53] only provided mixed information about total enhancement in the moment relative to that of bulk Fe. The enhancement includes the contributions from Pd polarisation and enhanced interface Fe moment as suggested by theoretical calculations[56, 57, 58, 59]. Only a few studies[55, 60] have attempted to provide values for the interface Fe moment and Pd polarisation independently. Using an indirect measurement, magnetic circular x-ray dichroism (MCXD), Vogel *et al.*[55] and Le Cann *et al.*[60] determined that the Pd and Fe at the Pd/Fe interface had a moment of 0.38 ± 0.08 μ_{B}/Pd atom and 2.7 ± 0.2 μ_{B}/Fe atom respectively. MCXD measures the absorptions of left and right circularly polarised x-ray at inner shell absorption edges in magnetic materials, and the moments were obtained using MCXD sum rules[61]. The sum rules, derived from a single ion model, state that the integrated absorption cross-section over the absorption edges relates to the ground-state expectation values of orbital, spin and the spin dipole of the valence electrons[61]. However, application of the atomic sum rules to determine accurately the moment at surfaces or interfaces of transition metals is still controversial due to theoretical ambiguities and experimental difficulties[62].

The range of Pd polarisation has been given as anywhere from 1 to 4 atomic layers(AL) from the interface[50, 51, 52, 55], while theoretical calculations made on an Fe overlayer on semi-infinite Pd(001)[56] and Pd atomic layers on semi-infinite Fe(001)[57] suggest that only the first 1 – 2 AL (1 AL of Pd(001) = 1.9 Å) of Pd near the interface should be polarized. These experimental and theoretical values of the extent of polarisation into Pd layers are surprisingly shorter than the size of the polarisation cloud in Pd alloys. In addition, most experimental studies mentioned above were carried out at room temperature, at which the Pd polarisation effect is very weak as will be shown in our study. Further investigation at low temperature is required if clear results are to be obtained.

In the thesis, we started with the Ag/Fe system. The bilayer thicknesses of four samples obtained from analysis of the small-angle x-ray reflectivity data were compared to the results from transmission electron microscopy (TEM) studies. The hyperfine field and magnetisation of multilayer $[\mathrm{Ag}25\ \text{Å}/\mathrm{Fe}10\ \text{Å}]_{25}/\mathrm{Ag}\ 25\ \text{Å}$ were measured as a function of temperature using CEMS (conversion electron Mössbauer spectroscopy) and magnetometry measurements respectively, and compared to each other. We address two problems: 1) if the bilayer thickness obtained from analysis of the small-angle x-ray reflectivity data is reliable; 2) if the variation of hyperfine field still measures the temperature dependence of the Fe moment in the sputter-deposited multilayers.

Then we attacked the more challenging problem, Pd/Fe multilayers, using a series of complementary structural and magnetic measurements all carried out on the same samples. Layer thicknesses and crystalline orientations were obtained from analysis of small-angle and high-angle x-ray diffraction data. The Pd polarisation and its temperature dependence were obtained by combining data from CEMS, magnetometry and PNR measurement. First, the CEMS was employed to determine the interface

Fe thickness and the temperature dependence of the Fe moment. Then the Fe contribution was removed from the total moments, measured by the magnetometer, to give the temperature dependence of the Pd polarisation. Last, we used PNR to probe the magnitude and depth of the induced polarisation in the Pd layers at both room temperature and 4.5 K. PNR measurements were used since neutrons interact with both nuclei and the atomic moments so that they map the nuclei as well as the existing magnetic profile. The important feature of the PNR study is that multilayer samples grown with carefully matched Pd and Fe layer thicknesses were used, which minimise the contributions from chemical structure to the even-order superlattice reflections and greatly enhance the sensitivity to Pd polarisation effects. Taken in isolation, no single measurement can yield an unequivocal understanding of Pd/Fe moment; taken together, a clear conclusion emerges. For the first time, we are able to answer the following questions with confidence: 1) what are the magnitude and the extent of the Pd polarisation; 2) how does the Pd polarisation vary with temperature; 3) what is the magnitude of the interface Fe moment.

The thesis is organized as follows: In Chapter 2, the theoretical background of magnetism of atoms and solids in general, and magnetic properties of Ag/Fe and Pd/Fe multilayers in particular are introduced. In Chapter 3, the experimental methods for sample preparation and characterization are described. Chapter 4 presents the data and analysis for x-ray diffraction, TEM, magnetometry and CEMS studies on Ag/Fe multilayers. In Chapter 5, the results of Pd/Fe moments, studied using CEMS, magnetometer, and PNR, are presented, The conclusions of this thesis as well as some proposals for future studies are included in Chapter 6.

2

Theoretical Background

A ferromagnetic thin film is an artificial material whose magnetic properties are strongly dependent on the dimension of the magnetic entity, the structural properties and the material in contact. The literature about a variety of two-dimensional magnetic phenomena and the underlying physical principles is vast. This chapter is limited to a brief introduction of the origin of magnetic moment and magnetic ordering in general, and the ground state moment of Fe at the two-dimensional interface in proximity to Ag and Pd, and the polarisation of Pd in particular.

2.1 *Magnetic Phenomena and Ferromagnetism*

A magnetic material often exhibits long-range magnetic order below a certain critical temperature, which is called the Curie temperature when the ordering is ferromagnetic. Above this critical temperature, thermal energy overcomes the exchange interaction, and the magnetically ordered substance becomes magnetically disordered, and behaves like a paramagnet.

The magnetic moment of an atom originates from the electrons and nuclei. However, since the mass of nuclei is much larger than that of electrons, the nuclear magnetic moments are usually negligible. The atomic moment is thus mostly attributed to the orbital motion and spin of electrons, and the electrons are the carriers of magnetism. According to quantum mechanics, the electrons move in orbitals, each of the orbitals is characterized by a specific energy and spatial distribution. The electron also has an intrinsic spin angular momentum. The orbital and spin angular momenta lead to a magnetic moment. Since the components of the orbital angular momentum and spin angular momentum along a specified direction, usually that of an applied magnetic field, are quantized, so also is the moment.

An atom or ion with all electronic shells filled has zero spin and orbital angular momentum in its ground state, so that its moment is zero. The quantum numbers of angular momenta can be determined for a free atom or ion at ground state with unfilled shells using Hund's rules. The atomic magnetic moment can be obtained thereafter.

In magnetically ordered substances, i.e., ferro-, antiferro-, and ferrimagnet, not only the atoms or ions carry magnetic moment, but also the moments in general tend to be aligned parallel or antiparallel. Collective magnetic interaction is indispensable for the magnetic ordering, since without the interaction, the individual magnetic moments would be thermally disordered and point in random directions in the absence of an externally applied field. It was first thought that the magnetic interaction would be the direct dipolar interaction between the magnetic moments. However, the direct dipolar interaction energy of two magnetic dipoles is a few orders of magnitude smaller than the electrostatic energy differences between atomic states. Moreover, the electrostatic energy of a pair of magnetic ions of a certain state depends on the relative direction of their moments in that state, as a result of Pauli exclusion principle. The most important source of magnetic interaction is the ordinary spin-independent Coulomb interaction. The contributions to the energy arising from Pauli principle may be regarded as caused by two-body spin-spin interactions, and the Hamiltonian is given by $H = -\sum_{ij} J_{ij}\mathbf{S_i}\cdot\mathbf{S_j}$, where $\mathbf{S_i}$ and $\mathbf{S_j}$ are the spin operators of the localized spins on site i, and j, and J is the exchange integral. This is known as Heisenberg exchange model, which is defined for localized electrons that interact only weakly. According to this localized electron model, positive J favors ferromagnetism, while negative J favors antiferromagnetism. This model successfully explains the origin of ferro- and antiferromagnetism in many insulating components.

For the first transition metal series ($3d$ system) ions or atoms, the magnetic moment has an almost spin-only value[63] of effective moment of $\mu_{eff} = g\sqrt{S(S+1)}\mu_{\mathrm{B}}$, or saturation moment of $\mu_{sat} = gS\mu_{\mathrm{B}}$, where S is the total spin quantum number, g is the gyromagnetic ratio, and $g = 2$ for spin motion, μ_{B} is Bohr magneton. This is a result of the almost complete quenching of orbital angular momentum due to crystalline electric field. The crystal field is the non-central and nonuniform electrostatic field from neighboring atoms or ions in the crystal environment. For the ions of the first transition series (3*d* system) in an insulating solid, the theoretical values for the moments with S determined using Hund's rules are in excellent agreement with experimental values. In the metallic form, however, the moments are not integers as determined by Hund's rules. For example, the three ferromagnetic elements Fe, Co, and Ni exhibit saturation magnetic moments of 2.2, 1.7, and 0.6 μ_{B} respectively, in contrast to spin magnetic moments of 4, 3, and 2 μ_{B} respectively. This discrepancy led to a different model: itinerant-electron theory.

Itinerant-electron theory is the band theory when applied to the field of magnetism. It is the main stream of theory of magnetism and is widely used to predict or interpret the magnetic properties of new magnetic materials, such as magnetic surfaces, superlattices, alloys and etc. Itinerant theory assumes that the *d* and *s* electrons are not completely localized at atoms, but instead are able to move (or be itinerant) in a crystal lattice and form a band structure. The band structure and the density of state (DOS) of electrons as a function of energy $\mathrm{N}_\sigma(\mathrm{E})$ can be calculated using band theory. A simplified spin-up and spin-down electron energy bands are shown in Fig. 2.1. The electrons fill the energy band up to the Fermi energy level (ϵ_{F}), and their numbers are given by,

$$\mathrm{n}_\sigma = \int_{-\infty}^{\epsilon_{\mathrm{F}\sigma}} \mathrm{N}_\sigma(\mathrm{E})\mathrm{dE}. \tag{2.1}$$

The magnetic moment μ is given by the imbalance between the number of electrons in the spin-up and spin-down *d*-bands, i.e.,

$$\mu = (n_\uparrow - n_\downarrow)\mu_B, \tag{2.2}$$

in which n_σ is the number of electrons with spin σ, and ↑ and ↓ represent spin-up and spin-down respectively. μ is not necessarily an integer.

The occurrence of the ferromagnetism can be explained using a phenomenological model. At T = 0 K, and in zero field, without exchange interactions between electrons, the energy bands for the two spins are symmetrical and $n_\uparrow$ is equal to $n_\downarrow$, so that the net magnetization is zero. If taking the positive exchange interaction between the electrons into account, which is equivalent to a positive internal magnetic field, the energy of spin-up electrons is reduced while the energy of spin-down electrons is enhanced. The energy bands are exchange split by a small energy δE. At ϵ_F, the electrons in energy range of δE is removed from spin-down band and added into spin-up band. The number of electrons is not the same for the two spins any more, which gives rise to a non-zero magnetization.

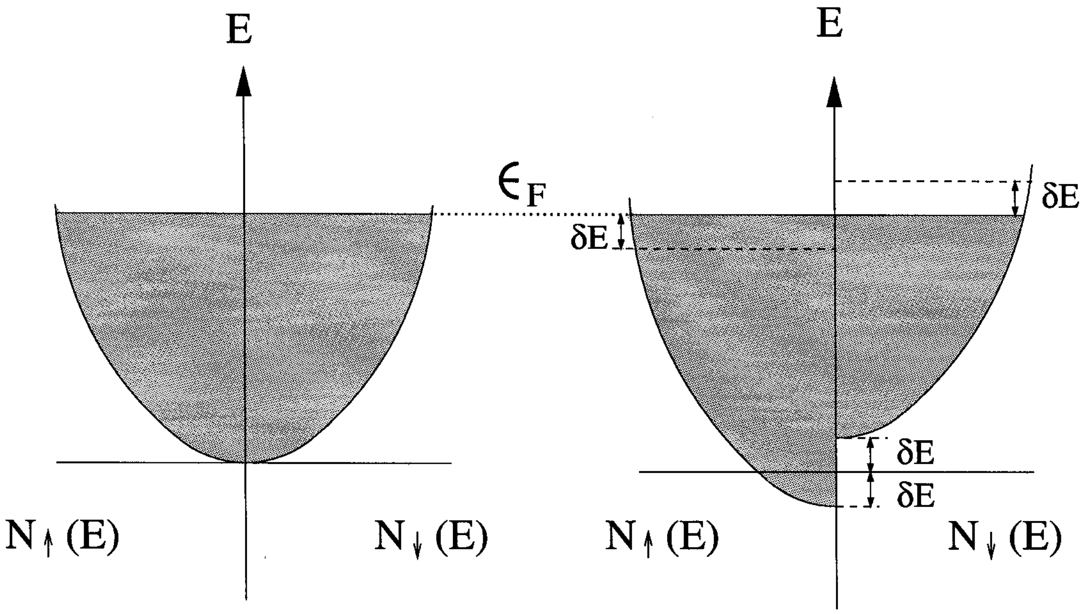

Figure 2.1: Density of state of spin-up electrons ($N_\uparrow$) and spin-down electrons ($N_\downarrow$), a) without exchange interaction; b) with exchange interaction.

A spontaneous ferromagnetic (FM) state occurs if the state with split energy bands is stable. Upon splitting the energy bands by δE, the kinetic energy is enhanced by

$$E_k = N(\epsilon_F)\delta E \cdot \delta E = N(\epsilon_F)(\delta E)^2, \tag{2.3}$$

where $N(\epsilon_F)$ is the density of states at Fermi energy for one spin state without exchange splitting. The change in the exchange energy is

$$E_{ex} = V\left(\frac{n}{2} + N(\epsilon_F)\delta E\right)\left(\frac{n}{2} - N(\epsilon_F)\delta E\right) - V\frac{n^2}{4} = -VN^2(\epsilon_F)(\delta E)^2 \quad (2.4)$$

where V is an effective exchange potential between the electrons, and $n = n_\uparrow + n_\downarrow$, is the total number of electrons in the energy bands. The resultant change in the total energy is

$$\Delta E = N(\epsilon_F)[1 - VN(\epsilon_F)](\delta E)^2. \quad (2.5)$$

FM state requires $[1 - VN(\epsilon_F)] < 0$, i.e., the split state has lower energy. This is called Stoner condition for FM state. This suggests that FM state is favored in systems with strong exchange potentials and large $N(\epsilon_F)$.

In the non-FM state, the susceptibility χ is given by

$$\chi = \frac{\chi_p}{1 - VN(\epsilon_F)}, \quad (2.6)$$

in which $\chi_p = \mu_B{}^2 N(\epsilon_F)$ is the unenhanced Pauli susceptibility, and $[1 - VN(\epsilon_F)]^{-1}$ is called Stoner exchange enhancement factor.

The calculated electronic densities of states of ferromagnetic Fe, Co and Ni are characterized by a broad and unpolarised 4*s*-band superposed on a spin-split 3*d*-band. The magnetic moment arises from the difference between the spin-up electrons and spin-down electrons in the 3*d*-band. The carriers of the magnetism can also be regarded as the holes in the 3*d*-band. For example, the electronic configuration of Fe atoms in metallic form is $3d^{\uparrow 4.8}3d^{\downarrow 2.6}4s^{\uparrow 0.3}4s^{\downarrow 0.3}$, where ↑ and ↓ denote spin-up and spin-down respectively. There are 0.2 holes in $3d^\uparrow$ band and 2.4 holes in $3d^\downarrow$-band, which gives rise to a spin-only moment of 2.2 μ_B. For these three ferromagnetic elements, the unsplit densities of states exhibit a peak at the Fermi level ϵ_F giving $N(\epsilon_F) > 1$ /atom·eV, and the exchange potential V in the 3*d*-band is $\simeq 1$ eV, so that the Stoner criterion for spontaneous ferromagnetism $[1 - VN(\epsilon_F)] < 0$ is satisfied.

Altough *d* electrons are able to be itinerant in the lattice, they are not as mobile as *s* electrons. For example, in the calculated energy dispersions of Fe[64], one *d*-band is parabolic-like, corresponding to freely itinerant electrons, while the other *d*-bands are very flat, reflecting very large effective electron mass. Electrons with large effective masses are close to being in a localized state. So the d electrons can be divided into itinerant electrons (d_i) and localized electrons (d_l). The calculated $d_i = 0.35$ electrons per Fe atom, while the total d electrons are 7 electrons per Fe atom[65], indicating that the Fe spin moment is very localized. In metals, long-range magnetic ordering is not a result of Heisenberg exchange interaction. Instead, the spins that are localized on separate atoms are considered to be exchange coupled by a small fraction of itinerant electrons. The occurence of ferromagnetism in metals can not be simply determined by the sign of the exchange integral. According to the Stoner citerion, spontaneous ferromagnetism is determined by the competition between the kinetic energy increase and exchange energy reduction due to spin band splitting (moment formation).

2.2 Magnetic Properties of Ag/Fe and Pd/Fe Thin Films

Magnetic surfaces and interfaces are a special group of magnetic system characterized by low-dimension and reduced symmetry. There are a wide range of novel properties found in $3d$-metals related to surface magnetism, which were not found in bulk materials. In this section, the ground state moment of Fe at Ag/Fe and Pd/Fe interfaces, and the unique properties of Pd are discussed qualitatively in the light of density of states from band structure calculations by S. Ohnishi and *et al.*[17] and Huang and *et al.*[58].

2.2.1 Enhanced Fe Moment at Fe Surface and Ag/Fe Interface

In general, the magnetic moment of atoms at a surface or interface in proximity with non-magnetic metals is affected by at least two factors[66]. One factor is the coordination number[66], or number of nearest neighbours. For the same system, the magnetic moment increases with decreasing coordination number. As an example, an Fe atom in the bulk has 8 nearest neighbors. At clean Fe surfaces, the number of neighbors is reduced to 6 and 4 for Fe(110) and Fe(100) structures respectively.

According to the calculations by Ohnishi *et al.*[6] and Fu *et al.*[8], the moment at the Fe surfaces of both structures is enhanced relative to the bulk value of 2.22 μ_B, and Fe(100) surface has higher moment of 2.98 μ_B[6] as compared to Fe(110) surface moment of 2.65 μ_B[8]. For an unsupported Fe(100) monolayer, which has two free surfaces, the moment further increases from the Fe(100) surface value to 3.2 μ_B[17]. This occurance can be explained as that the Fe atoms with lower coordination number have less overlap with neighbouring atoms, so that the *d* states become more localized and atomic-like. As a consequence, the intra-atomic exchange is more effective and the exchange splitting can be larger, which strengthens the conditions for moment formation at the surface, and in turn enhances the magnetic moment. The localization of the *d*-band is also reflected by the narrower *d*-bands in the Fe layers with reduced coordination as compared to those of bulk Fe.

According to the band structure calculation by S. Ohnishi *et al.*[17], when Fe(100) surface is covered by a Ag layer, the electronic structure is neither bulk-like, nor surface-like. The surface *d* states found in clean Fe surface[6] are still present at the interface. However, the surface states at interface are not as localized as they are for the clean surface, since the Ag atoms provide an increase of overlap for the surface *d* states. On the other hand, at the interface although Ag seals the Fe surface, Ag does not have the same effect of reimposing the bulk conditions as Fe itself does. As a result, the Fe layer at the interface has a moment of about 2.5 μ_B, which is lower than the clean Fe(100) surface moment of 2.98 μ_B[6], but still about 10% higher as compared to the bulk Fe value.

Another factor affecting the magnetic moment at the interface is the hybridization between the *d*-band of the magnetic metal and *sp* conduction electron band[66] and *d*-band[14] of the non-magnetic metal, which in general tends to lower the moment at the interface. The $d-d$ coupling between Ag and Fe is very small since the *d*-bands of Ag and Fe are very narrow and hardly overlap[14]. The Ag(*sp*)-Fe(*d*) coupling is also small since Ag has relatively low *sp*-conduction-electron density[14]. In the Ag/Fe system, the factors suppressing the magnetic moment do not exsist.

There have been experimental evidences for enhanced Fe moment at Ag/Fe interface. For example, the PNR study by Bland and *et al.*[15] has shown that a Ag/$\mathrm{Fe}_{5.5\ \mathrm{AL}}$ structure has an average moment of 2.58 ± 0.09 μ_{B}, significantly enhanced from the value of 2.33 ± 0.05 μ_{B} determined for a Ag/$\mathrm{Fe}_{10.9\ \mathrm{AL}}$ Fe reference sample. They also found that the moment ratio between these two samples was 1.06 ± 0.02 by FMR. The fact that moment increased with reduced Fe thickness implied that the moment of Fe atoms at the interface was enhanced. The interface moment of Fe was found to be enhanced by as much as 29% by Wooten *et al.*[16] when they studied Fe(100) films epitaxially grown on Ag(100) using SQUID magnetometry measurements.

2.2.2 Unique Magnetic Properties of Pd

Pd is isoelectronic to Ni and has the same lattice structure as Ni. Also due to its unusually large exchange enhanced paramagnetic susceptibility, Pd is regarded as an "incipient ferromagnet"[21, 22]. In their pure atomic configuration $4d^{10}5s^{0}$, free palladium atoms are nonmagnetic. However, in a metallic environment the palladium $4d$-band turns out to be not entirely filled. The band structure calculation by F. M. Mueller *et al.*[22] has suggested that Pd has 0.36 holes in the $4d$-band, which is in excellent agreement with the de Haas-van Alphen measurements of Vuillemin and Preistly[67]. F. M. Mueller *et al.*[22] have also shown that the Fermi energy lies slightly above the maximum in the calculated density of states N(E) as illustrated in Fig. 2.2, and the density of states at Fermi energy $\mathrm{N}(\epsilon_{\mathrm{F}})$ is 1.14 ± 0.08 states per eV. Combining the exchange potential $V = 0.71$ eV for the Pd, which is from a recent calculation[68], the product of $\mathrm{N}(\epsilon_{\mathrm{F}})$ and V is slightly lower than 1. The Stoner condition for FM state is not satisfied, while the Stoner exchange enhancement factor is large. These numbers qualitatively explain the absence of FM ordering in Pd and the anomalously large enhanced paramagnetic susceptibility observed experimentally[23].

Since Pd is near the threshold of becoming FM, various attempts were made to render the FM state in Pd. One is by expanding the lattice constant, since the increase in atomic volume enhances the repulsive intra-atomic Coulomb interactions.

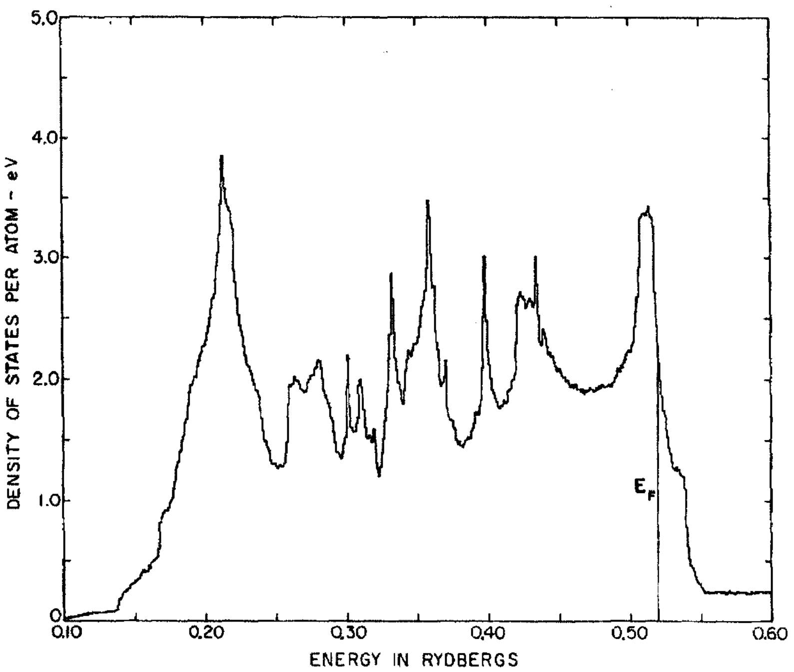

Figure 2.2: Calculated density of states of pure Pd. The unit for the energy is Rydberg(Ry), and 1Ry = 13.606 ev. (after F. M. Mueller *et al.*, *Phys. Rev. B*, 1:4617, 1970.)

Spin-polarized calculations[24, 25, 26] have found an onset of magnetic behavior upon 5 – 6 % (10 % when spin-orbit interaction was included) expansion in the lattice constant. However, these predictions have not been proved experimentally. No induced ferromagnetism in Pd has been achieved by growing Pd on Ag and Au to expand the lattice of Pd[27, 28, 29], although the Pauli susceptibility of Pd was found to be significantly enhanced[27].

On the other hand, long-range polarisation of the Pd *d*-band has been seen in a large number of experiments on Pd alloys with dilute solute atoms of Mn, Fe, Co and Ni[30, 31, 32, 33]. The magnetization in these dilute alloys is far too large to be due to the impurity alone[34, 35], implying that the solute atom polarises the surrounding Pd atoms. Electronic structure calculation[46] yielded a picture of the long-range polarization of Pd by local moments of 3*d* impurities, suggesting that many hundreds of Pd atoms should be polarised.

There is also experimental evidence of ferromagnetism in Pd at the two-dimensional interface incorporating Pd with ferromagnetic materials[15, 47, 48, 49, 50, 51, 52, 53, 54, 55]. Several theoretical calculations about the electronic structures at the interface between Pd and Fe claim to account for the Pd polarisation and enhanced Fe moment via $3d - 4d$ band hybridization. For example, Huang *et al.*[58] used a spin-polarized self-consistent localized-orbital (SCLO) calculation to study a free Pd(100) atomic layer with Fe lattice constant, a 5 AL Fe(100) slab(Fe_5) simulating the clean substrate, and a thin film consisting of 3 AL of Fe sandwiched by Pd atomic layers ($Pd/Fe_3/Pd$). The layer-resolved DOS of these three systems was used to illustrate the hybridization effect between Pd and Fe.

The calculated DOSs of the free Pd atomic layer and Fe_5 are given in Fig. 2.3. For the free Pd atomic layer(Fig. 2.3 (a)), not only the shape of the DOS is different from that of pure Pd, but also the majority-spin and minority-spin states are exchange split, resulting in a magnetic moment of 0.36 μ_B. The narrower band of Pd atomic layer with respect to that of bulk Pd and wavefunction localization account for this FM state in Pd. As shown in Fig. 2.3 (b), the main feature in surface DOS of Fe_5 is different from that of interior planes, while the interior planes have DOSs resembling those of bulk Fe, indicating the surface states are very localized.

As to the $Pd/Fe_3/Pd$ sandwich (Fig. 2.4 (a)) it can be seen that DOSs for the majority-spin and minority-spin of Pd cover layer become considerably different to those of the free Pd monolayer, and the DOS of surface Fe layer is also modified while being covered by a Pd layer. Moreover, as shown in Fig. 2.4 (b), the DOSs of Pd cover layer and first Fe layer overlap strongly in the majority-spin band, but not in the minority-spin band. It follows that a new mutual Pd-Fe state is developed at Pd/Fe interface via hybridization between majority spin electrons. This new state attributes to the interface magnetic properties of the $Pd/Fe_3/Pd$ sandwich.

The layer-resolved moments of Pd and Fe are listed in Table 2.1. The Pd cover layer has a moment of 0.37 μ_B, which only differs from that of the free Pd monolayer by 0.01 μ_B. The moment of the Pd cover layer results from Pd-Fe hybridization rather than the reduced coordination, since the DOSs of the Pd cover layer and free monolayer differ dramatically from each other. Hybridization reduces the interface

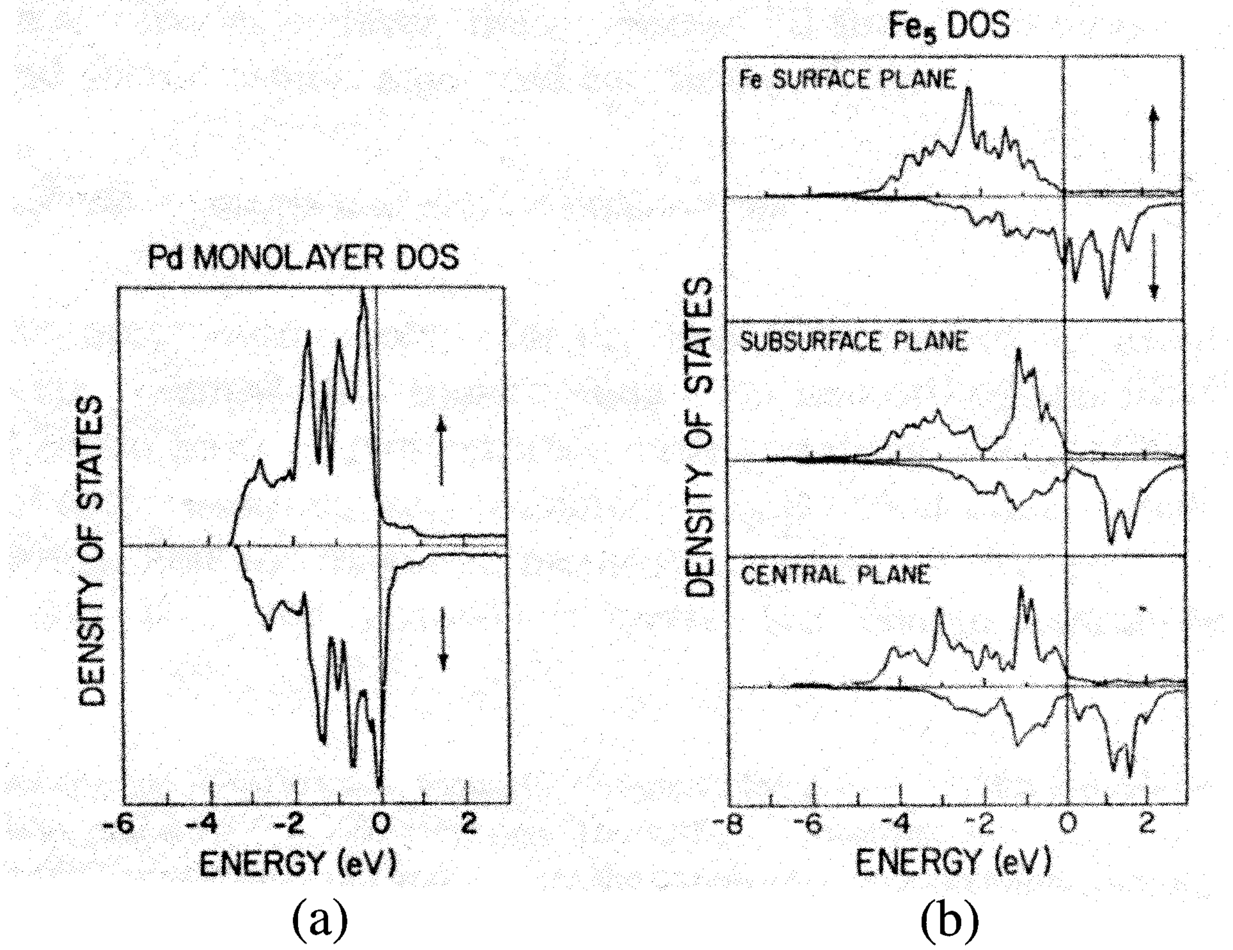

Figure 2.3: Spin and layer-resolved density of states for a) a Pd(100) monolayer; b) a five-plane Fe(100) film. ↑ is for the majority-spin and ↓ is for the minority-spin. ϵ_F is the energy zero. The vertical scale is arbitrary, and differs for a) and b). (after H. Huang *et al.*, *Surf. Sci.*, 172:363, 1986.)

Fe moment from the clean Fe surface, but the interface Fe moment 2.74 μ_B is still significantly larger than the center-plane moment of 2.37 μ_B and the bulk Fe moment of 2.16 μ_B.

The number of atomic layers of Pd which are polarized by Fe is also of interest, since clarifying this problem sheds light on the problem of polarization length into Pd by ferromagnetic impurities. Blügel *et al.*[56] have investigated the electronic structure of a system consisting of 7 AL of Pd(001) covered by an Fe overlayer, and found that an Fe overlayer induced moments of 0.32 and 0.17 μ_B in the first and

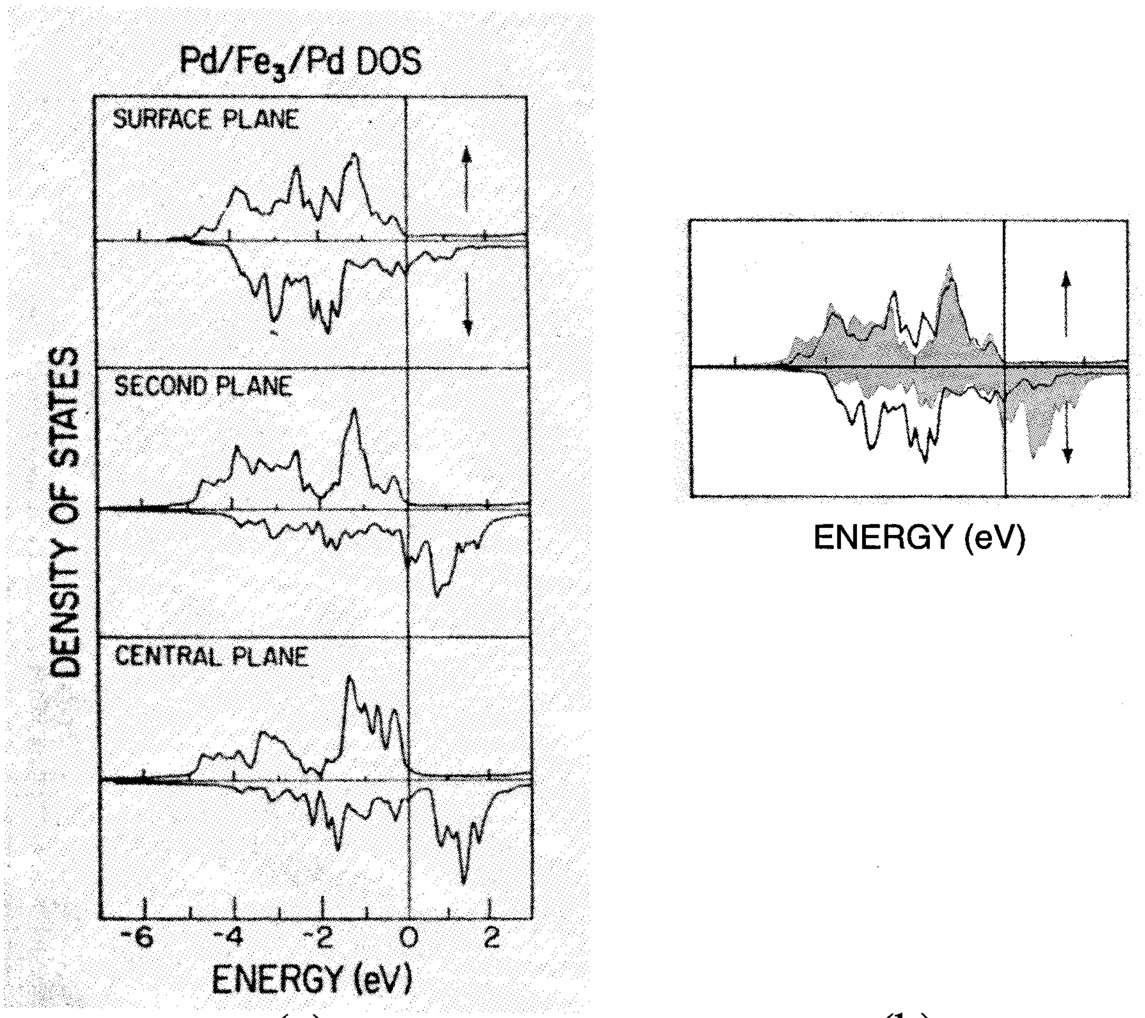

(a) (b)

Figure 2.4: a) Density of state (DOS) for a five-plane Pd/Fe_3/Pd sandwich. b) The DOSs of Pd cover layer (solid line) and first Fe layer (shadowed) superimposed on each other, to illustrate the hybridization between the majority spin electrons. (after H. Huang *et al.*, *Surf. Sci.*, 172:363, 1986.)

Table 2.1: The magnetic moments for a free Pd(100) monolayer Pd_1, a five-plane Fe(100) film Fe_5, and a $Pd/Fe_3/Pd$ sandwich. The surface, subsurface and central layers are labeled S, S−1, and C, respectively. (after H. Huang *et al.*, *Surf. Sci.*, 172:363, 1986.)

Film	Pd_1	Fe_5	$Pd/Fe_3/Pd$
S	0.36 μ_B	2.89 μ_B	0.37 μ_B
S−1	-	2.31 μ_B	2.74 μ_B
C	-	2.49 μ_B	2.37 μ_B

second Pd layers respectively. The Fe overlayer on the Pd slab has a moment of $\sim$ 3.2 μ_B, which is substantially higher than the interface Fe moment of 2.74 μ_B obtained by Huang *et al.*[58]. This could be explained as a result of the lower coordination number of the Fe overlayer, since the moment usually increases with decreasing coordination number. The moment of the Fe overlayer on the Pd slab is also higher than the moment of surface Fe (2.98 μ_B)[6], or the moment of Fe overlayer on Ag (3.0 μ_B)[14], suggesting the enhancement in the Fe moment by Pd in contact.

The theoretical value of the extent of polarisation into Pd layer of 2 AL by Blügel *et al.*[56] is in qualitative agreement with the results by a few experimental investigations[50, 51, 52, 55], but is significantly shorter than the size of the polarisation cloud in Pd alloys. Since most experimental studies mentioned above were carried out at room temperature, at which the Pd polarisation effect is very weak as will be shown in our study, further investigation at low temperature is required to resolve these discrepancies and to determine whether these theoretical calculations are correct or not.

3

Experimental Methods

The Ag/Fe and Pd/Fe multilayers used in this research were prepared using a computer controlled magnetron sputter deposition system. Low-angle x-ray reflectivity, high-angle x-ray diffraction and transmission electron microscopy (TEM) were performed to characterize the multilayers. Magnetometry, polarised neutron reflectivity (PNR), conversion electron Mössbauer spectroscopy (CEMS) measurements were carried out to probe the magnetic properties of the multilayers. The experimental methods of these techniques are described as follow.

3.1 Sputter Deposition

Magnetic thin films are synthesized in vacuum to reduce the concentration of impurities in the deposited films. There are a wide variety of vacuum deposition techniques. According to how the source material is gasified, these deposition techniques are divided into two categories: chemical vapor deposition (CVD) and physical vapor deposition (PVD). CVD, which involves chemically gasified solids as sources, is widely used in industry. Because most of the chemical vapors used to evaporate the source are poisonous or ignites if exposed to air, and contamination involved in deposition, CVD is not often practised in research. PVD includes molecular beam epitaxy (MBE), electron-beam evaporation, laser ablation, and sputtering, during which the source material is evaporated using physical processes. Sputtering is one of the most popular techniques widely used both in research and industry. Many materials, including metals, semi-conductors, or insulators, alloys or compounds, can be deposited at a relatively high rate.

Sputtering deposition employs highly energetic positive ions of a gas to knock off the atoms of a target material. After the evacuation of the deposition chamber, the sputtering gas, usually argon or other inert gas is introduced into the chamber, and a high negative DC voltage is applied to the target material. The sputtering gas is ionized by collisions with electrons. The ions of the sputtering gas, attracted by the cathode, are accelerated toward the target and remove the target atoms by bombardment. The energy of the sputtered target atoms, initially in the range between 2 – 30 eV, is reduced prior to deposition onto the substrate by collisions with the sputtering gas. Good adhesion onto the substrate depends mainly on substrate cleanliness. The structure of the deposited film depends on a variety of factors, such as the sputtering gas pressure (typically from 1 to 100 mTorr), target-substrate distance (typically from a few cm to a few tens of cm), power applied to the targets, substrate material, and temperature. During the sputtering process, a self-sustaining glow discharge, containing reflected ions, electrons and neutral species, is generated. The glow discharge is essentially a plasma, which is a partially ionized gas containing about equal concentrations of positive and negative particles. The characteristics of sputtering is determined by the properties of the glow discharge.

Sputtering can be operated in two modes, DC sputtering and RF sputtering. DC sputtering is used for metallic film deposition, while RF sputtering is used for both metallic and insulating film deposition. Magnetron sputtering is an improved technique operating with both DC and RF modes. In magnetron sputtering, a magnetic field (0.02– 0.05 T) is produced by strong permanent magnets placed underneath the target. The electrons undergo a cyclic motion based on $\mathbf{E} \times \mathbf{B}$ drift so that the glow discharges are confined close to the target and away from substrate. The sputtering gas pressure and cathode voltage are reduced due to the longer mean free path of the secondary electrons under cyclic motion. The advantages of the magnetron sputtering include reduction of damage to the substrate and the film from energetic ion bombardment, and lower residual gas in the thin films.

In this study, two families of Ag/Fe and Pd/Fe multilayers were grown using an

Edwards multifunction deposition system (Fig. 3.1). The system has three magnetron sputtering sources, two of which can be operated simultaneously for the deposition of multilayers containing two different materials, while the third one allows the growth of a capping layer or buffer layer of material different to the ones used for the multilayer. Discs of high-purity materials (99.99 % for Ag and Fe, 99.9 % for Pd) were used as targets. An isolation shield was placed over the targets to avoid intermixing the fluxes of the sputtered atoms. Substrates were mounted on a rotary substrate platform on top of the chamber. The rotation of the substrate platform was controlled by a computer. Deposition rates of the sputtered material were individually measured using a quartz-crystal monitor, and were precisely calibrated using small angle x-ray reflectivity measurement for thickness determination. The layer thicknesses in the multilayers were regulated by computer control of the substrate position and the exposure time.

Prior to sputtering, the chamber was pumped by a cryo-pump and a base pressure of 2.0×10^{-7} Torr was achieved. During deposition, the Ar pressure was 7 – 10 mTorr. The pumping and pressure monitoring procedures are automatically controlled by a microcomputer. For a given material, the deposition rate is controlled by the Ar pressure and the DC power. The deposition conditions of the Ag/Fe and Pd/Fe multilayers are listed in Table 3.1. The typical deposition rates were 0.6 – 3 Å/s. With a typical target-substrate distance of 14 cm and the 3.8 cm diameter target used in the sputtering, the uniformity of the deposition is 5 % or better for a distance of 4 cm from the center of the target.

Table 3.1: Deposition conditions for Ag/Fe and Pd/Fe multilayers. D_{st} is the substrate-target distance, P_{Ar} is the sputtering pressure of argon gas, P_{DC} is the DC power and τ is the deposition rate.

group	D_{st} (cm)	P_{Ar} (Torr)	P_{DC} (Watt)	τ (Å/s)
Ag/Fe	14	10	P_{Ag}:30 / P_{Fe}:80	τ_{Ag}:3 / τ_{Fe}:1
Pd/Fe	14	7 – 8	P_{Pd}:40 / P_{Fe}:60	τ_{Pd}:2 / τ_{Fe}:1

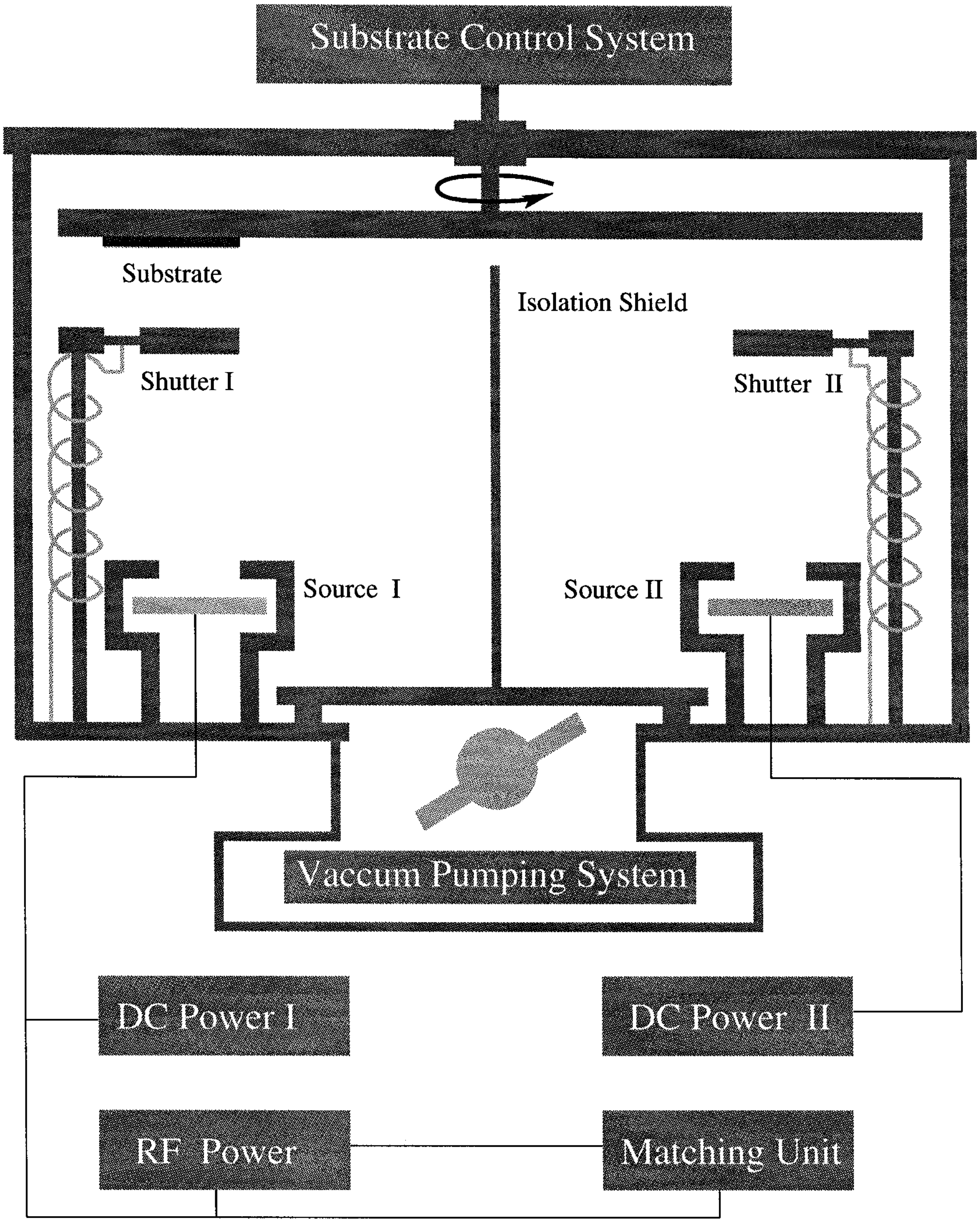

Figure 3.1: Schematic diagram of the multifunction deposition system.

3.2 X-ray Diffraction

X-ray diffraction is a non-destructive technique which provides quantitative information about the structural properties of the multilayers. In an x-ray scattering measurement, the intensity of a reflected radiation from a sample surface relative to the intensity of the incident beam is monitored as a function of wave vector transfer, $\mathbf{q}$, defined as $\mathbf{q} = \mathbf{k_r} - \mathbf{k_i}$, where the $\mathbf{k_r}$ and $\mathbf{k_i}$ are the reflected and incident wave vectors respectively. The most commonly used scattering geometry is the reflectivity measurement(Fig. 3.2), in which the incident angle (θ_i) and reflected angle (θ_r) are equal ($\theta_\mathrm{i} = \theta_\mathrm{r} = \theta$) so that the $\mathbf{q}$ is normal to the layers, and the magnitude of $\mathrm{q} = 4\pi \sin\theta/\lambda$. The reflectivity measurement is conventionally separated into low-angle ($2\theta < 20^\circ$) and high-angle ($2\theta > 20^\circ$) regions. In the low-angle region, the length scales probed by x-rays are much larger than the lattice spacings of the constituent layers, hence the scattering can be considered to solely arise from the chemical modulation of the structure. The low-angle x-ray scattering intensity of a sample with a rough interface is composed of specular intensity and diffuse background. The specular reflectivity provides information about the structure normal to the interfaces, i.e. the thicknesses, the intermixing and roughness of the constituent layers. The diffuse components can be determined by performing ω-scan and fitting the calculated diffuse scattering profile to the experimental one. The ω-scans, (also referred to as diffuse scan, transverse scan, or ω-rock), measures the scattered intensity as a function of θ_i while fixing the detector at certain 2θ (see Fig. 3.3) and rocking the sample around the specular peak at $\theta_\mathrm{i} = \frac{1}{2}(2\theta)$. The diffuse scattering provides lateral information about the roughness structure at the interfaces. In the high-angle region, the x-rays probe the atomic structure and the diffraction spectra provide information about the crystal structure. Quantitative analysis can be done by modeling the reflectivity spectra and fitting the calculated reflectivity spectra to the experimental ones.

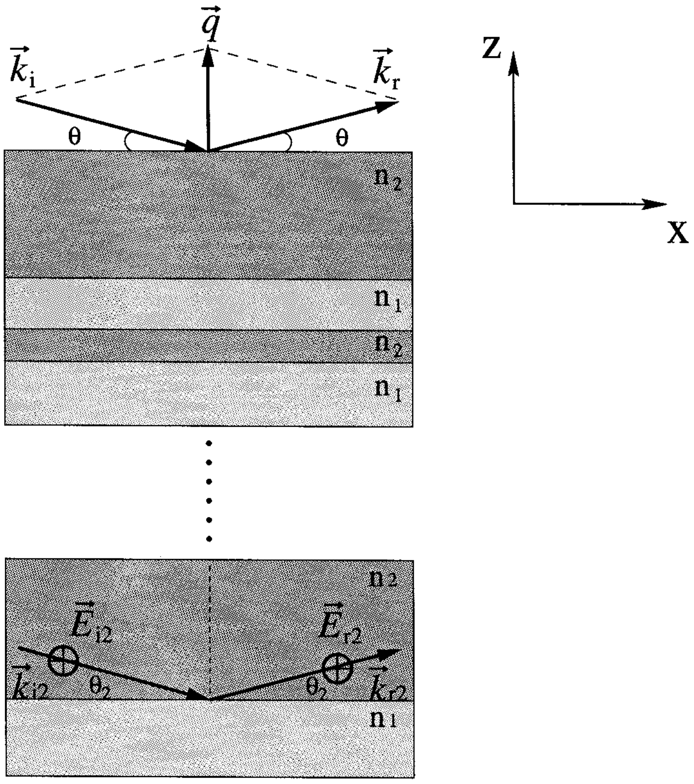

Figure 3.2: The schematic illustration of x-ray reflected by a stratified medium.

3.2.1 X-ray Reflectivity of Multilayers

An x-ray is essentially an electromagnetic wave. When an x-ray is scattered by an atom, the primary interaction is between the electric field of the x-ray and the electron charges of the atom, while the electromagnetic field couples with the spin or magnetic moment very weakly. The scattered amplitude is described by the atomic scattering factor,

$$\mathrm{F} = \mathrm{f_o} + (\Delta \mathrm{f}') + \mathrm{i}(\Delta \mathrm{f}''). \tag{3.1}$$

in which $\mathrm{f_o} = \mathrm{Z}$ is the atomic scattering factor at zero-momentum transfer and $\Delta\mathrm{f}'$ and $\Delta\mathrm{f}''$ are the real and imaginary parts of the dispersion corrections to $\mathrm{f_o}$, respectively.

Low-angle X-ray Reflectivity

At glancing angle, the wave vector q is sufficiently small that the length scales probed by the radiation are much larger than the inter-atomic distance. The medium can be treated as a continuum characterized by the refractive index, n, which is related to F by

$$\mathrm{n} = 1 - \mathrm{r_e}\frac{\lambda^2 \mathrm{N_o}}{2\pi}\mathrm{F}. \tag{3.2}$$

where $\mathrm{r_e}$ is the classical electron radius ($\mathrm{r_e} = 2.810\times10^{-5}$ Å), λ is the wavelength of the x-ray, $\mathrm{N_o}$ is the number density of atoms. n is usually written as

$$\mathrm{n} = 1 - \delta - \mathrm{i}\beta. \tag{3.3}$$

Combine Eqn. (3.1), (3.2) and (3.3),

$$\delta = \frac{\mathrm{r_e}\lambda^2\mathrm{N_o}}{2\pi}(\mathrm{f_o} + \Delta\mathrm{f}') = \frac{\lambda^2}{2\pi}\mathrm{r_e}\rho_\mathrm{e}, \tag{3.4}$$

$$\beta = \frac{\mathrm{r_e}\lambda^2\mathrm{N_o}}{2\pi}(\Delta\mathrm{f}'') = \frac{\mu}{4\pi}, \tag{3.5}$$

where $\rho_\mathrm{e} = \mathrm{N_o}(\mathrm{Z}+\Delta\mathrm{f}')$ is the electron density, and $\mu = 2\mathrm{r_e}\lambda^2\mathrm{N_o}\Delta\mathrm{f}''$ is the absorption coefficient.

The value for δ is typically in the order of 10^{-6} – 10^{-5}, so the real part of n is slightly less than 1. A beam of x-ray impinging on a flat surface can be totally reflected when the incident angle is below a critical angle θ_c, which can be obtained by applying Snell-Descartes' law. In a good approximation,

$$\theta_\mathrm{c} = 2\delta. \tag{3.6}$$

Since an x-ray is an electromagnetic plane wave, the propagations of its electric (**E**) and magnetic (**H**) field components in a medium obey Maxwell's equations. The intensity of the wave is proportional to the square of the amplitude of its electric field($|\mathbf{E}|^2$). The calculation of x-ray reflectivity, defined as the ratio between the intensities of reflected and incident x-rays, is to relate the electric field components of the incident and reflected x-rays. The x-ray reflectivity can be calculated exactly using the electron profile, or using a matrix method[69] as well. We use the formalism of Vidal[70] for the reflectivity calculation in the fitting program, which is essentially a matrix method. In this method, the components of the electric fields in the two media separated by an interface are related by the transfer matrix M. The matrix elements of M is a function of refractive indexes of the two media, the incident angle and the incident wave vector. For a multilayer, the total transfer matrix($\mathrm{M_{total}}$) relating the components of the electric fields of the incident wave, reflected wave and transmit wave is given by the product of the transfer matrices of all the interfaces,

$$\mathrm{M_{total}} = \mathrm{M_{N,N-1}M_{N-1,N-2}\cdots M_{2,1}}. \tag{3.7}$$

And the reflection and transmission coefficients can be calculated from the matrix elements of $\mathrm{M_{total}}$. The transform matrix by Vidal[70] includes the effect of interface roughness. For details of the formalism, see appendix 1.

High-angle X-ray Reflectivity

The theoretical x-ray diffraction pattern is calculated using a kinematic formalism[71]. The general model of a superlattice consists of a stack of M bilayers of material A and B characterized by scattering factors $\mathrm{F_A}$, $\mathrm{F_B}$. Material A (or B) has an integral number of atomic layers $\mathrm{N_A}$ (or $\mathrm{N_B}$). The structure factor of the superlattice can be written as

$$\mathrm{F_{SL}(q)} = \sum_{j=1}^{M} \exp(\mathrm{iqx_j})\{\mathrm{F_{Aj}} + \exp[\mathrm{iq(t_{Aj} + a_{Aj})}]\mathrm{F_{Bj}}\}, \tag{3.8}$$

where

$$\mathrm{x_j} = \sum_{s=1}^{j-1} (\mathrm{t_{As} + a_{As} + t_{Bs} + a_{Bs}}), \tag{3.9}$$

and q is the scattering vector given by $\mathrm{q}=4\pi\sin\theta/\lambda$; $\mathrm{F_{Aj}}$ and $\mathrm{F_{Bj}}$ are the scattering factors, $\mathrm{t_{Aj}}$ and $\mathrm{t_{Bj}}$ are the layer thicknesses of materials A, B in the j^{th} bilayer; $\mathrm{a_{Aj}}$ and $\mathrm{a_{Bj}}$ are the interface distances separating the layers. The scattering intensity is given by square of the structure factor $< \mathrm{F_{SL}(q)F^*_{SL}(q)} >$.

In the modeling, two types of disorder, interlayer disorder and intralayer disorder, are included. The interlayer disorder refers to the deviation in the periodicity of the layers in the growth direction resulting from interface disorder and layer thickness variations. To simulate this effect, the variation of interface distance $\mathrm{a_{Aj}}$ and $\mathrm{a_{Bj}}$ is assumed to follow a continuous Gaussian distribution about an average value, and the layer thickness variation is included by assuming a discrete Gaussian variation of $\mathrm{N_A}$ (or $\mathrm{N_B}$) about an integer average value. The intralayer disorder refers to the quality of the atomic ordering within a single layer. The intralayer disorder is included while calculating F_A and F_B: the inter-planar distance is assumed to fluctuate around an average value following a continuous Gaussian distribution, and the fluctuations are assumed to be cumulative. In addition, the average inter-planar distances between the three atomic planes closest to the interface are allowed to deviate with respect to the bulk d-spacing, which simulates the lattice distortion at the interface due to the lattice mismatch between the two different materials. The scattering intensity is then given by $I(q) = < F_{SL}(q)F^*_{SL}(q) >$, where the brackets are an ensemble average over all possible F_{Aj}, F_{Bj}, t_{Aj}, t_{Bj}, a_{Aj} and a_{Bj} weighted by corresponding Gaussian distributions. Before comparing the calculated I(q) with the measured profile, a scaling factor, an absorption correction, the Lorentz-polarization factor and a background intensity are included.

3.2.2 *Low-angle X-ray Reflectometer*

Low-angle x-ray reflectivity measurements were carried out on a high-resolution diffractometer with a conventional 2.2 kW Cu-K_α x-ray tube source. The layout of the diffractometer is shown schematically in Fig. 3.3.

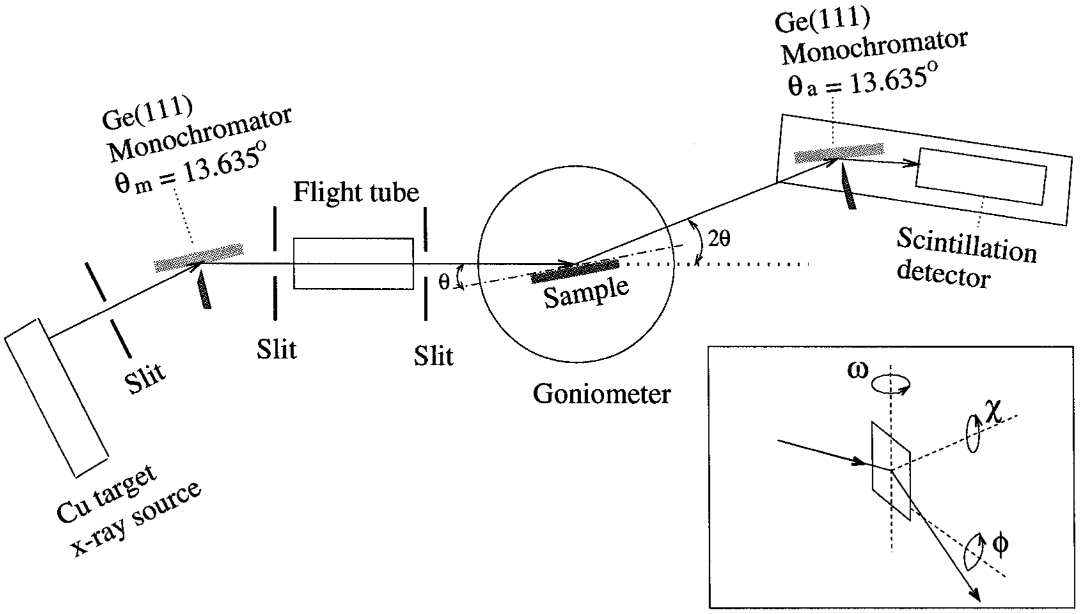

Figure 3.3: A schematic diagram of the low-angle x-ray reflectometer. The inset shows the rotation of the sample about three axes.

To achieve high resolution, two identical germanium single crystals with (111) orientation are used as monochromator and analyzer. Set at the Cu-K_α Bragg angle, the monochromator and the analyzer select radiation with a narrow range of wavevectors. Three sets of slits are place along the path of the x-rays to collimate the beam. The mechanical resolution of the slits is 0.01 mm in both horizontal and vertical directions. A resolution of order 0.01°, full width at half maximum (FWHM), for a $\theta - 2\theta$ scan ($\theta_\mathrm{i} = \theta_\mathrm{r} = \theta$) is achieved, corresponding to a Δq of 0.0014 $Å^{-1}$ in reciprocal space. Further increase of the resolution about one order higher in a $\theta - 2\theta$ scan can be achieved by filtering the Cu-K_α radiation.

The sample is mounted on a goniometer, which allows the translation of the sample in two directions and rotation of the sample about three axes, as shown in the inset of Fig. 3.3. The specular reflectivity measurements have been performed in the 2θ range between 0.3° – 8° at a step of 0.02° in 2θ (Δq = 0.0014 $Å^{-1}$).

Due to the high angular resolution of the diffractometer, particular care was taken to align the sample and the detector. For each alignment, the zero angle of the detector was set in the location of maximum beam intensity with no sample present. The sample was translated into the beam until it blocked half the x-ray beam at $\theta =$ 0°. The $\theta - 2\theta$ alignment was optimized by a couple of quick $\theta - 2\theta$ scans followed by a few ω scans with fixed 2θ where the reflected intensities were high (usually at the 2θ positions of superlattice peaks).

3.2.3 High-Angle X-ray Diffractometer

High-angle x-ray diffraction measurements were performed using an automated Nicolet-Stöe L11 powder diffractometer with a 2.2 kW Cu-K_α x-ray tube source. The general layout of the apparatus is shown in Fig. 3.4. A graphite crystal is used as the analyzer, which gives higher intensity at the expense of lower resolution as compared to the germanium single crystals. The width of sample slit is 1.8 mm. The detector slit with a width of 0.2 mm provides an angular acceptance of $\sim$ 0.3°. The axial divergence of the beam is limited to $\sim$ 3°. Most measurements were performed in a 2θ range between 30° and 100° at a step of 0.2°.

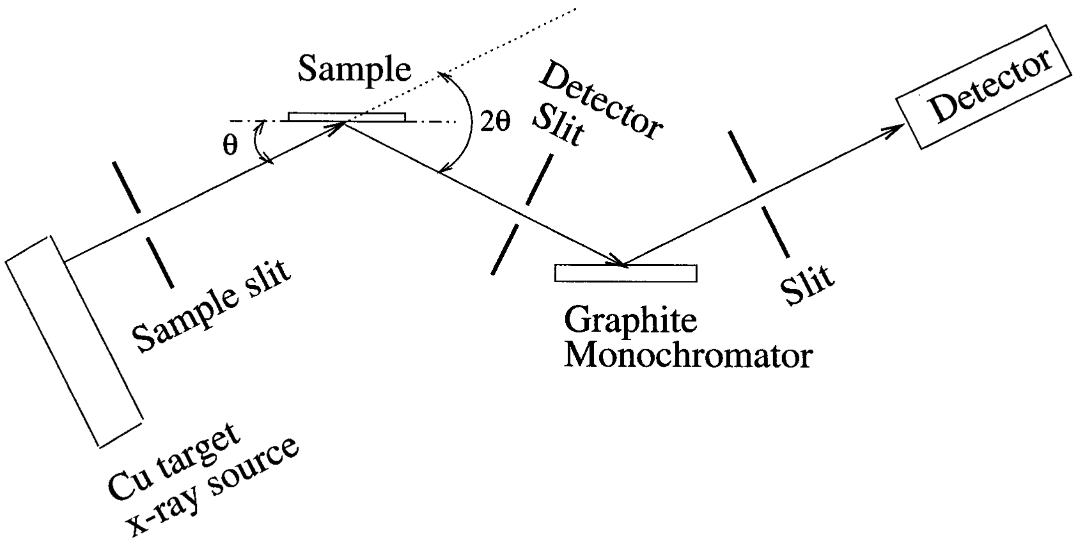

Figure 3.4: A schematic diagram of the high-angle x-ray reflectometer.

3.3 *Polarised Neutron Reflectivity*

X-ray and neutron reflectometry measurements are the two principal techniques used to study the composition modulation of multilayers. The scattering geometry, in which the neutron reflectivity is measured, is the same as that of x-ray reflectometry measurement. Undergoing different interactions, the x-rays probe the electron density profile, while the neutrons map the nuclei as well as the existing magnetic profile. In a spin-polarized neutron reflectivity measurement, the incident neutrons are polarized to be spin-up or spin-down. Spin-up (-down) neutrons are those with magnetic moments parallel (antiparallel) to the guide field. The reflected spin-up and spin-down neutrons can be measured respectively to yield the neutron reflectivities in four channels: non-spin-flip (NSF) spin up-up and spin down-down channels, and spin flip (SF) spin up-down and spin down-up channels. For each channel, the first spin state is for the incident neutrons, while the second spin state is for the reflected neutrons. The reflectivity corresponding to these four channels are R^{++}, R^{--}, R^{+-} and R^{-+}, where $^+$ and $^-$ indicate spin-up and spin-down respectively. The polarised neutron reflectivities provide vital information on the chemical modulation and magnetic profile in a multilayer.

3.3.1 Neutron Reflectivity of Multilayers

The neutron is a particle with a magnetic moment and zero electric charge. A beam of neutrons have wave-like properties and can be described by a wave of wavelength λ appropriate to neutron velocity v, and given by the de Broglie relation,

$$\lambda = h/mv, \tag{3.10}$$

where h is the Planck's constant.

In vacuum, the neutron potential is zero, while in a medium, the potential energy is mainly from strong interactions with nuclei and existing magnetic field of atoms. The nucleus-neutron scattering via the nuclear force is strong but the scattering process is elastic for rigidly bounded nuclei, and the potential extension is much smaller than the neutron wave length. Hence the interaction potential energy of an atom can be described by the Fermi pseudopotential[72]

$$\mathrm{V_F(r)} = \mathrm{b_n}\left(\frac{2\pi\hbar^2}{\mathrm{m}}\right)\delta(\mathrm{r}), \tag{3.11}$$

where $\mathrm{b_n}$ is the nuclear scattering length, and r is the position of the neutron. $\mathrm{b_n}$ is generally a complex number, $\mathrm{b_n} = \mathrm{b_c} + \mathrm{ib}'$. $\mathrm{b_c}$ is called the coherent scattering length. The imaginary part b', which determines the absorption of the neutrons, is negligible for thin films except for certain elements, such as Gd, Sm, B and Cd. The total scattering cross section is given by $\sigma_{\mathrm{tot}} = 4\pi <\mid \mathrm{b_n} \mid^2>$, in which the brackets designate the statistical average over the neutron and nuclear spins.

At glancing angle, the medium can be treated as a continuum, and the mean potential energy can be expressed as[73]

$$\mathrm{V_n} = \frac{2\pi\hbar^2\rho\mathrm{b_n}}{\mathrm{m}}, \tag{3.12}$$

where ρ is the atomic density.

The neutron carries a magnetic moment, and the dipolar interaction of neutron spin with effective magnetic field $\mathbf{B_{eff}}$ is expressed as[73]

$$\mathrm{V_M(r)} = -\boldsymbol{\mu}\cdot\mathbf{B} = -\mathrm{g_n}\mu_\mathrm{n}\boldsymbol{\sigma}\cdot\mathbf{B_{eff}}, \tag{3.13}$$

where $\boldsymbol{\mu}$ is the neutron moment, μ_n is the nuclear magneton, g_n is the nuclear Landé factor of neutron, $\boldsymbol{\sigma}$ is the Pauli operator associated to the neutron spin, and $\mathbf{B_{eff}}$ is the vector sum of the external field and the existing magnetic field created by the unpaired electrons of the magnetic atoms. The magnetic field from a magnetic atom contains two terms, the spin part and the orbital part[73]:

$$\mathbf{B} \;=\; \frac{\mu_o}{4\pi}\left(\nabla\times\left\{\frac{\boldsymbol{\mu_e}\times\mathbf{R}}{|\mathbf{R}|^3}\right\} \;-\; \frac{e\;\boldsymbol{v}_e\times\mathbf{R}}{|\mathbf{R}|^3}\right), \tag{3.14}$$

where $\boldsymbol{\mu_e} \;=\; -\,2\mu_B\boldsymbol{\sigma}$ is the magnetic moment of the electron, and $\boldsymbol{v}_e$ is the speed of the electron. By integrating $-g_n\mu_n\boldsymbol{\sigma}\cdot\mathbf{B}$ on a homogeneous magnetic layer, the mean interaction potential energy due to magnetic moment of the electron can be written as[73]:

$$V_m \;=\; \frac{2\pi\hbar^2}{m}\rho\cdot b_m, \tag{3.15}$$

where $b_m \;=\; 2.696\;\boldsymbol{\sigma}\cdot\mathbf{M}_{||}$ fm, is the magnetic scattering length; $\mathbf{M}_{||}$ is the in plane magnetic moment given in μ_B per atom.

From Eqn. (3.12) and Eqn. (3.15), the interaction of neutron with matter is characterized by the scattering length b, which includes contributions from both chemical and magnetic structures. For non-magnetic media, the total $b = b_n$, and only the chemical structure contributes to the scattering process, while for magnetic media, neutrons interact with both nuclei and the atomic moments. In a spin-polarized neutron reflectivity measurement, if the magnetisation of the medium is saturated in-plane, the SF reflectivities are essentially zero. Neutrons measure the in-plane moment through the NSF reflectivities. The neutron reflectivity is the square of the Fourier transforms of scattering length density, ρ, which is the scattering length b multiplied by the in-plane atomic densisty. The neutron reflectivity is given by[74],

$$R(q) \;=\; \left(\frac{4\pi}{q}\right)^2\left|\int_{-\infty}^{+\infty}\rho(z)e^{iqz}dz\right|^2. \tag{3.16}$$

R^{++} and R^{--} are different since the neutron scattering density b is different for spin-up and spin-down neutrons, $b = b_n \;\pm\; b_m$, where the + and − signs are for the spin-up and spin-down neutrons, respectively. Information about b_m and the magnetic moment of a medium can be obtained by fitting the calculated reflectivities to the experimental ones.

The neutron-matter interaction is different to x-ray–matter interaction, whereas, the neutron reflectivity of a multilayer can be calculated using optical formalism similar for the case of x-ray reflection. For the details of the formalism, see Appendix *A*.2.

3.3.2 Polarised Neutron Reflectometer

The PNR experiments were carried out on the C5 triple-axis spectrometer of the DUALSPEC facility at Chalk River. The schematic set-up is shown in Fig. 3.5. A Cu_2MnAl Heusler single crystal set at (111) Bragg reflection selects the incident neutrons with a wavelength of 2.3705 Å and down-spin polarization. A graphite filter is used to remove the neutrons with higher-order wavelengths in the diffracted beam. The polarised neutrons are guided by a field produced by a magnetic box consisting of permanent magnets to prevent the neutrons from depolarizing. Two Mezei-type[75] spin flippers were installed in front of and after the sample. The spin flipper is made of two sets of coils, with appropriate currents, the field produced by the horizontally wound coil cancels the stray field from the magnetic guide box, and the vertically wound coil produces a field which can reverse the neutron spin. The flippers enabled the measurement of all four spin-dependent scattering channels: spin up-up, spin down-down, spin up-down and spin down-up channels. The diffracted beam was 2 inches high, and the width was determined by the sizes of slit 1 and slit 2, which were varied during a scan. The angular resolution was determined by the sizes and the separation between slit 1 and slit 2, as well as the distance between slit 2 and sample. The samples used in this study were multilayers deposited on 100 mm diameter and 6.35 mm thick single crystal Si(100) circular wafers. An in-plane magnetic field of > 250 Oe provided by permanent magnets was used to align the moments of the multilayers parallel to the field. For low temperature measurements, the samples were field-cooled to 4.5 K using a liquid helium cryostat. Reflectivity scans have been made in all four neutron spin-dependent cross sections in the q range

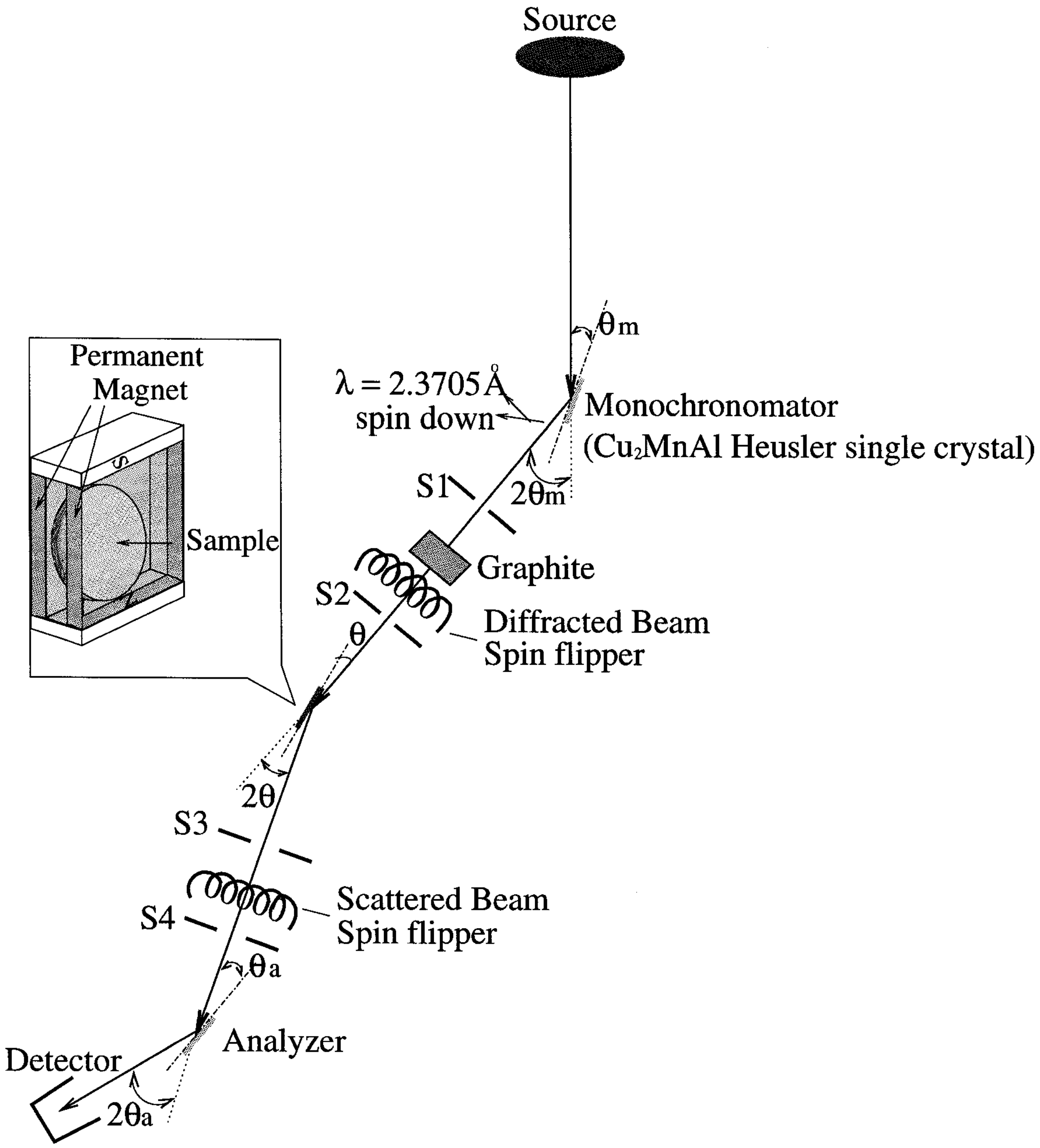

Figure 3.5: A schematic diagram of the polarised neutron reflectometer.

of 0.004 – 0.35 $Å^{-1}$.

3.4 Transmission Electron Microscopy

TEM measurements were performed using a Philips CM200 FEG microscope with accelerating voltage of 200 kV at National Center for Electron Microscopy, Lawrence-Berkeley National Laboratory. The microscope was operated in energy-filtered imaging mode using K-edge electrons, which are those electrons that lose a certain amount of energy to ionize the atoms of the specimen by exciting K shell electrons and giving a saw-toothed edge in energy-lose spectrum as schematically shown in Fig. 3.6. K-edge electrons were chosen because the electrons undergoing inner-shell ionization contain information characteristic of the atoms in the specimen. The images of the specimen were obtained using electrons with energy-loss of “pre-edge” and “post-edge” as indicated in Fig. 3.6. The background intensity coming from plural-scattering events, which are usually associated with outer-shell interactions, was subtracted by calculating the jump ratio, which is given by $(I_{\text{post-edge}} + I_{\text{pre-edge}})/I_{\text{pre-edge}}$. The jump ratio images had sharp contrast and the resolution is about 7 Å.

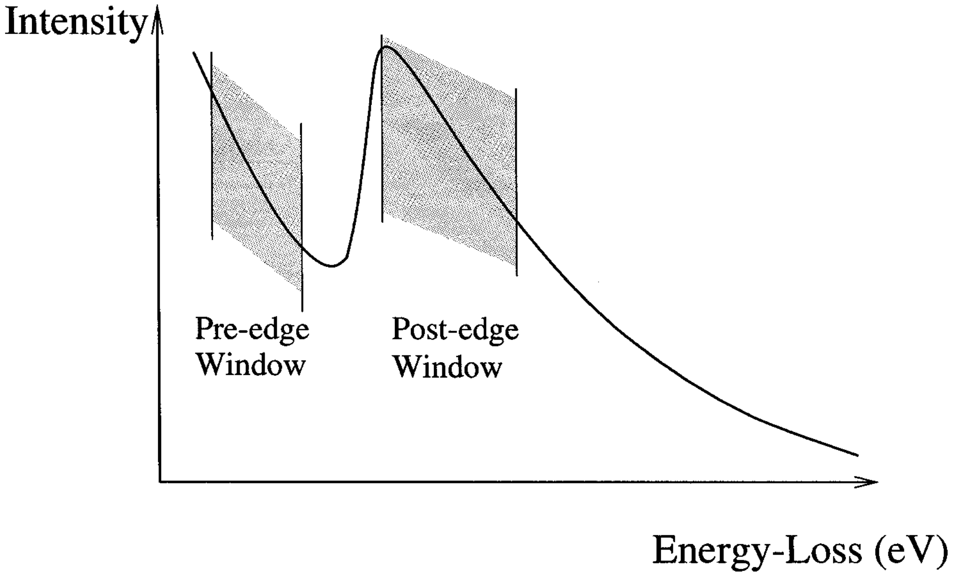

Figure 3.6: A schematic diagram of the energy-loss spectrum.

Specimens for TEM were prepared by a standard method, involving cross-sectioning, dimpling, and final thinning done with a Technoorg Linda IV3 Ar beam mill using a liquid-nitrogen cold stage.

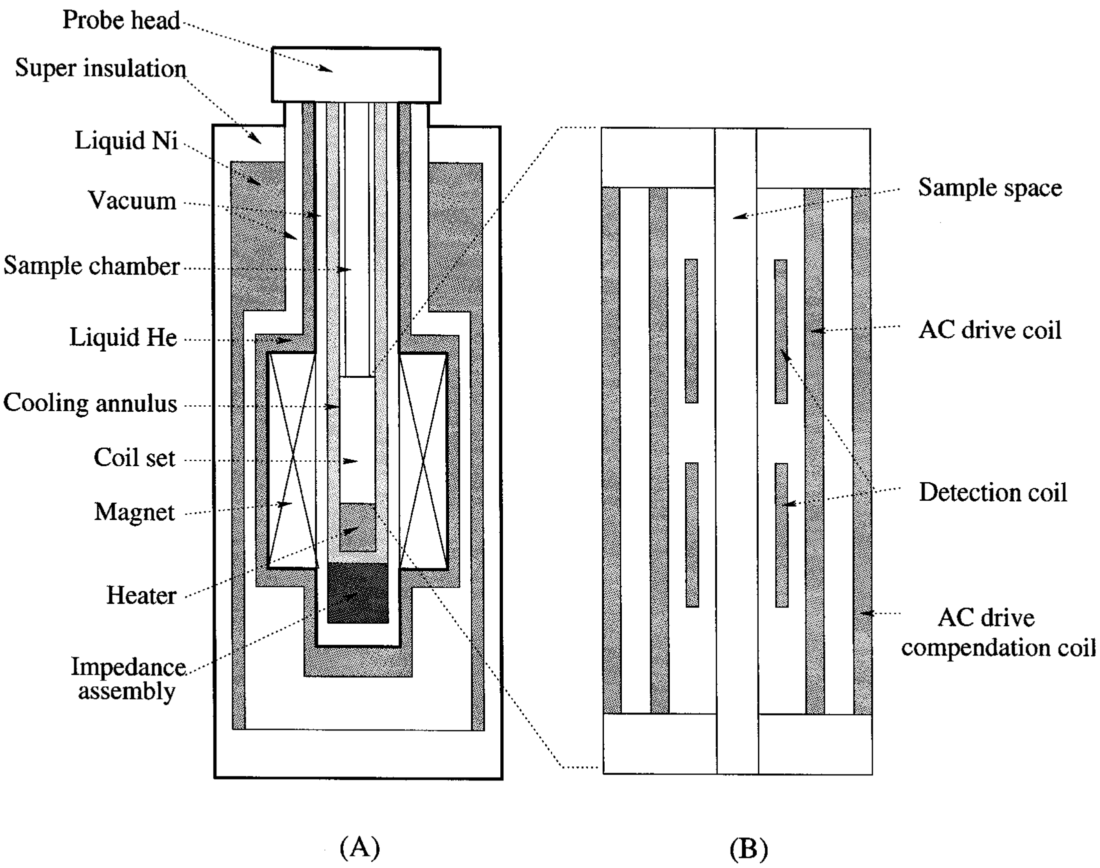

Figure 3.7: A schematic diagram of the AC susceptometer: (A) cross section of the PPMS dewar and probe (seperated by the thick solid line); and (B) cross section of the ACMS coil set.

3.5 Magnetometry Measurements

Magnetometry measurements provide important information on the magnetisation, magnetic anisotropy, and magnetic phase transition. In this study, the DC magnetisation of the multilayers was measured using a custom-made AC Measurement System (ACMS) unit connected to a Quantum Design Physical Property Measurement System (PPMS) workstation. The ACMS unit and associated ACDC-Mag software are capable of performing both DC magnetisation and AC susceptibility measurements. The PPMS provides the temperature control and the magnetic field control. The apparatus is made of three main parts: PPMS dewar, PPMS probe, and AC coil set, as shown in Fig. 3.7.

The aluminum PPMS dewar contains a super insulation layer, a liquid nitrogen layer and a vacuum layer to minimize the consumption of liquid He. The PPMS probe, placed in the liquid helium bath, incorporates the elemental temperature control hardware and the superconducting magnet. Above 4.2 K, the sample is cooled by drawing cold He vapor from the liquid He dewar into a cooling annulus, or heated by a heater mounted at the base of the sample chamber. The He flow rate is controlled by an impedance assembly. Below 4.2 K, the cooling annulus is filled with a controlled amount of liquid He. The pressure above the liquid He is reduced by opening the flow control valve. The boiling point of He is reduced consequently. The temperature can go down to 1.9 K. The 9 Tesla superconducting magnet is a longitudinal solenoid composed of niobium/titanium alloy embedded in copper, which provides a high field homogeneity (0.01 %) within the measuring region. The AC coil set contains the drive and detection coils. The drive coil provides an AC excitation field for the AC susceptibility measurement. The detection coils are two sets of counter-wound copper coils connected in series. Such a configuration senses the inductive signals from a sample and rejects interference from uniform background sources.

For the DC magnetisation measurements in this study, two methods were used to mount the samples. For the Ag/Fe multilayers, samples were broken into small pieces and put in a plastic bucket. The bucket was attached to a sample rod, and then placed in the center of the detection coil. For the Pd/Fe multilayers, a 4×20 mm^2 sample was inserted into a plastic straw and fixed at the end of the straw. The straw was attached to the sample rod. The DC magnetisation was measured as a function of magnetic field up to 5 Tesla, and the diamagnetic signals from the sample holders and Si substrate were removed from saturation magnetisation by extrapolating the magnetisation to zero field.

3.6 Mössbauer Spectroscopy

Mössbauer spectroscopy involves the use of γ-rays to probe the nuclear transitions in Mössbauer active atoms. In a Mössbauer experiment, γ-rays are provided by a source which decays to the Mössbauer nuclide. A velocity, called Doppler velocity (v_D), is applied to either the source or the absorber using a drive system in order to impart an additional Doppler energy of $E_D = E_o v_D/c$ to the emitted γ-ray, where E_o is the energy of the emitted γ-ray, and c is the velocity of the light. By moving the source in a precise and controlled velocity, the energy of the γ-ray can be varied continuously in a range of interest. As the γ-rays propagate through the sample (absorber), those at energies matching the excitation energies of the Mössbauer active atoms at the ground state in the absorber are absorbed resonantly, causing a reduction in the intensity of transmitted γ-rays, or an increase in the reemitted γ-rays, x-rays, or electrons by nuclides undergoing de-excitation in the absorber. The Mössbauer spectrum is obtained by registering the resonant absorption of the γ-rays as a function of Doppler velocity, which corresponds to the γ-ray energy. By analyzing the Mössbauer spectra, the hyperfine parameters can be obtained, which reveal the local environment of the Mössbauer active atoms in the absorber.

3.6.1 Basic Concepts

The Mössbauer effect is essentially a process of emission and nuclear resonance absorption of γ-rays by recoil-free nucleus of the same kind. It is associated with nuclear transition from an excited state of energy E_e to the ground state of energy E_g, or vice versa. The spectral lines, in term of the intensity as a function of the transition energy(I(E)), of emitted or absorbed γ-ray do not have a single energy of $E_o = E_e - E_g$. Instead, the energy of the γ-ray has a distribution centered around E_o with a width of Γ(Heisenberg natural line width). This is because the energy level of the excited state spreads over a certain energy range of width $\Delta E_e(= \Gamma)$, due to the finite mean life. I(E) was found to have Lorentzian or Breit-Wigner form. Nuclear resonance absorption occurs only if the γ-emission line and the γ-absorption line appear at the same energy position or partially overlap. Between nuclei of free or loosely bound atoms, nuclear resonance absorption does not occur due to the recoil effect. Assume the nucleus is at rest before decay or excitation. Momentum conservation requires a recoil to be imparted to the nucleus after a γ-emission or a γ-absorption. The kinetic recoil energy of $E_R \sim E_o^2/2Mc^2$ is involved, where M is the mass of the nucleus. In the emission process, the nucleus moves in the opposite direction to the direction of the γ-emission and takes up the recoil energy. The emission line is shifted to $E_\gamma = E_o - E_R$. In the absorption process, the nucleus moves in the same direction as the direction of the absorbed γ-ray, which requires a total energy of $E_\gamma = E_o + E_R$ to excite the nucleus and make up the recoil effect. As a result, the emission line and absorption line are separated by $2E_R$ on the energy scale, which is about 10^6 times larger than the natural line width. Overlap between the transition lines and hence nuclear resonance absorption is impossible.

In the solid state, atoms are rigidly bound to the lattice and vibrate about their equilibrium positions, so that the behavior of the recoiling atom is different from that of a free atom. According to the quantum theory of the harmonic crystal, the lattice vibrational energies are quantized and can only change by integral multiples of the phonon energy $\hbar\omega$ (ω represents the characteristic frequency of a vibrational mode). If E_R is less than the phonon energy $\hbar\omega$, either zero or one unit of phonon energy may be transferred to the lattice. So there is a certain probability f that no lattice excitation (zero-phonon transition) takes place, and the nuclear undergoes transition without recoil. In a zero-phonon transition, the whole crystal rather than a single atom recoils. Due to the very large mass of the crystal as compared to the mass of a single nucleus, the recoil energy is many orders of magnitude smaller than Γ, and this process is then effectively recoil-free. The γ-ray emitted by a recoil-free atom carries the total energy of the nuclear transition, and the excitation energy needed by a recoil-free atom equals to the energy of the nuclear transition. Hence resonant absorption of γ-ray is achieved which gives rise to the Mössbauer effect. f, called the recoil-free fraction, can be derived using the Debye model for solids, and has the following expression[76]:

$$f = \exp\left[\frac{-6E_R}{k_B\Theta_D}\left\{\frac{1}{4} + \left(\frac{T}{\Theta_D}\right)^2 \int_0^{\Theta_D/T} \frac{x}{e^x - 1}dx\right\}\right], \tag{3.17}$$

which reduces to the following approximations at temperatures much lower and much higher than the Debye temperature,

$$f = \exp\left[-\frac{\mathrm{E_R}}{\mathrm{k_B}\Theta_\mathrm{D}}\left(\frac{3}{2}+\frac{\pi^2\mathrm{T}^2}{\Theta_\mathrm{D}^2}\right)\right], \quad \text{for } \mathrm{T} \ll \Theta_\mathrm{D}, \tag{3.18}$$

$$f = \exp\left(-\frac{6\mathrm{E_R T}}{\mathrm{k_B}\Theta_\mathrm{D}^2}\right) \quad \mathrm{T} \gg \Theta_\mathrm{D}, \tag{3.19}$$

where $\mathrm{k_B}$ is the Boltzmann factor and Θ_D is the Debye temperature.

Mössbauer spectrum records the spectral lines of γ-rays. A ^{57}Fe Mössbauer spectrum may contain a single line, or a doublet, or a sextet, or a combination of these features, which reflects the nature and the strength of the hyperfine interactions. There are only three kinds of hyperfine interactions to be considered in practical Mössbauer spectroscopy: electric monopole interaction ($e0$), electric quadrupole interaction ($e2$) and magnetic dipole interaction ($m1$).

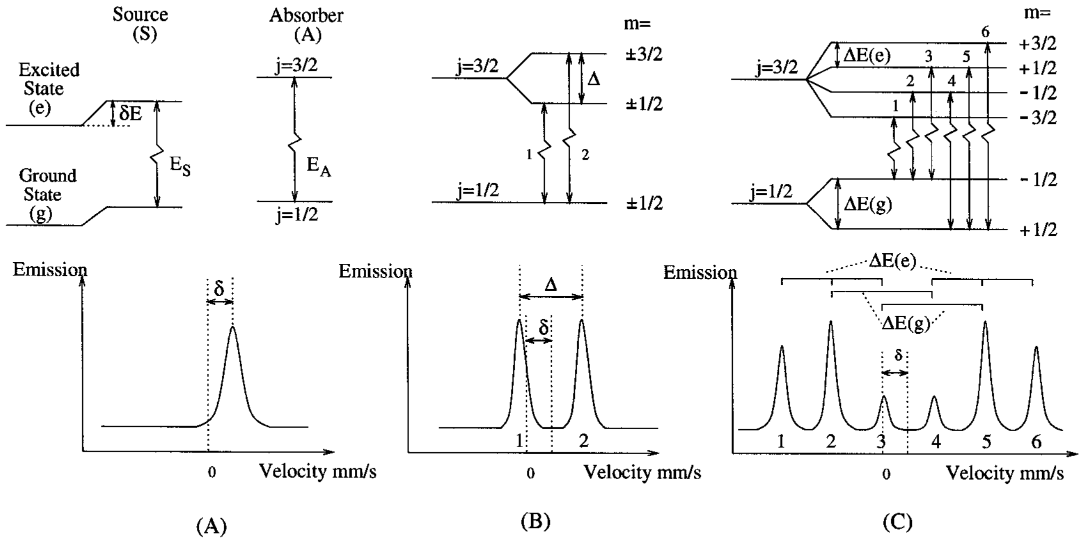

(A) (B) (C)

Figure 3.8: A schematic diagram of the effects of hyperfine interactions on the nuclear energy levels of ^{57}Fe illustrating the origins of: (A) isomer shift (δ); (B) quadruple splitting (Δ); and (C) the magnetic dipole splitting of the ground state ΔE(g) and the excited state ΔE(e). Resultant conversion-electron Mössbauer spectra are also presented.

In the absence of an electric field gradient and magnetic hyperfine field in the nuclear region, the Mössbauer spectrum is a single line associated with the electric monopole interaction (Fig. 3.8(A)). The electric monopole interaction is the electrostatic Coulomb interaction between the nuclear charge and electrons inside the nuclear region. The nuclear energy levels are shifted by the electric monopole interaction energy, which is called electrostatic shift. The isomer shift (δ) arises from the difference in the electrostatic shift between the source and the absorber, and is expressed by[76],

$$\delta = \frac{4\pi}{5}\mathrm{Ze}^2\mathrm{R}^2(\frac{\delta\mathrm{R}}{\mathrm{R}})(|\phi(0)|^2_{\mathrm{absorber}} - |\phi(0)|^2_{\mathrm{source}}) \tag{3.20}$$

where δR is the difference in mean nuclear radius R, between nuclear excited and ground state, and $|\phi(0)|^2$ is the total electron density at the nucleus dependent on the chemical environment of the Mössbauer nucleid. In ^{57}Fe Mössbauer spectroscopy, ^{57}Co diffused into metal foils, such as Rh, Cu, Pd and etc are use as sources, whose $|\phi(0)|^2_{\mathrm{source}}$ are different to each other. So the isomer shift δ relative to a standard reference material, α-Fe, is commonly reported,

$$\delta = \delta_{\mathrm{absorber}} - \delta_{\alpha-\mathrm{Fe}} = \frac{4\pi}{5}\mathrm{Ze}^2\mathrm{R}^2(\frac{\delta\mathrm{R}}{\mathrm{R}})(|\phi(0)|^2_{\mathrm{absorber}} - |\phi(0)|^2_{\alpha-\mathrm{Fe}}). \tag{3.21}$$

The isomer shift relative to α-Fe reflects the difference between the electron densities at the nucleus of the Fe atoms in absorber and the Fe atoms in the pure α-Fe.

The interaction between the electric field gradient and the nuclear quadrupole moment, called electric quadrupole interaction, splits the degenerate $j = \frac{3}{2}$ level and gives rise to a doublet in the spectrum (Fig. 3.8(B)). The $j = \frac{1}{2}$ level is unsplit since the ground state of ^{57}Fe has spherically symmetric distribution and corresponding to zero nuclear quadrupole moment. The interaction only occurs if the surrounding charge distribution is not in cubic symmetry, which gives rise to the electric field gradient. The doublet in the spectrum helps to identify crystallographic sites.

The magnetic dipole interaction or the nuclear Zeeman effect, is the interaction between a nuclear magnetic moment and the magnetic hyperfine field(B_{hf}) at the nucleus, so called magnetic hyperfine interaction. In the case of ^{57}Fe, the magnetic dipole interaction splits the $j = \frac{3}{2}$ level into $m = \pm\frac{3}{2}$ and $\pm\frac{1}{2}$ levels, and the $j = \frac{1}{2}$ level into $m = \pm\frac{1}{2}$ levels. The nuclear transition from the $j = \frac{3}{2}$ excited state to the $j = \frac{1}{2}$ ground state with selection rules $\delta m = 0,\pm 1$ allows six transitions and gives rise to a sextet in the spectrum (Fig. 3.8(C)). The transition probabilities are the squares of the Clebsch-Gordan coefficients corresponding to these angular momentum states, and hence they depend on the j and m values. The probabilities also depend on the angle θ between the detected γ-ray and the direction of the magnetic field producing the Zeeman splitting of the nuclear energy levels. The line intensity ratios are given by 3:x:1:1:x:3 where x = $4\sin^2\theta/(1+\cos^2\theta)$[77]. For an in-plane magnetized Fe, the six lines have intensity ratios 3:4:1:1:4:3. By an appropriated least-squares fit to the spectrum, one may obtain the related hyperfine parameters: δ, the quadrupole splitting (Δ), and the B_{hf}.

3.6.2 *Mössbauer Spectrometer*

^{57}Fe Mössbauer spectroscopy is a powerful method to study magnetic properties of Fe atoms located at surfaces, interfaces and in ultra-thin films. There are mainly two approaches to apply ^{57}Fe Mössbauer spectroscopy to thin films, the conventional transmission technique and conversion electron Mössbauer spectroscopy. In a conventional transmission Mössbauer experiment, the unaffected transmitted γ-rays are detected, while in a CEMS experiment, the so-called conversion electrons are detected.

A schematic diagram of a conventional transmission Mössbauer spectrometer is shown in Fig. 3.9. For ^{57}Fe Mössbauer spectroscopy, ^{57}Co*Rh* single line source is used. ^{57}Co decays primarily to the 137 keV state of ^{57}Fe, and this excited state decays immediately to the 14.4 keV first excited state, emitting 123 keV γ-rays. The decay from the first excited state to the ground state provides the 14.4 keV γ-rays for the Mössbauer effect measurements.

The source is moved by an electromagnetic velocity transducer, which consists of the drive and pickup coils moving in a homogeneous magnetic field. The driving unit feeds the transducer with a voltage, whose waveform is given by a digital function generator (DFG)'s reference signal. A triangular waveform was used in this study corresponding to constant acceleration mode. The amplified voltage difference between the reference signal and the induced pickup signal is applied to the drive coil. This negative feedback system minimises the deviations of the actual velocity from the reference waveform.

The detector used in transmission Mössbauer experiment is a proportional counter containing a Ar+10% CH_4 gas mixture. The magnitude of the pulses from the detec-

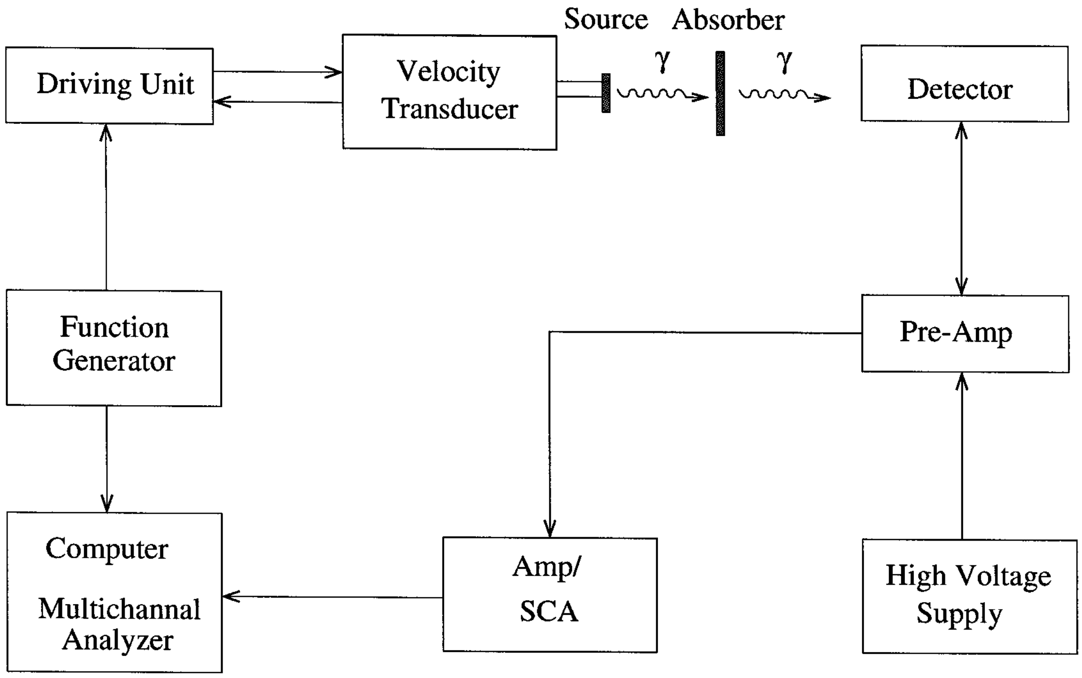

Figure 3.9: A schematic diagram of the Mössbauer spectrometer.

tor is proportional to the γ-ray energy. After amplification, the pulses are sorted by a single channel analyzer, which allows the selection of the γ-ray of interest from any other radiation emitted from the source. The detected counts are fed to a multichannel analyzer (MCA) installed in a computer which stores an accumulated counts in each of 512 registers known as channels. The MCA is synchronized with the transducer so that each channel corresponds to a particular velocity. Synchronization is accomplished as follows. The MCA is started by a 'START' impulse from DFG, which coincides with the beginning of the waveform. The DFG also generate 'CHA' pulses with period which equals to the period of the waveform divided by the number of the channels in the MCA. The channels are advanced by the 'CHA' pulses, and the counts obtained in the dwell time of the pulses are accumulated in the opened channel.

Conversion-electron Mössbauer spectroscopy (CEMS) works in the back scattering geometry in which conversion electrons are detected. The CEMS is based on the fact that an excited nucleus may de-excite by internal conversion (91 % probability) other than γ-ray emission (9% probability). In an internal conversion, the excited nucleus transfers its excess energy to one of the inner electrons with appreciable density at the nucleus. As a result, the electron, called a conversion-electron, is ejected from its orbit. Most of the internal conversion results in the ejection of a K-electron of 7.3 keV energy. The resulting excited atom with a K-shell hole further de-excites by emission of a 6.4 keV x-ray or a L-electron of 5.4 keV, which is called Auger electron.

The set-up of CEMS is the same as convention transmission Mössbauer spectrometer, except for the detector and the way the sample is mounted. A schematic diagram of the CEMS detector used in this study is shown in Fig. 3.10. The sample is mounted inside the detector and grounded, forming the cathode. A fine gold coated tungsten wire (25 μm diameter) biased to 500 – 1000 Volts forms the anode.

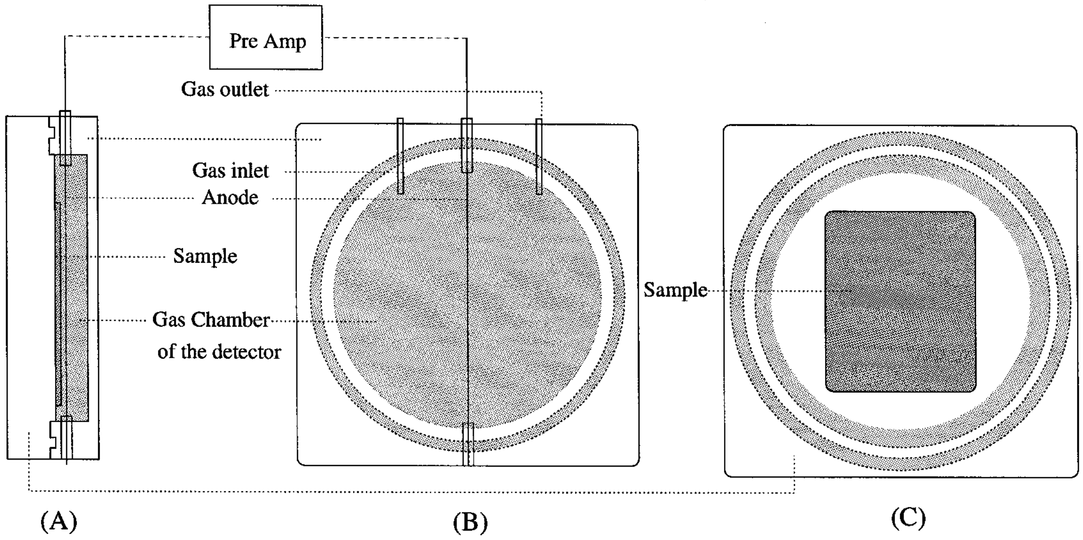

Figure 3.10: A schematic diagram of the conversion-electron detector: (A) cross sectional side view; cross sectional top views of the two detachable parts of the detector: (B) the gas chamber with the anode; (C) the cover with the sample.

A typical CEMS detector is a He+10%CH_4 gas-flow proportional counter operating between 90 – 290 K. A gas-filled He counter was used down to 50 K. Helium gas is used to minimize the sensitivity to γ-rays. The detector is constantly flushed with the counting gas with a flow rate of ~30 cm^3/min, to remove contamination from the atmosphere. The amplification of the signal from originally emitted electrons is achieved through the ionisation processes of He gas by the electrons emitted from the sample (primary ionisation process) as well as in the avalanches where secondary electrons are multiplied (secondary ionisation process). To prevent He ions from emitting additional electrons by colliding with cathode materials, CH_4 is added as a quench gas. Charges of He ions are transfered to CH_4 molecules by collisions. CH_4 ions are usually decomposed instead of emitting the additional electrons when colliding with the cathode.

The advantage of the CEMS over conventional transmission Mössbauer on the study of thin film containing Fe is that the CEMS detector has high sensitivity to ^{57}Fe. The standard transmission technique requires a minimum 100 – 200 Å thick ^{57}Fe, corresponding to 0.5 – 1 μm of natural iron, while a CEMS detector has a detection limit of 1/10 to 1/100 of a monolayer of ^{57}Fe. As a result, CEMS is a powerful tool to probe thin films made of natural Fe, which has only 2% abundance of ^{57}Fe.

In this study, the CEMS was applied to the multilayers in temperature range of 50 – 290 K. The temperature control was accomplished by a nitrogen flow cryo-stat in tempareture range of 90 – 290 K, and below 90 K by a closed cycle He refrigerator.

4

Structural and Magnetic Properties of Ag/Fe Multilayers

In this chapter, the structural and magnetic studies of Ag/Fe multilayers using x-ray diffraction, TEM, CEMS, and magnetometry measurements are presented. The purpose of small-angle x-ray and TEM studies is to prove that the bilayer thicknesses obtained from these two techniques are consistent, so that used correctly, small-angle x-ray reflectivity can provide a fast and accurate determination of the layer thicknesses in a multilayer. The crystalline orientation was examined using high-angle x-ray measurements, and the profiles were fitted using a kinematic diffraction formalism. CEMS and magnetometry studies confirmed that the variation of the hyperfine field does indeed follow the temperature dependence of the Fe moment.

4.1 *Structural Characterization*

4.1.1 *X-ray Reflectivity*

For multilayers Si(100)[Ag 30 Å/Fe t]$_{25}$/Ag 100 Å with nominal thicknesses of t_{Fe} = 5, 10, 15 and 20 Å, the reflected x-ray intensity is plotted on a semi-log scale as a function of 2θ and shown in Fig. 4.1, where θ is the angle of incidence. The size of the vertical lines represents the error in the intensity measurements. As mentioned in section 3.2.1, the reflectivity depends on the refractive index, hence the electron density. The refractive index of a crystal for x-ray wavelengths is slightly less than unity. As a result, below a critical angle θ_c, total reflection occurs at the crystal surface. θ_c is related to the electron density of the surface layer. The Ag top layer gives $\theta_c \approx 0.4^\circ$, as indicated by the dashed line at $2\theta = 0.8^\circ$ in Fig. 4.1. Below $2\theta_c$, the reflectivity is unity and the reflected intensity should be a constant and equal to the incident intensity of the x-ray beam. However, a small slope is observed instead of a horizontal line. This is because when the x-ray is incident at a glancing angle, the sample projection in the x-ray beam, which is smaller than the width of the beam, increases as the sample rotates to higher θ. The size of the beam incident on the sample, which is completely reflected, increases with θ until the sample projection starts to exceed the x-ray beam size. This effect is taken into account in the model calculation.

Beyond θ_c, x-rays penetrate into the film and are reflected at each interface. The superposition of all the reflected amplitudes gives rise to the interference pattern. The small period intensity oscillations result from the interference between the reflected beams from the two interfaces, one between the sample's top surface and air, the other between the sample's bottom surface and substrate. The constructive interference between the x-ray beams reflected from the surfaces of each bilayer gives rise to the strong superlattice peaks, whose θ position is determined by the critical angle θ_c and bilayer thickness Λ. To a good approximation[78],

$$\theta^2 = \theta_c^2 + \theta_B^2, \tag{4.1}$$

and the Bragg angle θ_B is determined from,

$$2\Lambda \sin\theta_B = n\lambda, \qquad (n = 1, 2, ...) \tag{4.2}$$

where λ is the wave-length of the x-ray. The intensity of the superlattice peaks is determined by the contrast in the electron density of the two layers, and by the interfacial roughness. The contrast in the electron densities of Ag (2.7732 $e^{-1}/\text{Å}^3$) and Fe (2.1164 $e^{-1}/\text{Å}^3$)[1] is large, giving rise to a strong first order superlattice peak. The interfacial roughness reduces the intensity of the higher order superlattice peaks. In Fig. 4.1, the superlattice peaks can be seen up to 2^{nd} order without apparent broadening, suggesting well-defined compositional modulation along the film growth direction.

---

[1] The electron densities are obtained from "http : //www – cxro.lbl.gov/optical_constants".

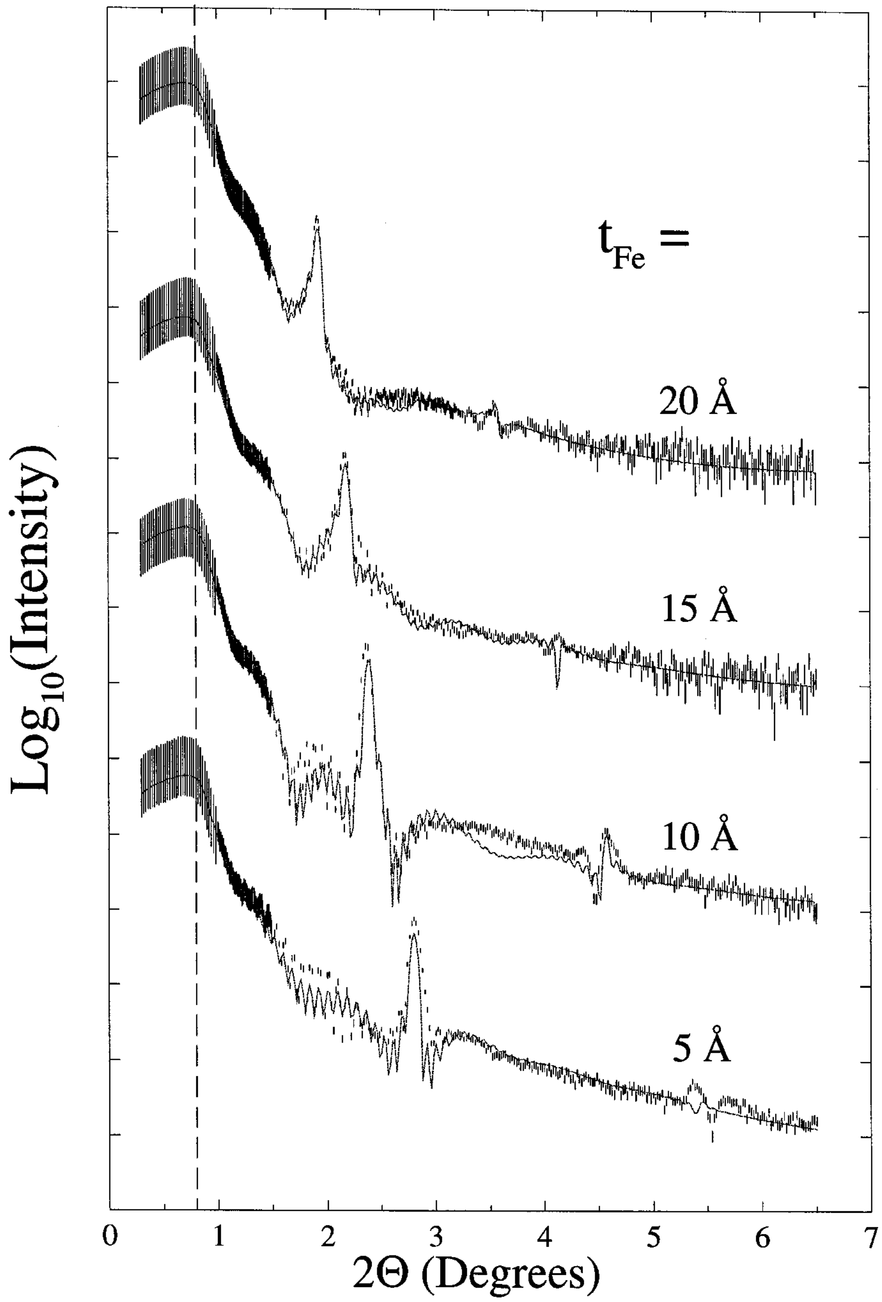

Figure 4.1: X-ray reflectivity of multilayers [Ag 30 Å/Fe t $]_{25}$/Ag 100 Å, with t = 5, 10, 15 and 20 Å. The dashed lines are the experimental data and the red lines are the fits to the data using the method described in Appendix A.1.

Quantitative analysis was carried out by calculating the x-ray reflectivity using the formalism[70] shown in Appendix $A.1$, and fitting the calculated reflectivity to the experimental data. The main structural parameters, the layer thickness (t) and root-mean-square roughness (σ) of the interface, are listed in Table 4.1.

Table 4.1: The parameters obtained from x-ray reflectivity analysis of multilayers [Ag 30 Å/Fe t]$_{25}$/Ag100Å, with nominal t = 5, 10, 15 and 20 Å. t_{Fe} and t_{Ag} are the layer thicknesses of Fe and Ag respectively. Λ is the bilayer thickness. And $\sigma_{\mathrm{Ag/Fe}}$ is the roughness at the interface with Ag layer on top of Fe, and $\sigma_{\mathrm{Fe/Ag}}$ is the roughness at the interface with Fe layer on top of Ag.

Nominal t_{Fe}	t_{Fe} (Å)	t_{Ag} (Å)	Λ (Å)	$\sigma_{\mathrm{Ag/Fe}}$ (Å)	$\sigma_{\mathrm{Fe/Ag}}$ (Å)
5	4 ±1	29 ±1	33.0 ±1	8.0 ±0.4	14 ±2
10	9.7 ±0.8	29.8 ±0.8	40 ±1	7.4 ±0.1	15 ±3
15	13 ±2	31 ±2	44 ±3	17 ±2	8.9 ±0.2
20	18 ±2	33 ±2	51 ±3	18 ±1	11.4 ±0.2

σ is a measure of the degree of roughness at a non-ideal interface. There are two types of roughness: inter-diffusion, and geometric roughness. For a purely diffuse interface, the electron density varies smoothly along the film growth direction x, and can be described by an electron profile function $\rho_0 P(\mathrm{x})$, where ρ_0 is the electron density of the bulk material, and $P(\mathrm{x})$ is the interface profile function with values between 0 and 1. For an interface with purely geometric roughness, although abrupt transitions from one electron density to another occur at different positions of x, the interface can still be represented by a simple analytical function $P(\mathrm{x})$. The reason is that the measured x-ray reflectivity samples the average variation of the electron density across the interface over the area of the x-ray beam. For a purely diffuse interface, the derivative of $P(\mathrm{x})$ is the composition gradient. While for an interface with pure geometric roughness, the derivative of $P(\mathrm{x})$ is the probability distribution of the height deviations from the average interface[79]. Abdouche[80] has modeled the x-ray reflectivity from a 500 Å Ni film deposited on Si/SiO$_2$ by magnetron sputtering and fitted the calculation to the experimental reflectivity profile. Among four types of profiles $P(\mathrm{x})$: linear, error function, hyperbolic-tangent and arc-tangent, the error function worked best in the fitting for describing the interface structure. $P(\mathrm{x})$ for an interface described by an error function and a mean interface with vacuum at origin, is given by[79]

$$P(\mathrm{x}) = \frac{1}{\sqrt{2\pi}\sigma}\int_{-\infty}^{\mathrm{x}} \mathrm{e}^{-\frac{\mathrm{u}^2}{2\sigma^2}}\mathrm{du} = \frac{1}{2}\left[1+\mathrm{erf}(\frac{\mathrm{x}}{\sqrt{2}\sigma})\right] \qquad (4.3)$$

The derivative of Eqn. (4.3) is a Gaussian. In order to show how the electron density profile changes with σ, effective electron density profiles for a 100 Å Fe layer sandwiched by Ag layers with $\sigma = 0 - 100$ Å are given in Fig. 4.2. For an ideally flat and abrupt interface ($\sigma = 0$), the electron density profile is a step function. The effect of a small σ is to smooth out the transition at the interface. As σ increases to half of the layer thickness, the interface extends into the center of the layers, and the difference between the effective electron densities in Fe and Ag layers is reduced.

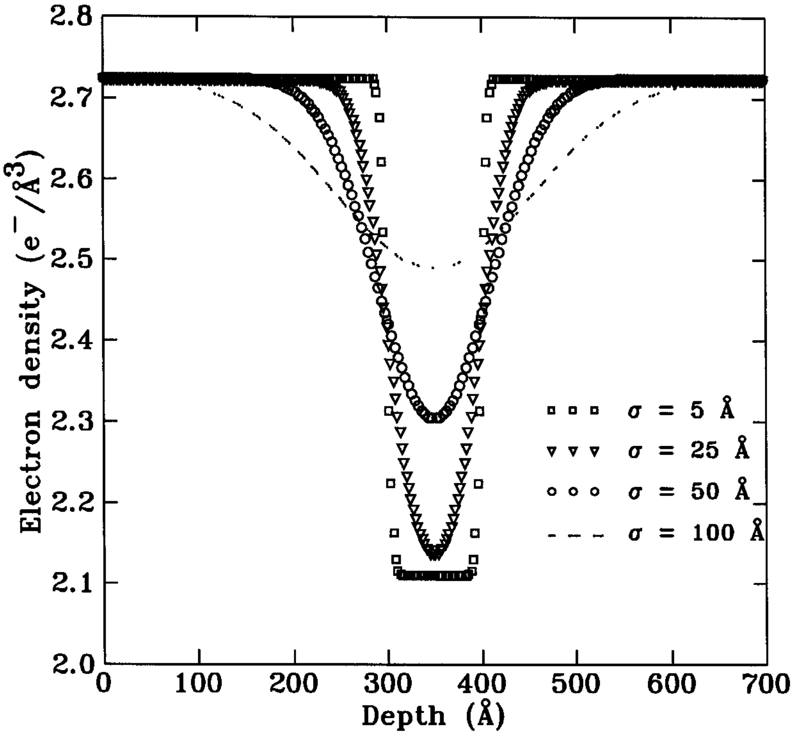

Figure 4.2: The effective electron density profiles of a 100 Å Fe layer sandwiched by Ag layers with different interface roughness, σ = 5, 25, 50, and 100 Å, are used to show the intnerface structure described by an error function. The effective electron densities of bulk Fe and Ag are 2.1164 $e^-/Å^3$ and 2.7732 $e^-/Å^3$ respectively.

Since the formalism[70] used in the fitting of small-angle x-ray profiles assumes the interface profile function at interfaces is an error function, the electron density profiles of multilayers [Ag 30 Å/Fe t]$_{25}$/Ag 100Å were generated using error functions (Eqn. (4.3)) and the parameters obtained from the fits to the x-ray reflectivity (Table 4.1). Since all the bilayers in each multilayer are identical, Fig. 4.3 displays the electron density profiles of multilayers with a period of N = 10. As can be seen, the effect of the roughness, which is comparable, and in some cases even larger than the Fe thickness, is to reduce the effective electron densities in the Ag layers from the bulk Ag value of 2.7732 $e^-/Å^3$, while enhancing the effective electron densities in the Fe layers from the bulk Fe value of 2.1164 $e^-/Å^3$, implying the Fe profile extends to the Ag layer, and the Ag profile extends to the Fe layer.

4.1.2 X-ray Diffraction

High-angle x-ray diffraction measurements provide information about the atomic ordering or crystallographic structure along the sample growth direction. The x-ray diffraction intensity as a function of twice the incident angle is shown in Fig. 4.4 for multilayers [Ag 30 Å/Fe t]$_{25}$/Ag 100Å with t = 5, 10, 15 and 20 Å.

At room temperature, equilibrium bulk Fe has a body-centered-cubic (*bcc*) structure with lattice constant a = 2.8655 Å and Ag has a face-centered-cubic (*fcc*) structure with lattice constant a = 4.0863 Å. The Bragg peaks for bulk Fe and Ag are indexed as shown in Fig. 4.4. The high intensity peaks with sharp features in the $2\theta = 50^\circ - 75^\circ$ range are Bragg peaks originating from the Si substrate. The Bragg peaks with 2θ positions at 38.15° and 81.64°, corresponding to Ag(111) and Ag(222) diffraction peaks, are from the multilayers. It suggests a predominant texture with Ag(111) orientated along the film growth direction. Since Fe typically grows along an axis perpendicular to its densest packed layer[81], then Fe(110) is expected to stack on Ag(111). As the Ag layers are thicker than the Fe layers, and the square of the atomic scattering factor of Ag is about 5 times that of Fe, the Fe(110) diffraction peak at $2\theta = 44.6^\circ$ is relatively weak. The satellite peaks around the main peak indicate a well-defined periodic structure.

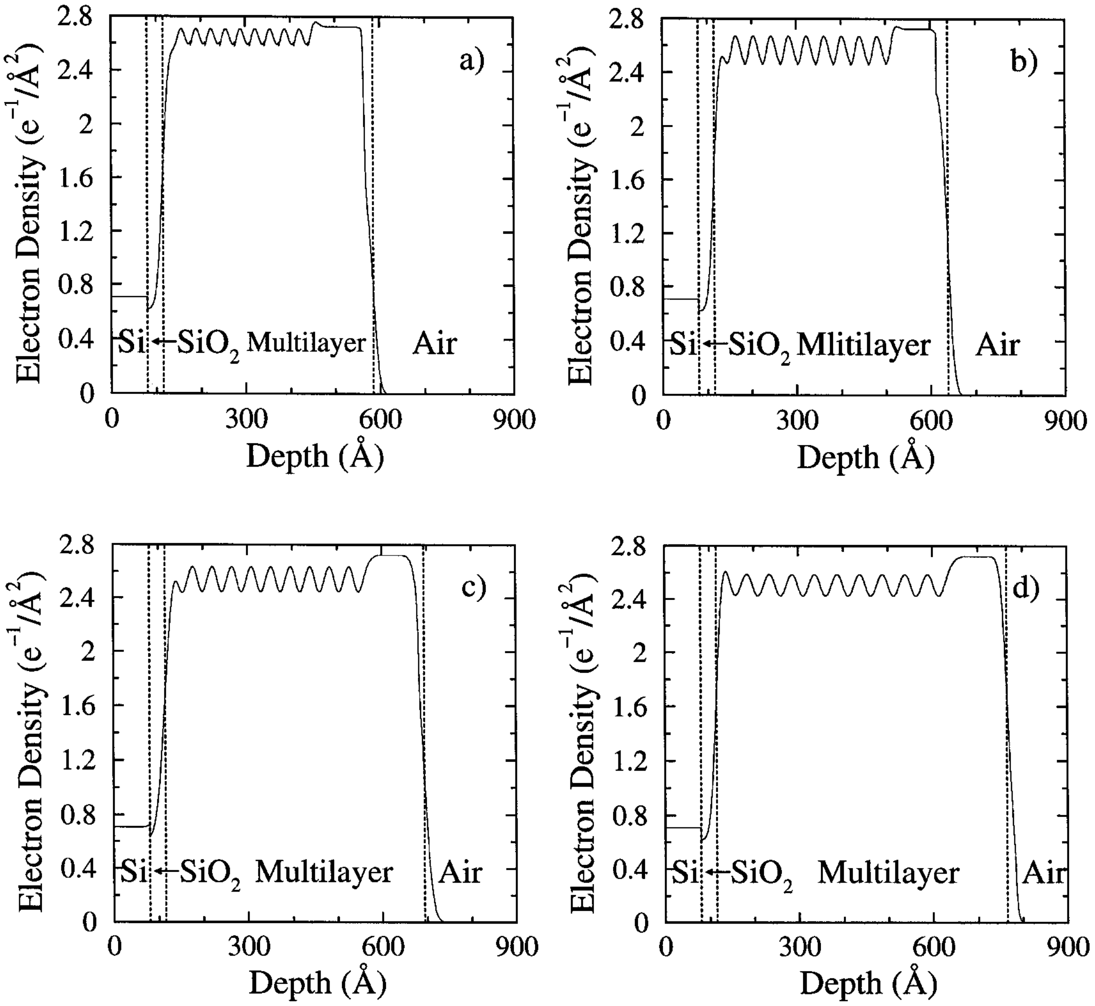

Figure 4.3: The effective electron density profiles (solid lines), generated using the parameters obtained from fitting to the small-angle x-ray reflectivity (Table 4.1) and using the error function to describe the interface structure, for multilayers [Ag 30 Å/Fe t]$_{10}$/Ag 100Å with a) t = 5 Å, b) t = 10 Å, c) t = 15 Å, and d) t = 20 Å. The dotted lines indicate the mean position of the Si/SiO$_2$ interface, SiO$_2$/multilayer interface, and multilayer/air interface.

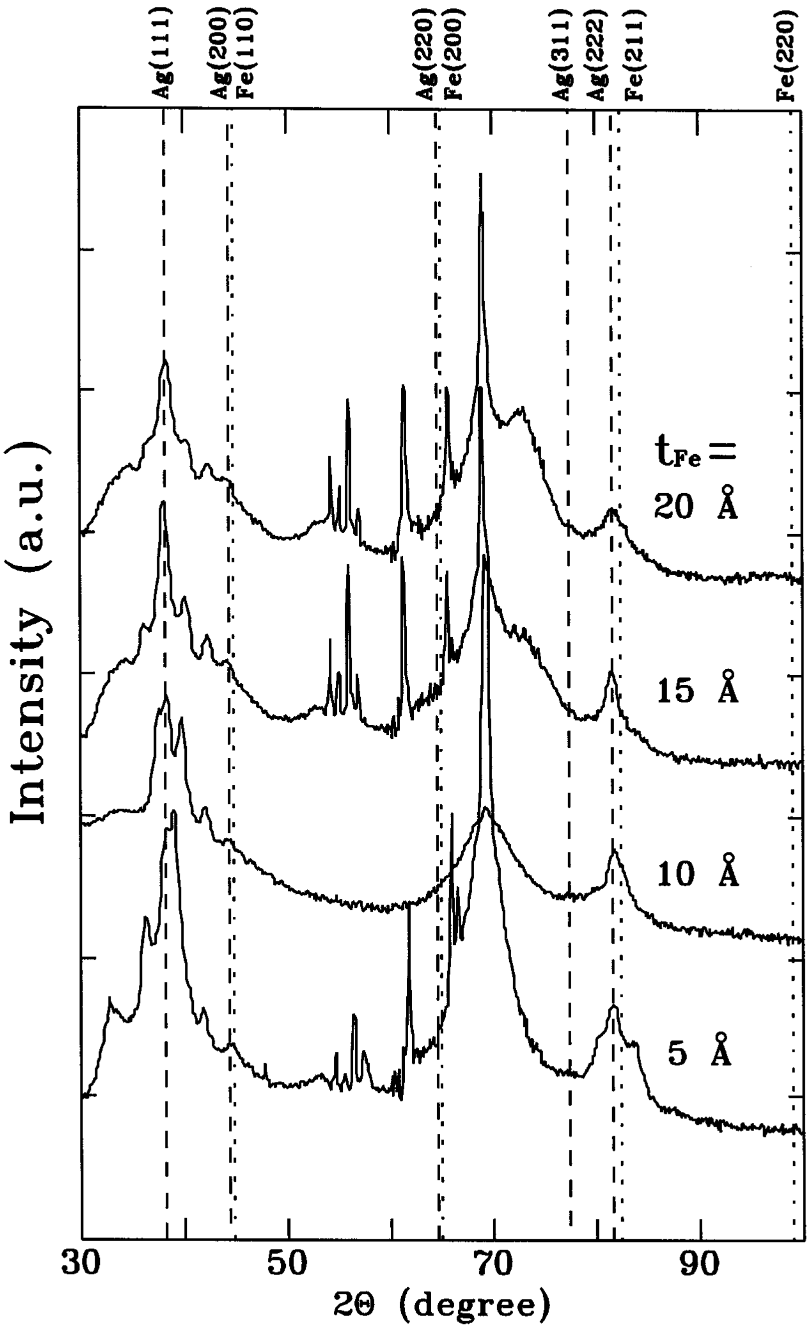

Figure 4.4: The high-angle x-ray diffraction of multilayers [Ag 30 Å/Fe t]$_{25}$/Ag 100Å with t = 5, 10, 15 and 20 Å. The experimental data are displaced vertically for clarity without altering the scale.

The x-ray diffraction profiles around the Ag(111) diffraction peak were fitted using a kinematic diffraction formalism[71] (see section 3.2.1), as shown in Fig. 4.5. The d-spacing of Ag obtained from these fits agrees with the d-spacing of bulk Ag(111) planes (2.3592 Å). For samples with t_{Fe} = 10, 15, and 20 Å, the d-spacing of Fe agrees with the interplanar spacing of (110) planes (2.0269 Å) of bulk *bcc* Fe. While for samples with t = 5 Å, the d-spacing is expanded by 9±3 %, suggesting lattice distortion along the epitaxy. The width of the fluctuations in the interface distance and interplanar spacing are found to be very small (< 0.2 Å), indicating that the interface, Ag and Fe layers have a high crystalline order. It can be concluded that the Fe layers have preferential Fe(110) orientation perpendicular to the film plane, and the d-spacing is expanded for the sample with the thinnest Fe layers.

The Fe and Ag layer thicknesses and the bilayer thicknesses calculated using the number of atomic layers, d-spacing and interface distance from fits to the high-angle x-ray diffraction profiles, are listed in Table 4.2. The values of bilayer thicknesses are in good agreement with those obtained from fits to the small-angle x-ray reflectivity data except for the sample with the thinnest Fe layers as discussed above.

Table 4.2: The parameters obtained from the analysis of high-angle x-ray diffraction data of multilayers [Ag 30 Å/Fe t]$_{25}$/Ag 100Å with t = 5, 10, 15 and 20 Å. t_{Fe} and t_{Ag} are the layer thickness of Fe and Ag in units of Å and atomic layers respectively, and Λ is the bilayer thickness.

Nominal t_{Fe}	t_{Fe} / Atomic Layers	t_{Ag} / Atomic Layers	Λ (Å)
5 Å	6.5 ± 0.2 Å (3 AL)	28.3 ± 0.5 Å (12 AL)	34.8 ± 0.7 Å
10 Å	10.3 ± 0.8 Å (5 AL)	31 ± 1 Å (13 AL)	41 ± 2 Å
15 Å	14.3 ± 0.6 Å (7 AL)	30.7 ± 0.8 Å (13 AL)	45 ± 1 Å
20 Å	17 ± 2 Å (8 AL)	31 ± 2 Å (13 AL)	48 ± 4 Å

4.1.3 *Transmission Electron Microscopy*

TEM provides a direct observation of the microstructure of the multilayers. The Fe (Ag) jump ratio images, obtained using K-edge electrons of Fe (Ag), have been

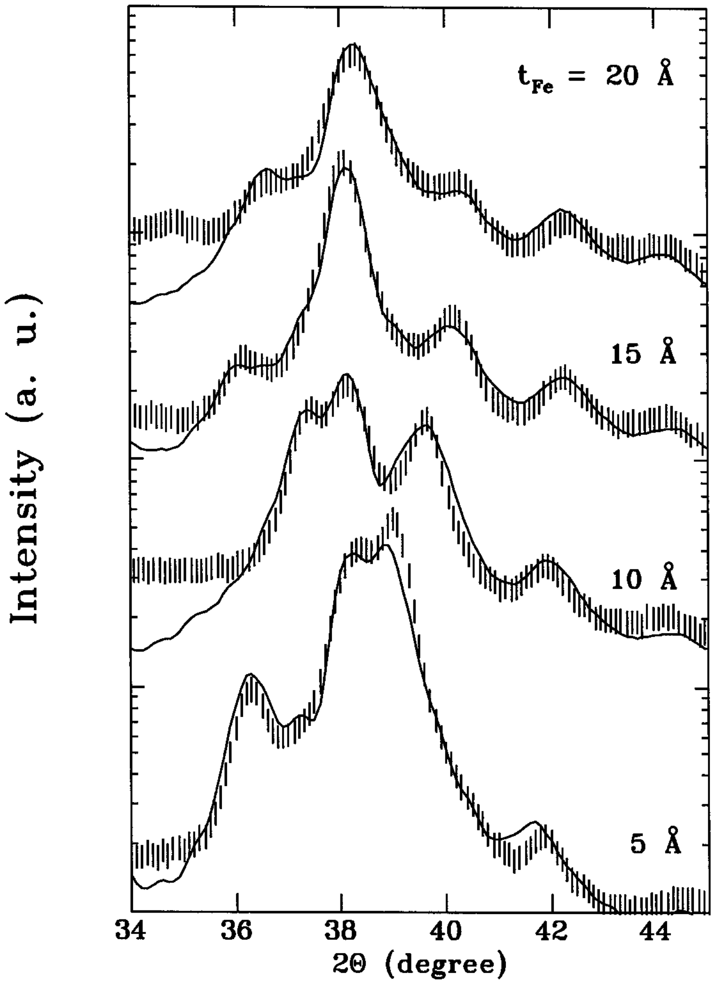

Figure 4.5: The high-angle x-ray diffraction profiles of multilayers [Ag 30 Å/Fe t]$_{25}$/Ag 100Å with t = 5, 10, 15 and 20 Å. The vertical lines are experimental data, and the solid lines are calculations.

obtained for the [Ag 30 Å/Fe t]$_{25}$/Ag 100Å multilayers and illustrated in Fig. 4.6 and Fig. 4.7. In each Fe jump ratio image, the bright layers of the same thickness correspond to Fe and the dark layers to Ag, while in the Ag jump ratio images, bright layers are Ag and the dark ones Fe. 25 bilayers are visible for samples with t_{Fe} = 10 and 15 Å, while part of the sample with t_{Fe} = 20 Å is missing due to the damage during cross-section sample preparation. The image of the sample with t_{Fe} = 5 Å is blurry since 5 Å is close to the limit of the TEM resolution. The Fe layers in samples with Fe thickness of more than 5 Å are clearly continuous, while the condition of the Fe layers with thinnest Fe thickness of 5 Å can not be determined due to the image quality. The waviness of the Fe layers close to the substrate (left side) is relatively moderate, while the waviness increases as the Fe layers approaching the surface, demonstrating the effect of cumulative roughness in the multilayers. The thick and bright layer of about 35 Å is the natural SiO_2 layer on top of the Si substrate. Including this SiO_2 layer in the reflectivity calculation does not make a noticeable difference for x-rays, since the electronic density of SiO_2 of 0.6713 $e^{-1}/\text{Å}^3$ is very close to that of Si (0.7142 $e^{-1}/\text{Å}^3$), but will be important for the fittings of the neutron reflectivity of Pd/Fe multilayers as mentioned in section 5.4.

Quantitative analysis of the layer thickness was carried out using the intensity profiles of the selected areas marked in Fig. 4.6 and Fig. 4.7. The intensity profiles are shown in Fig. 4.8 and Fig. 4.9. For the intensity profiles of Fe jump ratio images, full width at half maximum (FWHM) was first determined for each selected peak, and the average value of the FWHM was taken as the average Fe thickness. The bilayer thickness was determined by dividing the distance between the peaks at the two ends of the selected area by (N−1), N being the number of peaks in the selected area. The intensity profiles of Ag jump ratio images were analyzed in a similar way to obtain the Ag thickness and bilayer thickness, except for the sample with 5 Å Fe layers due to poor image quality.

The parameters of the thicknesses from analysis of the intensity profiles as described above are listed in Table 4.3. The bilayer thicknesses Λ obtained from analysis

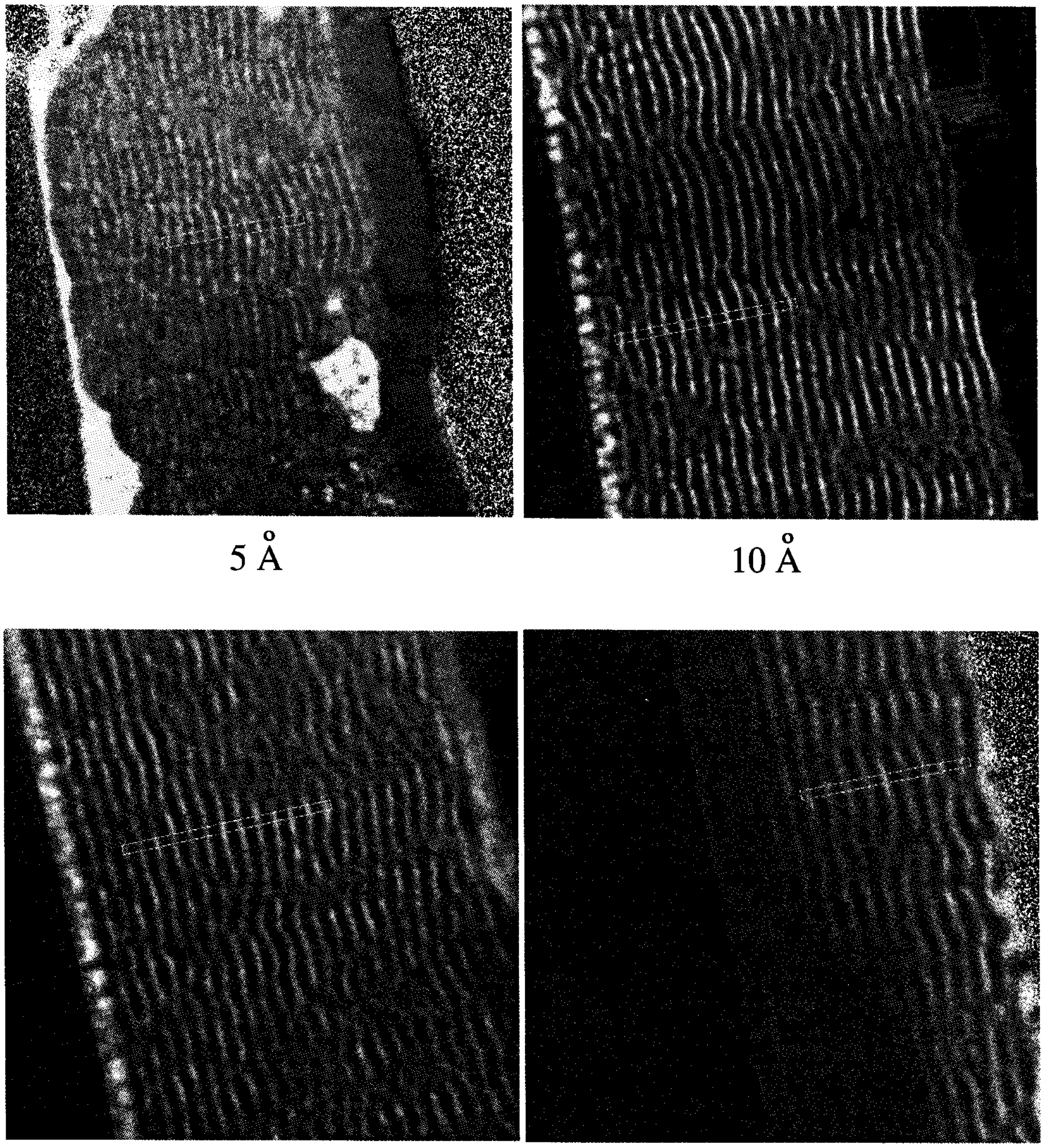

5 Å 10 Å

15 Å 20 Å

Figure 4.6: The Fe jump ratio images of [Ag 30 Å/Fe t]$_{25}$/Ag 100Å with t = 5, 10, 15 and 20 Å. The selected rectangular regions, enclosed by dashed lines, are used to generate the intensity profiles shown in Fig. 4.8.

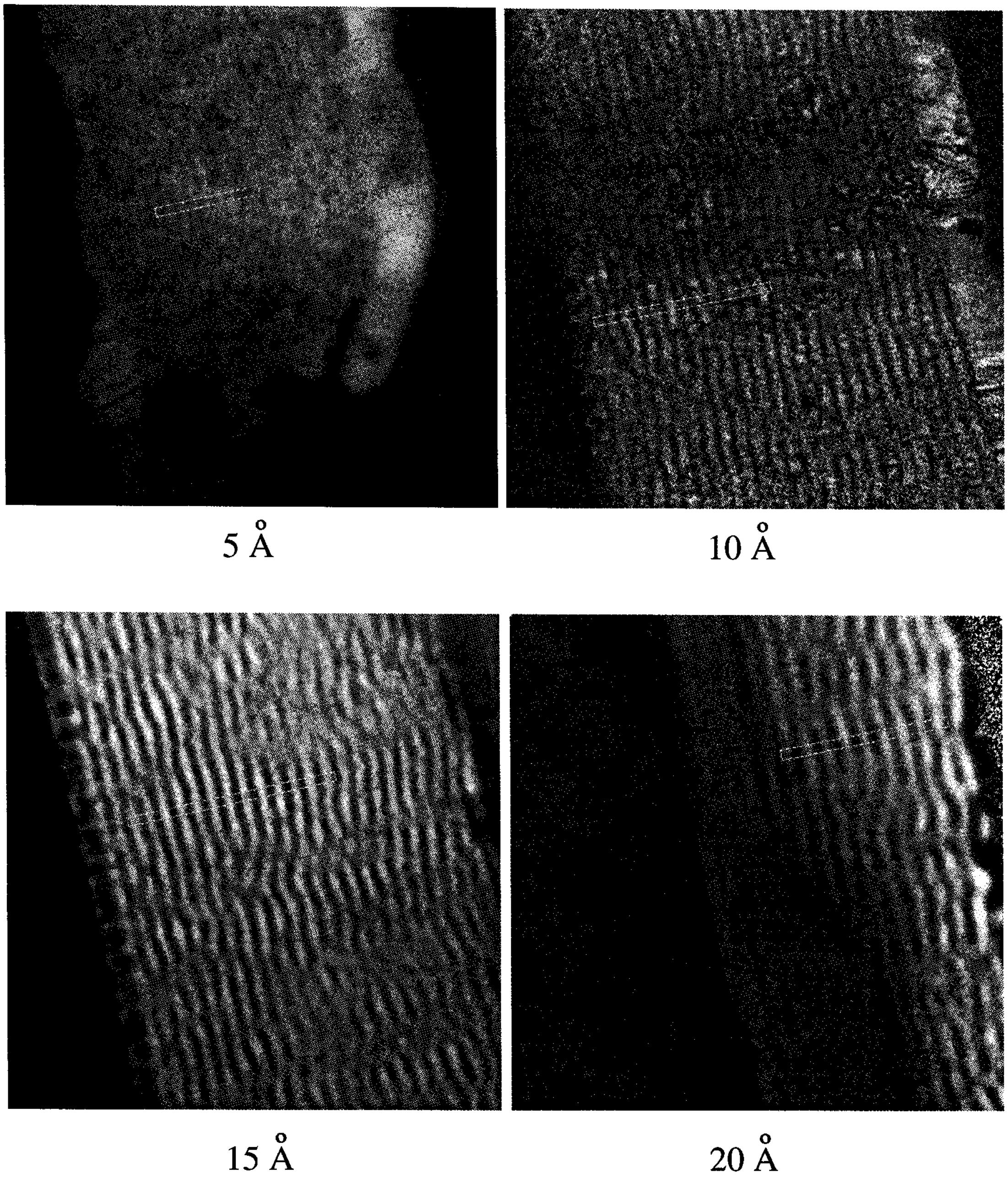

5 Å 10 Å

15 Å 20 Å

Figure 4.7: The Ag jump ratio images of [Ag 30 Å/Fe t]$_{25}$/Ag 100Å with t = 5, 10, 15 and 20 Å. The selected rectangular regions, enclosed by dashed lines, are used to generate the intensity profiles shown in Fig. 4.9.

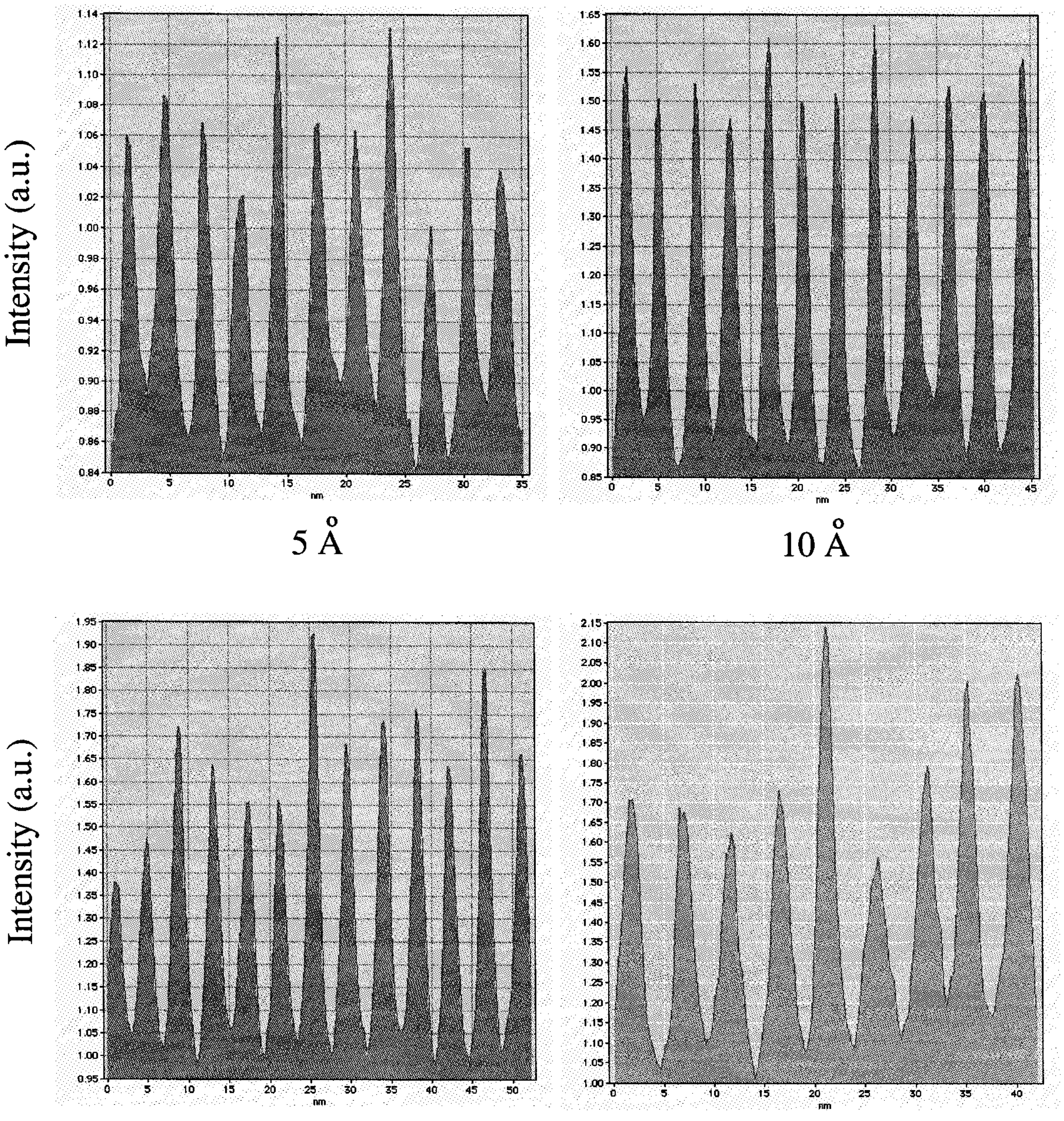

5 Å

10 Å

15 Å

20 Å

Figure 4.8: The intensity profiles, taken from the selected area in the Fe jump ratio images of [Ag 30 Å/Fe t]$_{25}$/Ag 100 Å with t = 5, 10, 15 and 20 Å.

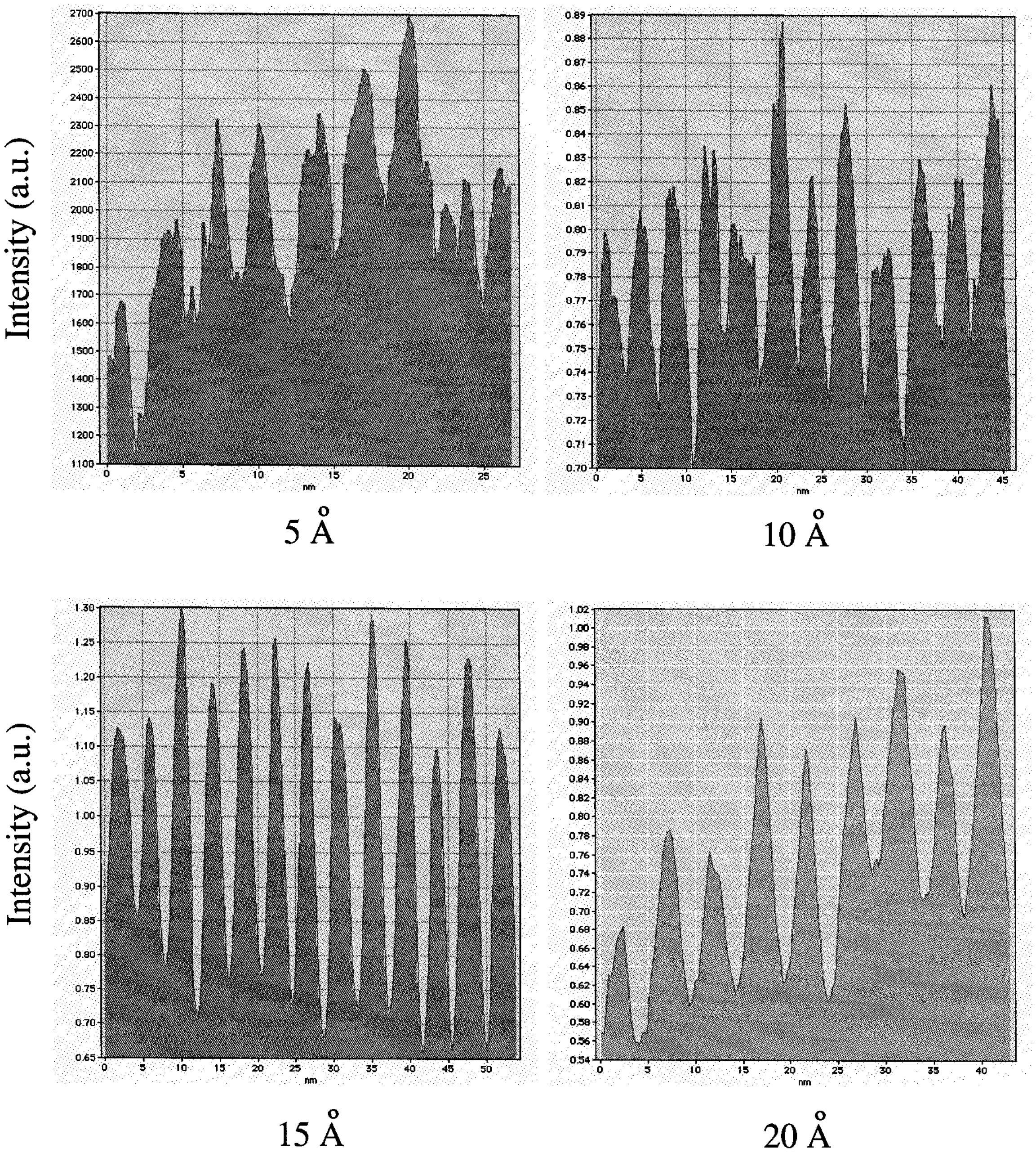

5 Å

10 Å

15 Å

20 Å

Figure 4.9: The intensity profiles, taken from the selected area in the Ag jump ratio images of [Ag 30 Å/Fe t]$_{25}$/Ag 100 Å with t = 5, 10, 15 and 20 Å.

of Fe and Ag jump ratio images agree within error. The sums of Fe thickness and Ag thickness obtained from Fe and Ag jump ratio images respectively are in good agreement with the values of Λ for the samples with nominal t_{Fe} = 10, 15 and 20 Å. However, it should be noted that taking the FWHM of an intensity profile of a particular element as layer thickness is not very precise and may not provide accurate values. This is because the value of FWHM of a peak in an intensity profile depends on the sharpness of the peak and the background of the peak, both of which are dependent on the quality of the image. Choosing the background, which varies from one peak to another, is also subjective. However, the bilayer thickness can be accurately determined from the intensity profiles, since it is easy to identify the position of the peaks, specially when averaging over about 10 periods to reduce the error.

Table 4.3: The parameters obtained from TEM analysis of multilayers [Ag 30 Å/Fe t]$_{25}$/Ag 100Å with t = 5, 10, 15 and 20 Å using the intensity profile of Fe jump ratio images (Fe JRI) and Ag jump ratio images (Ag JRI). t_{Fe}, t_{Ag} and Λ are the Fe, Ag and bilayer thicknesses.

Nominal t_{Fe} (Å)	t_{Fe} (Å)	t_{Ag} (Å)	Λ (Å)		$t_{Fe} + t_{Ag}$ (Å)
	Fe JRI	Ag JRI	Fe JRI	Ag JRI	
5	10.2 ±0.5	-	31.8 ±0.5	-	-
10	12.6 ±0.5	26 ±1	38.6 ±0.5	38.6 ±0.5	39 ± 1
15	17.6 ±0.6	24.0 ±0.5	41.7 ±0.5	41.9 ±0.5	41.6 ± 0.8
20	21 ±1	26.5 ±0.5	47.8 ±0.5	48.2 ±0.5	48 ± 1

The values of t_{Fe}, t_{Ag} and Λ, which were obtained from the analysis of small x-ray reflectivity, high-angle x-ray diffraction and TEM data, are plotted for comparison in Fig. 4.10. Since for the sample with nominal 5 Å of Fe, the Ag thickness can not be determined from Ag jump ratio image due to the poor image quality, the Ag thickness is obtained from Fe jump ratio image by subtracting the Fe thickness from the bilayer thickness. The values of t_{Fe}, t_{Ag} and Λ obtained from fitting to the x-ray reflectivity and diffraction data agree with each other except for the sample with nominal 5 Å of Fe. The t_{Fe} and t_{Ag} obtained from analysis of TEM data do not agree with the values obtained from the x-ray diffraction: the values of t_{Fe} obtained from TEM are larger than those obtained from x-ray diffraction, and the opposite is true for t_{Ag}. However, the bilayer thicknesses obtained from all these three techniques agree within error. Since it is difficult to determine accurately the individal layer thicknesses from TEM images, in the following chapter, the Fe and Pd thicknesses were determined from the fitting to x-ray reflectivity data and used to calculate the magnetic moments.

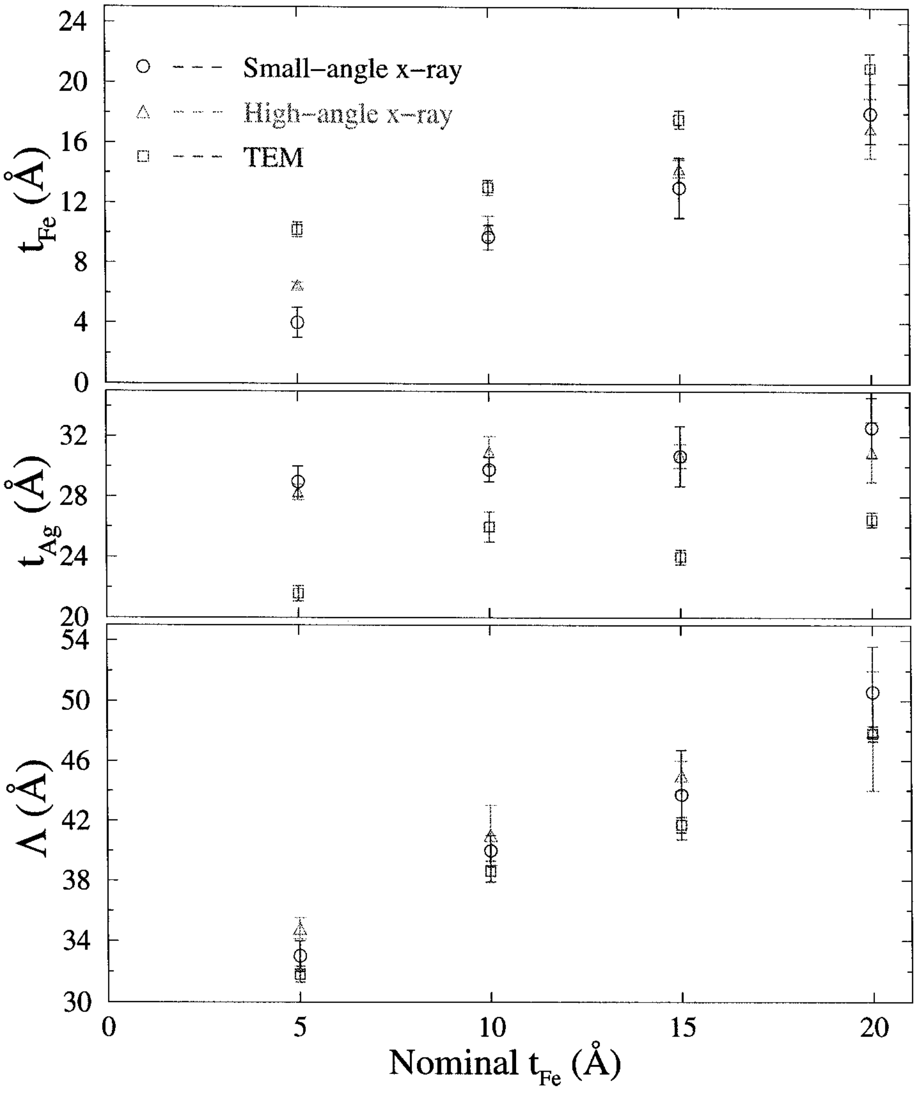

Figure 4.10: The comparison of the Ag (t_{Ag}), Fe (t_{Fe}) and bilayer (Λ) thicknesses obtained from analysis of the small-angle x-ray reflectivity (blue ○), high-angle x-ray diffraction (green △) and TEM data (red □) of multilayers [Ag 30 Å/Fe t]$_{25}$/Ag 100Å with t = 5, 10, 15 and 20 Å.

4.2 Magnetic Properties

4.2.1 Conversion Electron Mössbauer Spectroscopy

^{57}Fe Mössbauer spectroscopy provides information on the magnetism of Fe, including the hyperfine field and its temperature dependence, the orientation of the magnetic moment, and the magnetic ordering. Mössbauer spectroscopy is site selective. An experimentally obtained Mössbauer spectrum is a superposition of the subspectra from all the ^{57}Fe sites in a specimen. If the components in a spectrum can be resolved, then the hyperfine parameters for the Fe sites can be determined by fitting the subspectra. Detailed studies have been carried out using one or two atomic layers of ^{57}Fe as a probe[82, 83, 84, 85, 86]. The probe layers were grown at different depths in the Fe layer away from the interface or surface. The hyperfine parameters were thus sampled only for Fe sites where the probe was placed. Depth-dependent information about the magnetic properties of Fe has been obtained with a monolayer resolution. However, if too many Fe sites are present, their corresponding components in the spectra overlap and can not be resolved. Usually, these spectra are tentatively fitted with two components associated with Fe sites at the interface and in the interior of the Fe layers.

In this study, the [Ag 25 Å/Fe 10 Å]$_{25}$/Ag 25 Å multilayer was investigated using ^{57}Fe low-temperature conversion electron Mössbauer spectroscopy (CEMS) between 50 K and 295 K. Three spectra are shown in Fig. 4.11. The spectra are dominated by a magnetic Zeeman sextet at all temperatures, with a central doublet present when T $\geq$ 130 K. Careful inspection of the spectra shows that the line shape is asymmetric. For example, in the 130 K and 296 K spectra, line 5 is sharper and stronger than line 2, and there are more data points on the inner side of the lines than those on the outer side. These features imply the presence of more than one sextet with different δ and B_{hf}, which, when superimposed give rise to the asymmetry in the line shape.

The CEMS spectra were fitted using a non-linear least-squares routine with two sextets at all temperatures and with one additional doublet when resolvable. The sextets can be assigned to Fe sites according to their isomer shift δ. The isomer shift

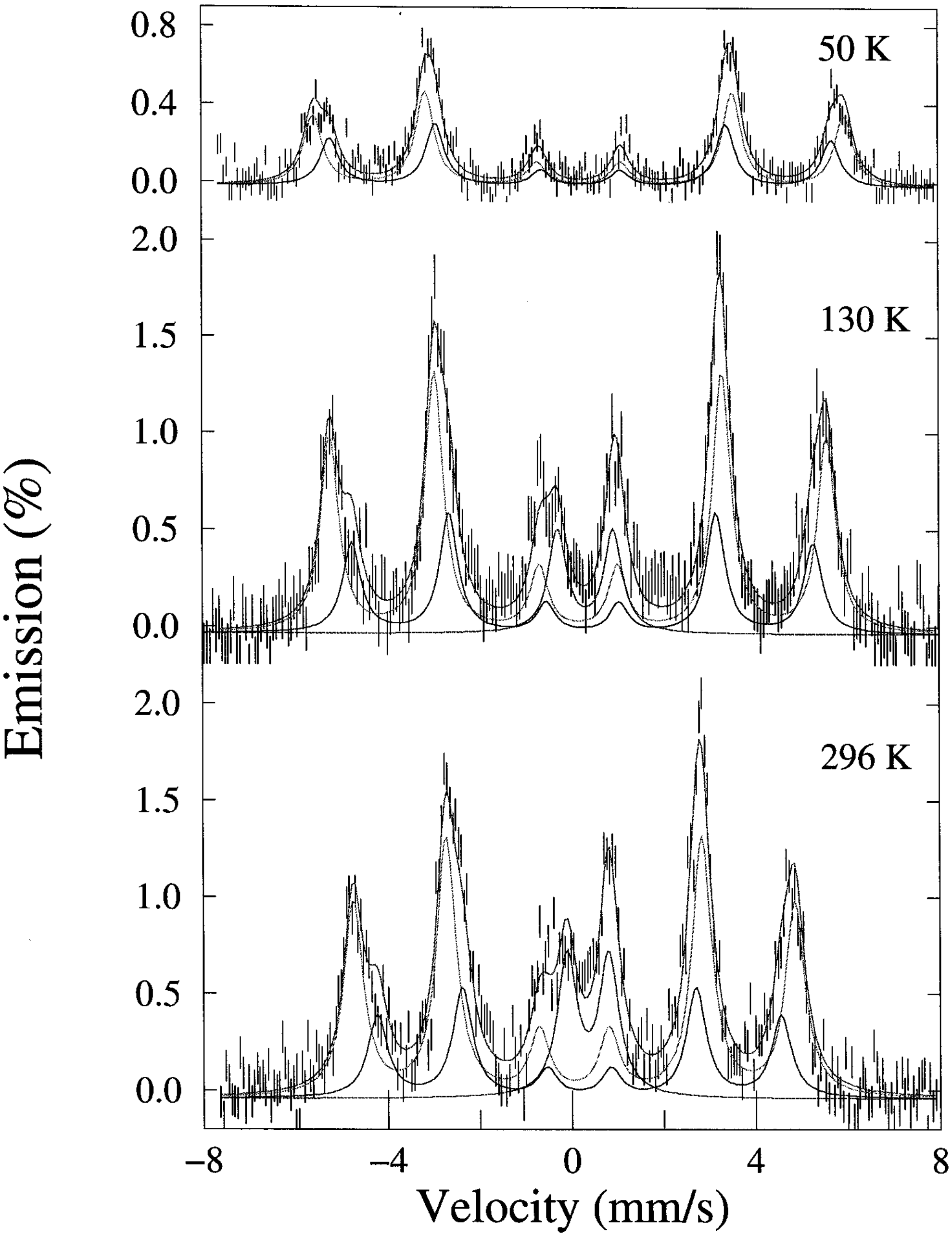

Figure 4.11: Conversion Electron Mössbauer spectra of the [Ag 25 Å/Fe 10 Å]$_{25}$/Ag 25 Å multilayer at 90 K, 130 K and 296 K. Black vertical lines are experimental data, colour lines are from fits by assuming two sextets (see the text): S_m (blue lines) and S_l (green lines) and one doublet (purple lines) for spectra measured at temperature $\geq$ 130 K, and two sextets for spectra measured below 130 K. The red lines are the overal fits.

relative to α-Fe reflects the difference between the electron density at the Fe nucleus in the sample and that of Fe in bulk α-Fe state, and this difference depends on the environment of Fe in the sample. Since both sextets from our fits have non-vanishing δ, the corresponding Fe sites are all interface-like. One of the sextets with larger δ is attributed to Fe sites with more Ag neighbors (S_m), while the other with smaller δ is attributed to Fe sites with less Ag neighbors (S_l). The hyperfine fields of the two sextets, shown by empty blue circles and filled green circles in Fig. 4.12 for S_m and S_l, follow a linear temperature dependence. The hyperfine field of S_m is slightly more temperature dependent than that of S_l. Assuming B_{hf} measures the temperature dependence of the magnetisation, (as justified in the following section), then S_m is magnetically softer than S_l. The partial contributions to the spectral area of S_m and S_l at $\mathrm{T} \leq 90$ K are 40% and 60% respectively, while above 130 K, the doublet grows at the expense of S_m, being 23 ± 1 % in the room temperature spectrum. The area weighted hyperfine field, $\overline{\mathrm{B}}_{hf} = (\mathrm{B}_{hf}^{S_m} A_{S_m} + \mathrm{B}_{hf}^{S_l} A_{S_l})/(A_{S_m} + A_{S_l})$, where A_{S_m} and A_{S_l} are the percentage contributions to the spectral area for S_m and S_l respectively, is also shown in Fig. 4.12 by red triangles.

The angle, θ, between the incident γ ray and the Fe moment, is related to the relative intensity ratio of the six lines, 3:x:1:1:x:3, where $\mathrm{x} = 4\sin^2\theta/(1+\cos^2\theta)$[77]. A ratio of 3:4:1:1:4:3 indicates an in-plane magnetisation.

The doublet component has an isomer shift (~0.3 mm/s) and quadrupole splitting (QS) (~1.0 mm/s). The relative area of the doublet decreases as the sample is cooled, and the doublet vanishes as the temperature reaches 90 K, suggesting the ordering temperature is between 90 – 130 K. Paramagnetic doublets with an ordering temperature below 77 K have also been observed in MBE-grown Fe(100)/Ag(100) systems[82], but their QS were usually smaller than 0.42 mm/s, except for a $[\mathrm{Fe}_{1.8\mathrm{AL}}/\mathrm{Ag}_{1.8\mathrm{AL}}]_{45}$ superlattice studied by Volkening[87], which gave a doublet with QS of 0.77 mm/s and δ of 0.39 mm/s. Depth profiling experiments using a monolayer of ^{57}Fe as a probe have shown that the subspectrum with an isomer shift of 0.38 mm/s and QS of 0.41 mm/s is associated with Fe atoms with zero or one nearest Ag neighbors[86].

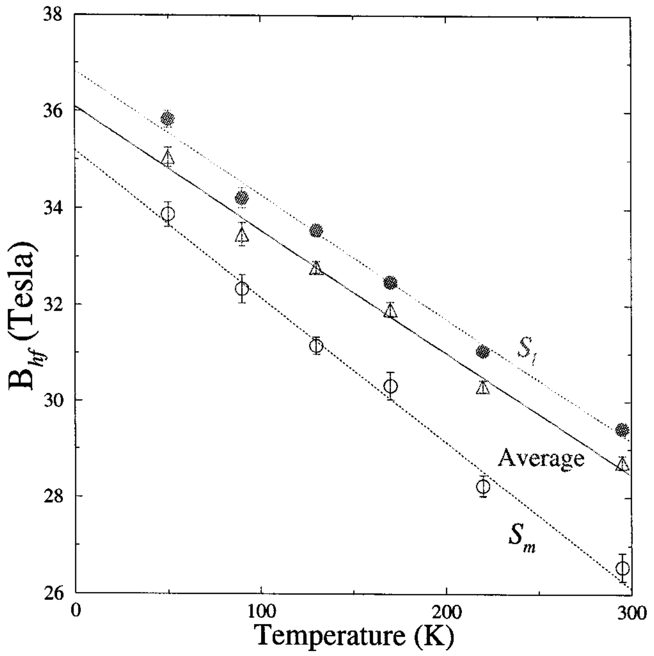

Figure 4.12: The hyperfine fields of [Ag 25 Å/Fe 10 Å]$_{25}$/Ag 25 Å obtained from fits using two sextets assumed for two Fe sites (see the text), S_m (blue ○) and S_l (green ●). The area-weighted hyperfine fields, $\overline{B}_{hf}$, (red △) also have a linear temperature dependence. The lines are the fits assuming linear temperature dependence.

The doublet could also be attributed to a tetragonal distortion of the Fe(100) atomic planes on top of Ag(100) due to the out-of-plane mismatch[88, 89, 83].

The last problem is to relate the hyperfine field to the local moment. The hyperfine field is a magnetic field at the site of the nucleus produced by the electron spin. The largest contribution to B_{hf} is the Fermi contact term[90], which is non-zero only for *s* electrons. This term reflects the spin density at the nucleus, and can be separated into core (B_{cp}) and conduction-electron (B_{ce}) contributions. The core *s* electrons, which are exchange polarized by the *d* electrons, give rise to a large and negative field, B_{cp}, at the nuclei. The negative sign indicates that the net *s*-electron spin is antiparallel to the moment of the atom. In bulk ferromagnetic metals, B_{cp} is the predominant contribution to B_{hf}, and is approximately proportional to the moment. The hyperfine field has been empirically used to obtain the magnetic moment for bulk materials assuming a simple linearity between the hyperfine field and moment. However, the linearity between the hyperfine field and moment of bulk material has been questioned for a surface or interface. According to calculations for Fe at a clean surface[6], and interfaces of Fe/Ag(001)[17] and Fe/W(110)[18], B_{cp} scales approximately with the moment with a scaling factor of –13 to –14 T per unpaired spin, regardless of the local environment. However, the conduction (valence) electrons contribution, B_{ce}, which does not scale with the moment, can be either negative or positive, depending on which kind of polarization dominates. B_{ce} is negative if the conduction *s* electrons are indirectly polarized by *d* electrons through covalent mixing between the *s*- and *d*-bands[91], while B_{ce} is positive if the conduction *s* electrons are directly coupled to the *d* electrons. For example, the calculated B_{ce} of Fe buried inside a Fe slab and at Ag/Fe interface is small and negative, while in a monolayer[17], at a clean surface of Fe(100)[6, 17], in Fe/W(110) and Ag-covered Fe/W(110)[18] systems, the calculated B_{ce} is large and positive (13 – 32 T). For those systems with an enhanced Fe moment, the Fermi contact term could be reduced in comparison with the bulk Fe value, since the positive B_{ce} exceeds the enhanced negative B_{cp} (due to the enhanced moment).

Moreover, the importance of the contribution to B_{hf} from the dipolar field (B_{dip}) at the surface or interface is not clear. The B_{dip} has three terms, the demagnetizing field (B_{d}), the Lorentz field (B_{L}) and the dipole sum within the Lorentz sphere (B_{s}). Inside a ferromagnetic sample, $\mathbf{B}_{\text{d}} = -\mu_0 N_d \mathbf{M}$, where N_d is the demagnetizing coefficient, and $\mathbf{M}$ is the magnetisation. The demagnetizing coefficient can be calculated exactly only for samples with a few special geometries, such as an ellipsoid, from which the N_d of special cases, a sphere and an infinite thin slab, can also be obtained. Inside a thin film, $N_d = 0$ and 1 for in-plane and perpendicular magnetisation respectively. The Lorentz field $\mathbf{B}_{\text{L}} = \frac{1}{3}\mu_0\mathbf{M}$, and $B_{\text{s}} = 0$ for a cubic material. So inside a Fe thin film with bulk moment, the dipole field is 0.7 T and −1.4 T for in-plane and perpendicular magnetisation, respectively. At the surface or interface, however, B_{L} is not defined, B_{s} does not vanish and depends on the orientation and the structure of the interface and on the direction of the magnetization. Christensen *et al.*[92] have calculated the B_{dip}'s of Fe(100) thin films by performing the lattice summation of the demagnetizing field and the Lorentz field. They found that for a thin film with in-plane magnetisation, the B_{dip} of surface atoms was slightly reduced by 0.17 T from the B_{dip} of the atoms inside the film (0.7 T). If the magnetization was perpendicular to the film plane, the B_{dip} of surface atoms was enhanced by 0.34 T from the value inside the film (−1.4 T). So the difference between the surface B_{dip} and the bulk B_{dip} values is not significant compared to the total hyperfine field (e.g., the hyperfine field of bulk Fe is 34 T at 0 K). However, the effect of surface roughness, which is expected to increase the local demagnetizing fields[93], was not evaluated.

As mentioned above, from the theoretical side, B_{hf} might not scale with the moment the same way as in the bulk, since the conduction electron contribution B_{ce}[6, 17, 18] and the dipolar field B_{dip}[93], are both strongly dependent on the local environment and might become prominent. On the experimental side, owing to the difficulties in determining the number of atoms in an ultra-thin film, the interface moment determined using direct magnetization measurements may not be accurate. The relationship between the experimentally determined hyperfine field and the magnetic moment at the surface is not established.

In our study, the ground state value of the area weighted B_{hf}, obtained by extrapolating B_{hf} to zero temperature assuming a linear temperature dependence, is 36.1 $\pm$ 0.3 T. If we tentatively assume that B_{hf} scales with the moment in the same way as in the bulk, the interface-like Fe moment is 2.36 ± 0.02 μ_{B}, which is enhanced by 6% compared to the bulk Fe value of 2.22 μ_{B}. On the other hand, studies[19, 20] have shown that for MBE-grown ultrathin Fe, the temperature dependence of the hyperfine field ($B_{hf}(T)/B_{hf}(0)$) is the same as that of spontaneous magnetisation ($M_s(T)/M_s(0)$), where M_s is the saturation magnetisation. In the following section, we will prove this for the sputter-deposited Ag/Fe multilayers.

4.3 Magnetometry

M_s of S_{10} was measured in the temperature range of 5 – 290 K. $M_s(T)/M_s(0)$ and $B_{hf}(T)/B_{hf}(0)$ are shown in Fig. 4.13. In the same temperature range, the $M_s(T)/M_s(0)$ and $B_{hf}(T)/B_{hf}(0)$ are superimposed on each other. It demonstrates that, for sputter-deposited ultrathin Fe layers sandwiched by Ag layers, the effective hyperfine field follows the same temperature dependence as the saturation magnetization, although sputter-deposited samples have larger interfacial roughness and possibly associated larger B_{ce} and B_{dip} relative to those of MBE-deposited thin films.

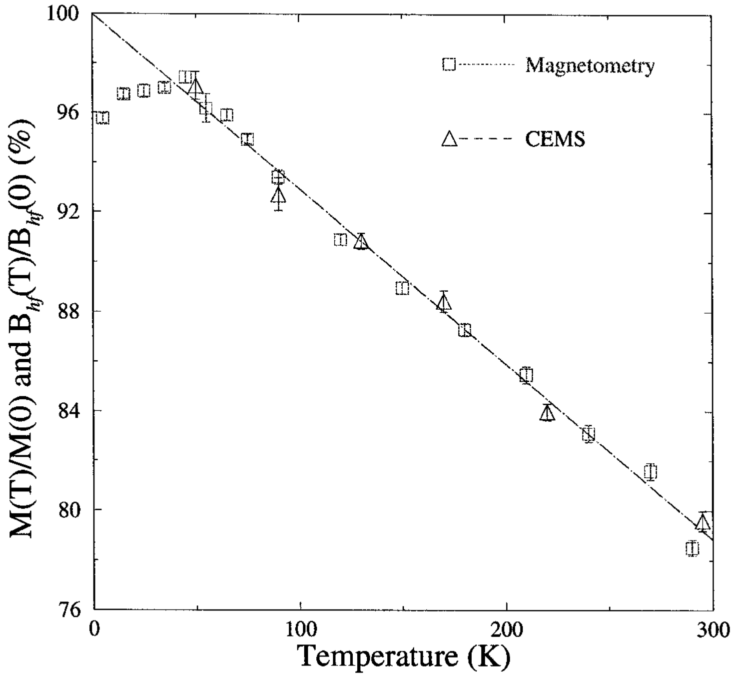

Figure 4.13: The temperature dependences of saturation magnetization (red □) and hyperfine field (blue △) in the same temperature range of 50 – 295 K are compared. The ground state saturation magnetization and hyperfine field were obtained by extrapolating the data between 50 – 295 K to 0 K, which were used to normalize the magnetization and hyperfine field data. Assuming linear temperature dependence, the red dotted line and blue dashed line are the fits to the magnetization and hyperfine field data, respectively, which superimpose on each other.

The linear temperature dependence of the saturation magnetization, reflected by $B_{hf}(T)$, is often associated with two-dimensional magnetic behavior, where the spin-wave excitations normal to the film are suppressed over an appreciable low-temperature regime[94]. In a Mössbauer study of Fe(110)/Ag(111) multilayers, J. C. Walker and *et al.* have shown that linear $B_{hf}(T)$ could either be a quasi-two-dimensional (2D) magnetic effect[95, 96], or a consequence of superparamagnetic relaxation of island structures[97]. These two behaviors can be distinguished in principle by comparative Mössbauer measurements with and without a small applied magnetic field[95]. Upon applying the field, if $B_{hf}(T)/B_{hf}(0)$ of a multilayer is not changed, the linear $B_{hf}(T)$ is due to a genuine quasi-two-dimensional behavior. But if the slope of $B_{hf}(T)/B_{hf}(0)$ is reduced by the application of field, then the linear $B_{hf}(T)$ is due to magnetic relaxation. Further CEMS measurement with applied field is required to clarify whether linear $B_{hf}(T)$ found in our Ag/Fe multilayer is the result of quasi-two-dimensionality or superparamagnetic relaxation behavior.

In this chapter, upon performing x-ray diffraction, CEMS and magnetometry studies of the relatively simple and clean system of Ag/Fe multilayers, we have confirmed that the analysis of small-angle x-ray reflectivity data provides fast and accurate determination of the bilayer thickness. We have also demonstrated that for the Fe layers in our sputtering deposited multilayers, the temperature dependence of the hyperfine field reflects the variation of saturation magnetisation of Fe with temperature. These two important and powerful experimental techniques were then applied to the more complicated system, Pd/Fe multilayers, to reveal its intriguing structural and magnetic properties.

5

Palladium Polarisation In Pd/Fe Multilayers

In this chapter, we present the results of structural and magnetic studies of Pd/Fe multilayers, and present for the first time a consistent and complete picture of the polarisation of the Pd layer in the Pd/Fe multilayer system. First, the multilayers were characterized using small and high angle x-ray diffraction measurements, from which the layer thicknesses and crystalline structure were obtained. Then the magnetic properties were investigated by combining CEMS, magnetometry and PNR measurements. The interfacial Fe thickness and the temperature dependence of the Fe moment were determined from the CEMS studies. Magnetometry measurements provided the ground state expectation value and the temperature dependence of the total moment. Removing the Fe contribution from the total moment, the Pd polarisation as a function of temperature was obtained. Finally, the value of the Pd moment, the extent of the Pd polarisation, and the value of the interfacial Fe moment were extracted from the analysis of PNR measurements at room temperature and 4.5 K.

5.1 Structural Characterization

5.1.1 Low Angle X-ray Reflectometry Results

In the study of the magnetism of an ultrathin film, structural characterization is of great importance. In addition to the preliminary requirement of ensuring a well-defined layered structure, a detailed understanding of the structural properties is essential for tailoring the magnetic properties. In the Pd/Fe study, the major concern is the Fe and Pd moment, so that knowing the number of atoms in the sample is essential for the determination of the moments. The number of atoms can only be calculated with the knowledge of crystalline orientation and the layer thickness. In addition, an interesting "wasp-waisted" feature associated with interfacial roughness was observed for the hysteresis loops (section 5.3.3). A model including the cumulative roughness effect was developed and shown to give a better description of the data than a simple model using constant roughness.

The dependence of the roughness on bilayer period

It is well known that the interfacial roughness may increase cumulatively with the bilayer period (N)[98, 99, 100]. In the process of deposition, if the adatoms do not have sufficient lateral mobility, the rate at which the surface is smoothed out is lower than the rate at which atoms are deposited, so that the roughness of the surface will increase as more material is deposited[98]. The substrate roughness will propagate into multilayer interfaces, and the interface roughness increases with N. As will be shown in the following sections, the coercive field is sensitive to N even at very small N. In order to study the cumulative effect of interfacial roughness and to find the correlation between the roughness and the magnetic properties of sputtered Pd/Fe, multilayers $[\mathrm{Pd}\ 50\text{Å}/\mathrm{Fe}\ 20\text{Å}]_{\mathrm{N}}$ with N = 5, 10, 15 and 20 were characterized using small angle x-ray reflectivity measurements. Fig. 5.1 shows the reflectivity profiles in which the superlattice peaks are visible up to 5^{th} order, due to the large contrast between the electron densities of Pd and Fe, and moderate roughness at the interfaces. The 4^{th} and 5^{th} superlattice peaks are strongest for the sample with N = 20, owing to the greater number of interfaces reflecting x-rays, and so giving rise to stronger constructive interference at these superlattice peak positions.

Quantitative analysis was carried out by fitting the calculated reflectivity to the experimental data. Two models were applied. Model I assumes that all the layers of the same kind are identical throughout a multilayer. The interfacial roughness is then an average over all the interfaces of the same kind. The plots of the fitting are shown in Fig. 5.2(a) and the structural parameters obtained from the fitting are listed in Table 5.1. The structural parameters include individual layer thicknesses

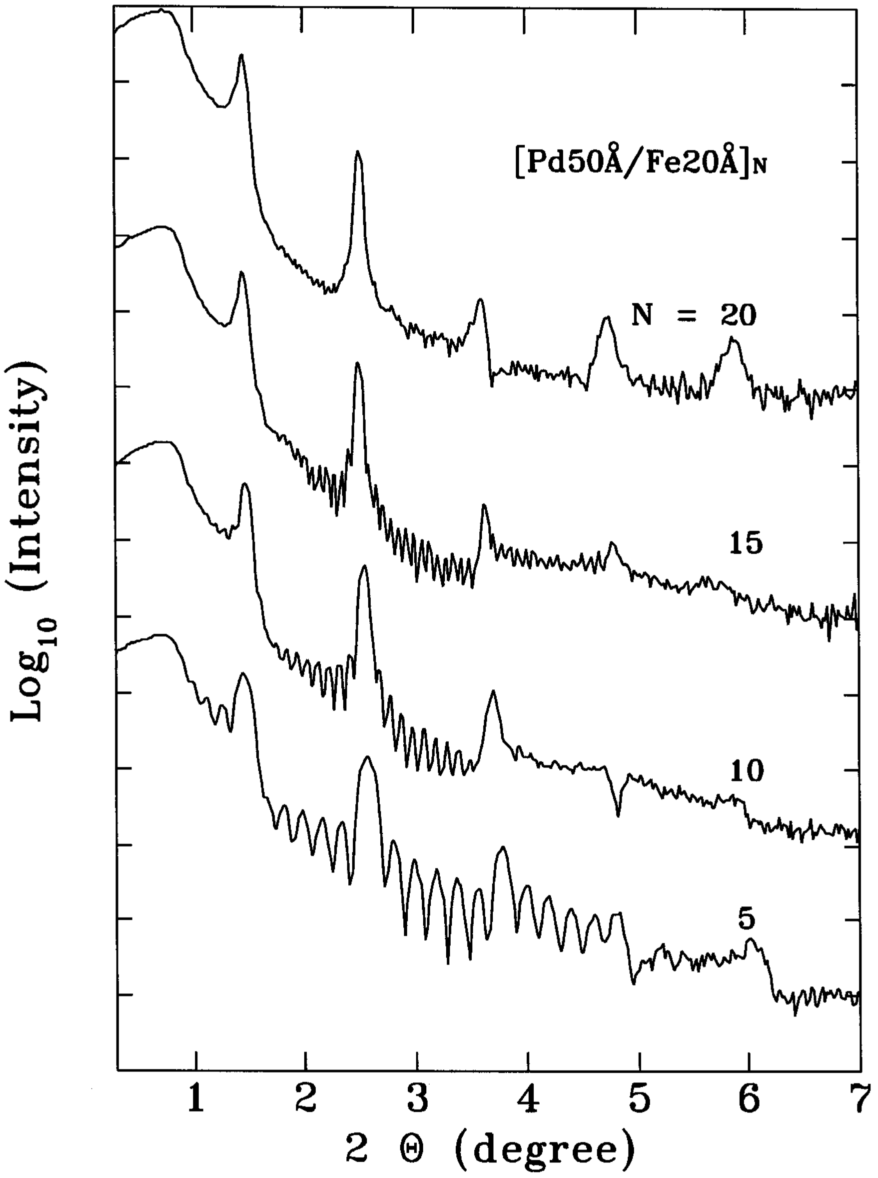

Figure 5.1: Small angle x-ray reflectivity profiles of [Pd 50 Å/Fe 20 Å]$_N$, N = 5, 10, 15 and 20 multilayers. The superlattice peaks can be seen up to the 5th order without significant broadening.

Table 5.1: The parameters obtained from fitting the x-ray reflectivity profiles of [Pd50Å/Fe20Å]$_N$ multilayers with N=5, 10, 15, 20 using model I. Λ is the bilayer thickness, t is the layer thickness, σ_s is the surface roughness, $\sigma_{Pd/Fe}$ and $\sigma_{Fe/Pd}$ are the interfacial roughness with Pd on top of Fe, and with Fe on top of Pd respectively. The Fe (Pd) layers are assumed to be identical from bottom to top.

N	Λ (Å)	t_{Fe} (Å)	t_{Pd} (Å)	σ_s (Å)	$\sigma_{Pd/Fe}$ (Å)	$\sigma_{Fe/Pd}$ (Å)	χ^2
5	73.6±0.1	20.7±0.1	52.9±0.1	6.8±0.2	6.8±0.2	5.1±0.1	2.63
10	74.3±0.5	17.5±0.5	56.8±0.5	9.2±0.1	8.4±0.4	7.3±0.2	3.83
15	76.0±0.9	20.9±0.9	55.1±0.8	10.4±0.2	9.3±0.5	9.5±0.5	4.74
20	75.9±0.6	26.4±0.6	49.5±0.6	11.6±0.1	11.2±0.4	8.8±0.3	3.81

for Pd (t_{Pd}) and Fe (t_{Fe}), bilayer thickness (Δ), surface roughness (σ_s), interfacial roughnesses for the interface with Pd on top of Fe ($\sigma_{Pd/Fe}$) and for the interface with Fe on top of Pd ($\sigma_{Fe/Pd}$). The fitting program tends to increase the surface roughness and the interfacial roughnesses in order to fit the shape of the reflectivity profiles as N increases. However, the large roughness washes out the high order supperlattice peaks in the calculated profiles for the multilayers with N=15 and 20. χ^2 also increases with N, suggesting poor fitting for the sample with large N.

In order to improve the fitting, model II was used to simulate the cumulative effect of roughness. In this model, $\sigma_{Pd/Fe}(\sigma_{Fe/Pd})$ has an initial value of $\sigma_{Pd/Fe}(1)$ ($\sigma_{Fe/Pd}(1)$)for the layer nearest to the substrate; as the bilayer number increases, $\sigma_{Pd/Fe}(\sigma_{Fe/Pd})$ increases linearly with a ratio of $\Delta\sigma_{Pd/Fe}(\Delta\sigma_{Fe/Pd})$. So for the ith layer counting from the substrate, the roughness is,

$$\sigma(i) = \sigma(1) + (i-1) \times \Delta\sigma. \tag{5.1}$$

The spectra calculated using the two different models are shown as solid lines in Fig. 5.2(b). The parameters obtained from model II are listed in Table 5.2. Visual inspection of the agreement between the calculations (red solid lines) and the experimental spectra (black vertical lines) at the high order superlattice peaks suggests improved fitting using model II for multilayers with N = 15 and 20. The smaller values of χ^2 for the multilayers with N $\geq$ 10 in Table 5.2 confirms that model II gives

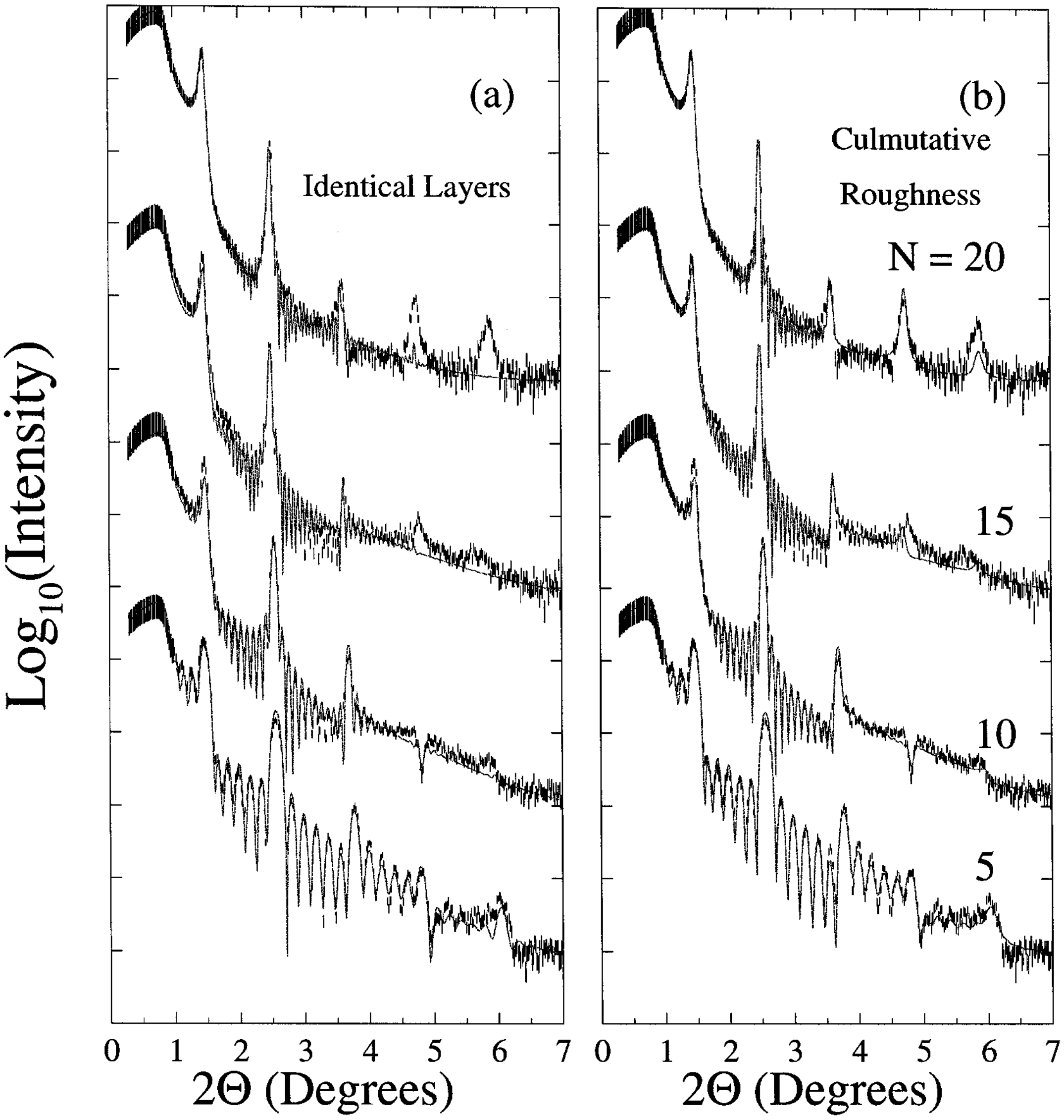

Figure 5.2: Fits to the x-ray reflectivity profiles of [Pd 50 Å/Fe 20 Å]$_N$, N = 5, 10, 15 and 20 multilayers using two different models: (a) model I assumes that all the layers of the same kind are identical all across a multilayer; (b) model II includes the effect of cumulative roughness into the reflectively calculation. The black dashed lines are experimental data and the red solid lines are the calculations.

Table 5.2: The parameters obtained from fitting the x-ray reflectivity profiles of [Pd50Å/Fe20Å]$_N$ multilayers, N=5, 10, 15, 20, using model II. Λ is the bilayer thickness, t is the layer thickness, σ_s is the surface roughness, $\sigma_{Pd/Fe}$ and $\sigma_{Fe/Pd}$ are the interfacial roughness of with Pd on top of Fe, and with Fe on top of Pd respectively. The cumulative interfacial roughnesses are modeled in such a way, from the bottom to top, that the ith layer has a roughness of $\sigma(1)$ + (i−1)×$\Delta\sigma$. .

N	Λ (Å)	t_{Fe} (Å)	t_{Pd} (Å)	σ_s (Å)	$\sigma_{Pd/Fe}(1)$ (Å)	$\Delta\sigma_{Pd/Fe}$ (Å)	$\sigma_{Fe/Pd}(1)$ (Å)	$\Delta\sigma_{Fe/Pd}$ (Å)	χ^2
5	73.5±.1	20.5±.1	53.0±.1	7.0±.1	5.3±.2	.58±.08	4.6±.1	.40±.05	2.36
10	74.3±.2	18.0±.2	56.3±.2	9.9±.1	6.4±.2	.42±.05	5.7±.1	.33 ±.03	2.60
15	76.0±.2	21.9±.2	54.1±.2	10.9±.1	5.8±.2	.40±.03	6.3±.2	.28±.02	2.81
20	75.9±.6	26.1±.3	49.8±.3	12.1±.1	4.6±.1	.37±.02	6.3±.2	.22±.02	2.73

better fits. Even though, the bilayer thickness and Fe and Pd thicknesses obtained using the two different models are consistent within error.

For each multilayer, $\sigma(1)$'s for the films are not consistent within error, neither are the values of $\Delta\sigma$. The discrepancy could be due to the fact that the linear increase in the roughnesses is only a simple approximation of the cumulative roughnesses. In a multilayer, the roughness initially might increase faster with N, while the increment in roughness slows down at large N, as suggested by the values of $\Delta\sigma$ which decrease as N increases. The fits are not sensitive enough to give a detailed description of how the roughness increases. However, the layer thicknesses are found to be independent on the model used. For simplicity, the model I using a constant roughness is applied to get the structural parameters in the remaining of the chapter.

Since the roughness increases with N cumulatively, in principle multilayers with small numbers of N ($N \leq 5$) should be used to ensure homogeneity. However, this is at the cost of having smaller amount of material and thus lower signals in some measurements such as magnetometry. When using samples with large N, care has to be taken to distinguish between properties due to non-uniform roughness present in the multilayers and their intrinsic properties.

The study of the multilayers for magnetometry measurements

The reflectivity profiles of three series of multilayers for magnetometry measurements with nominal forms of [Pd 50 Å/Fe t Å]$_{25}$ (t_{Fe} = 5 – 40 Å), [Pd t Å/Fe 20 Å]$_5$ (t_{Pd} = 5 – 50 Å) and [Pd t Å/Fe 15 Å]$_{25}$ (t_{Pd} = 10 – 55 Å) are shown in Fig. 5.3, Fig. 5.4 and Fig. 5.5 respectively. For the multilayers with 25 bilayers, the superlattice peaks are observed up to 6^{th} order without significant broadening, indicating a well-defined compositional modulation along the film growth direction. The interfacial roughness gradually reduces the intensity of the higher order superlattice peaks. It is interesting to see that the 3^{rd} and 5^{th} superlattice peaks in the profiles of multilayers with t_{Fe} = 25 and 35 Å respectively are significantly suppressed. This is because the ratios of the Pd and Fe layer thicknesses in these two samples are close to the ratios 2:1 and 3:2, which give rise to destructive interference at the 3^{rd} and 5^{th} superlattice peaks respectively. The small intensity oscillations due to the interference of reflected x-rays from the top and bottom interfaces of a multilayer are not visible for multilayers with total thickness more than $\sim$ 1000 Å. For the multilayers [Pd t Å/Fe 20 Å]$_5$, with 5 bilayers, the small intensity oscillations are clearly visible because the total thickness is so small, while the superlattice peaks are broader due to fewer bilayers contributing to the interference.

The structural parameters obtained from fitting the small angle x-ray reflectivity profiles of [Pd 50 Å/Fe t Å]$_{25}$ multilayers are listed in Table 5.3. The Fe thickness from the fits does not increase quite linearly as the nominal Fe thickness increases, and some fluctuations in the Pd thickness is also obtained. However, if one plots the bilayer thickness as a function of nominal Fe thickness, a straight line is obtained, suggesting a constant Pd thickness and a linear increment in the Fe thickness. Since the fits to the small-angle x-ray profiles yield accurate bilayer thicknesses, while the individual layer thicknesses are somewhat in question, more accurate values for the Fe and Pd thicknesses were determined in the following way. The bilayer thickness versus nominal Fe thickness was fitted using a straight line, the intercept of 53 ± 1 Å is the Pd thickness, and the slope of the line corresponds to the Fe layer thickness

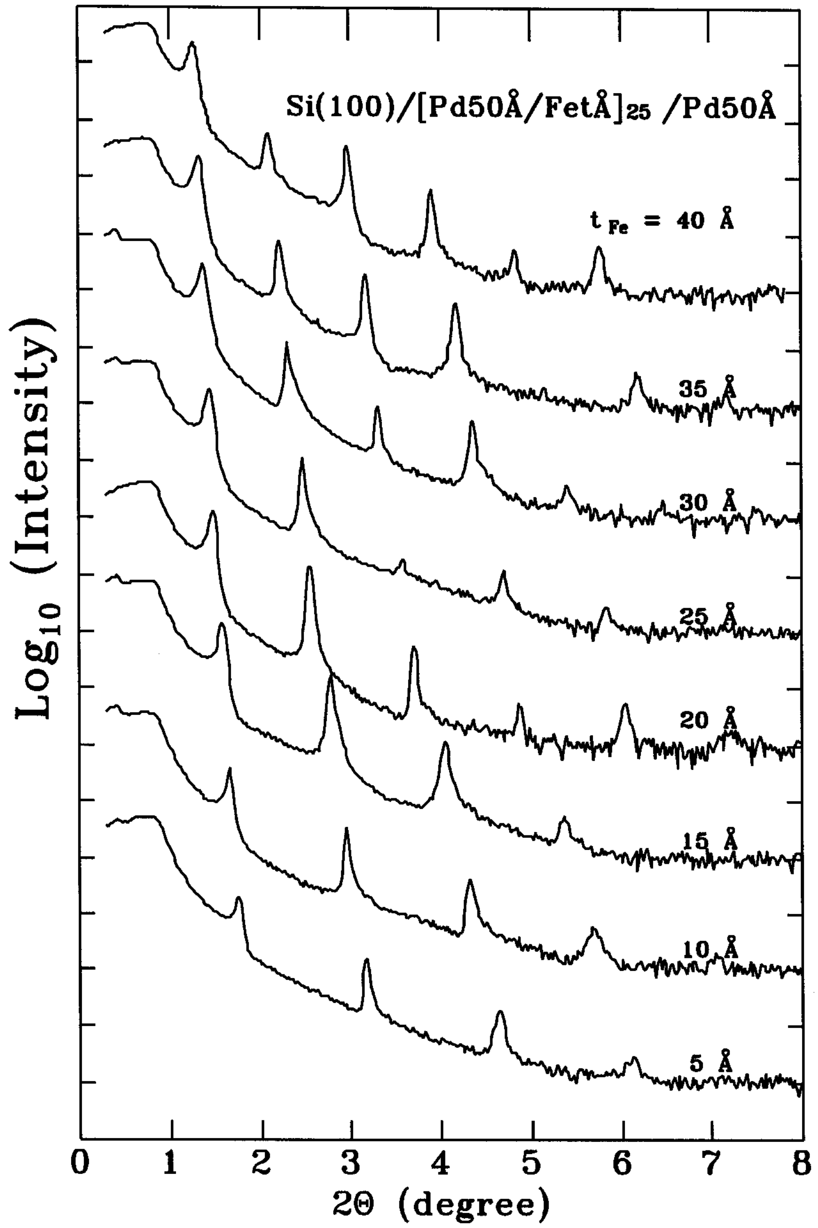

Figure 5.3: Small angle x-ray reflectivity profiles of [Pd 50 Å/Fe t Å]$_{25}$ multilayers, with t_{Fe} = 5 – 40 Å.

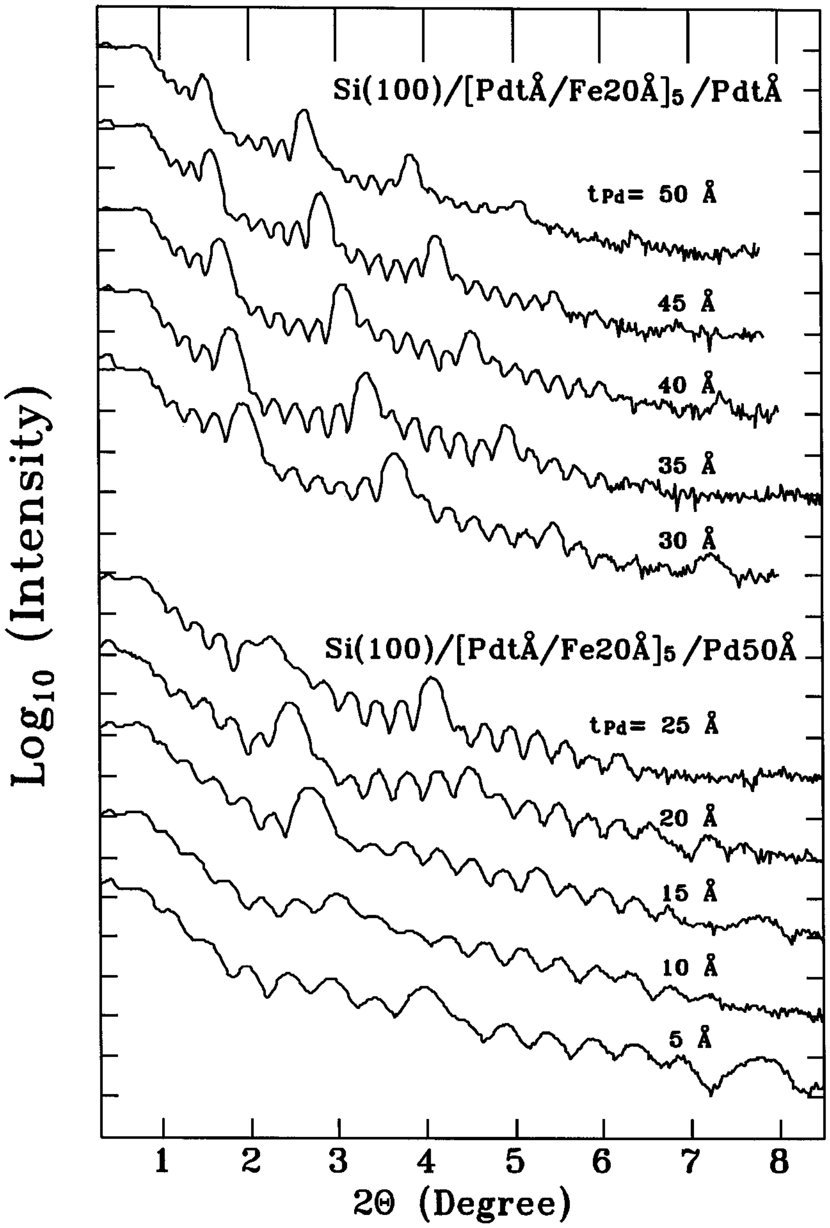

Figure 5.4: Small angle x-ray reflectivity profiles of [Pd t Å/Fe 20 Å]$_5$ multilayers, with t_{Pd} = 5 – 50 Å.

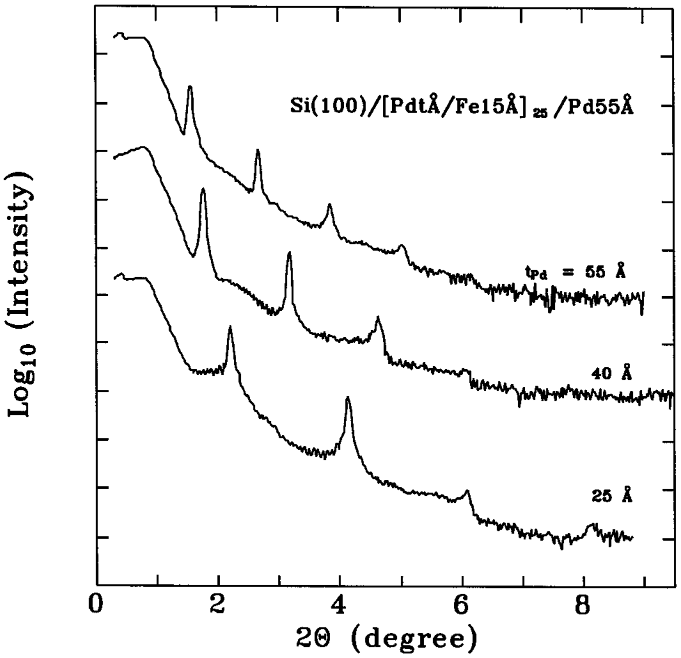

Figure 5.5: Small angle x-ray reflectivity profiles of [Pd t Å/Fe 15 Å]$_{25}$ multilayers, with t$_{\mathrm{Pd}}$ = 10 – 55 Å.

increasing in steps of 4.8 ± 0.2 Å.

The result of such an analysis on the bilayer thickness of [Pd t Å/Fe 20 Å]$_5$ multilayers yields a constant Fe thickness of 18.9 ± 0.2 Å, and a Pd thickness of 5.20 ± 0.05 Å for a nominal t$_{\mathrm{Pd}}$ = 5 Å.

The study of the multilayers for PNR measurements

Two multilayers, nominal [Pd 60Å/Fe 60Å]$_4$ and [Pd 30Å/Fe 30Å]$_5$, were prepared for PNR measurements. Equal thickness of Pd and Fe was chosen to eliminate the scattering at the even-order superlattice reflections. For each sample type, a series of multilayers with slightly varying layer thickness were grown, and the one with a minimum 2nd order superlattice peak was chosen for PNR studies. The reflectivity profiles are shown in Fig. 5.6. The residual weak 2nd order superlattice peak could result from either the Fe and Pd layers not being quite equal to each other, and/or roughness at the two different interfaces, $\sigma_{\mathrm{Pd/Fe}}$ and $\sigma_{\mathrm{Fe/Pd}}$, not being equal. By fitting

Table 5.3: The structural parameters obtained from fitting the small angle x-ray reflectivity profiles of [Pd 50 Å/Fe t Å]$_{25}$ multilayers with t = 5, 10, 15, ... 40 Å. t_{Fe} and t_{Pd} are the Fe and Pd layer thicknesses, $\sigma_{Pd/Fe}$ and $\sigma_{Fe/Pd}$ are the roughnesses at the interface with Pd on top of Fe, and Fe on top of Pd, and Λ is the bilayer thickness.

Nominal [Pd/Fe]$_N$	t_{Fe} (Å)	t_{Pd} (Å)	$\sigma_{Pd/Fe}$ (Å)	$\sigma_{Fe/Pd}$ (Å)	Λ (Å)
[Pd50Å/Fe 5Å]$_{25}$	5.0 ±0.5	53.8 ±0.5	12.0 ±1.4	7.0 ±0.2	58.8 ± 1.0
10	7.5 ±0.4	55.5 ±0.4	12.2 ±1.1	5.8 ±0.1	63.0 ±0.8
15	13.4 ±0.4	54.7 ±0.4	13.0 ±0.9	6.3 ±0.1	68.1 ± 0.8
20	14.4 ±0.4	59.5 ±0.4	9.0 ±0.4	6.5 ±0.1	73.9 ± .8
25	24.8 ±0.2	51.8 ±0.2	7.4 ±0.1	6.8 ±0.1	76.6 ± .4
30	28.4 ±0.3	54.4 ±0.3	8.8 ±0.2	6.1 ±0.1	82.8 ± .6
35	34.5 ±0.7	52.3 ±0.7	10.7 ±0.5	6.2 ±0.1	86.8 ± 1.4
40	41.4 ±0.4	51.5 ±0.4	9.3 ±0.3	6.2 ±0.1	92.9 ± .8

the reflectivity profiles, the actual Fe and Pd thicknesses were obtained, and these two samples were found to have configurations of Pd 61Å/Fe 61Å and Pd 34Å/Fe 34Å respectively.

Small-angle x-ray studies of the Pd/Fe multilayers confirmed the well-defined compositional modulation along the film growth direction. The interfacial roughnesses were found to increase with N from about 5 Å, reaching about 13 Å as N = 20. As shown later, the interface roughness does not give rise to a measurable difference in the saturation magnetisation. The Fe and Pd layer thicknesses were obtained from the analysis of the bilayer thickness as well, which were used to calculate the magnetic moments in the magnetometry studies as presented later.

5.1.2 *High-angle x-ray Diffraction Measurements*

The high angle x-ray diffraction patterns have high intensity peaks around $2\theta = 40.1^\circ$ and 86.7°, which correspond to Pd(111) and Pd(222), suggesting that the Pd/Fe multilayers have a preferential Pd(111) orientation perpendicular to the film plane. Pd(200) and Pd(311) diffraction peaks are also present. The Pd(111) peaks are 15

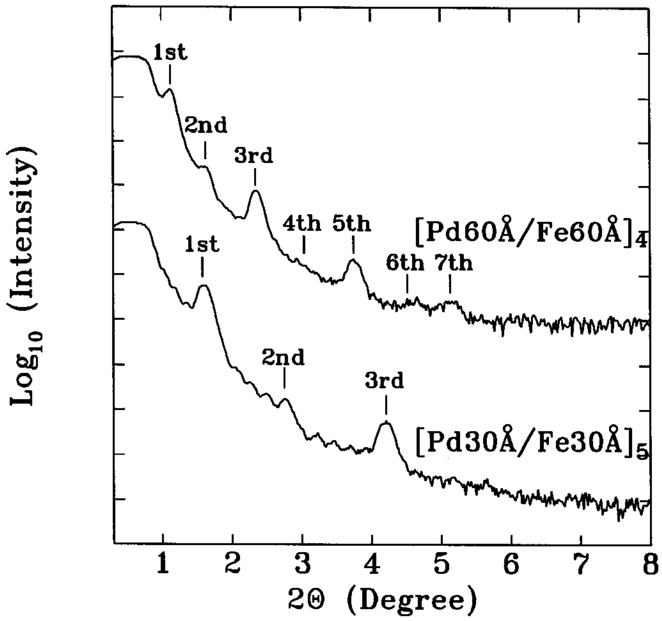

Figure 5.6: Small angle x-ray reflectivity profiles of [Pd 60 Å/Fe 60 Å]$_4$, and [Pd 30 Å/Fe 30 Å]$_5$ multilayers. The weak even order superlattice peaks indicate that the Pd and Fe thicknesses are closely matched.

– 70 times stronger than the Pd(200) and Pd(311) peaks. These are much greater than the ratio between x-ray Bragg intensities from a powdered Pd sample ($I_{(111)}$: $I_{(200)} \approx 2 : 1$, and $I_{(111)} : I_{(311)} \approx 3 : 1$), which suggests predominant Pd(111) texture in our multilayers. The Pd/Fe multilayers with preferential Pd(111)/Fe(110) texture have also been made by deposition using magnetically enhanced dc sputtering guns onto graphite and sapphire substrates[81], and using e-beam deposition on glass and kapton substrates[101].

Using the kinematic diffraction formula[71], the high-angle x-ray diffraction profiles can be fitted using the bulk d-spacings ($d_{Pd(111)} = 2.2465$ Å, $d_{Fe(110)} = 2.0269$ Å). The result is shown in Fig. 5.8. The parameters obtained from the analysis are listed in Table 5.4. The Fe layer thickness increases in a step of 2 AL (except for the last sample), which is not consistent with the value of 2.4 ± 0.1 AL obtained from the analysis of small-angle x-ray data. The problem is that only integer number of atomic layers can be used in fitting the high-angle x-ray data. The comparison of the layer thicknesses obtained from the analysis of small-angle and high-angle x-ray data are

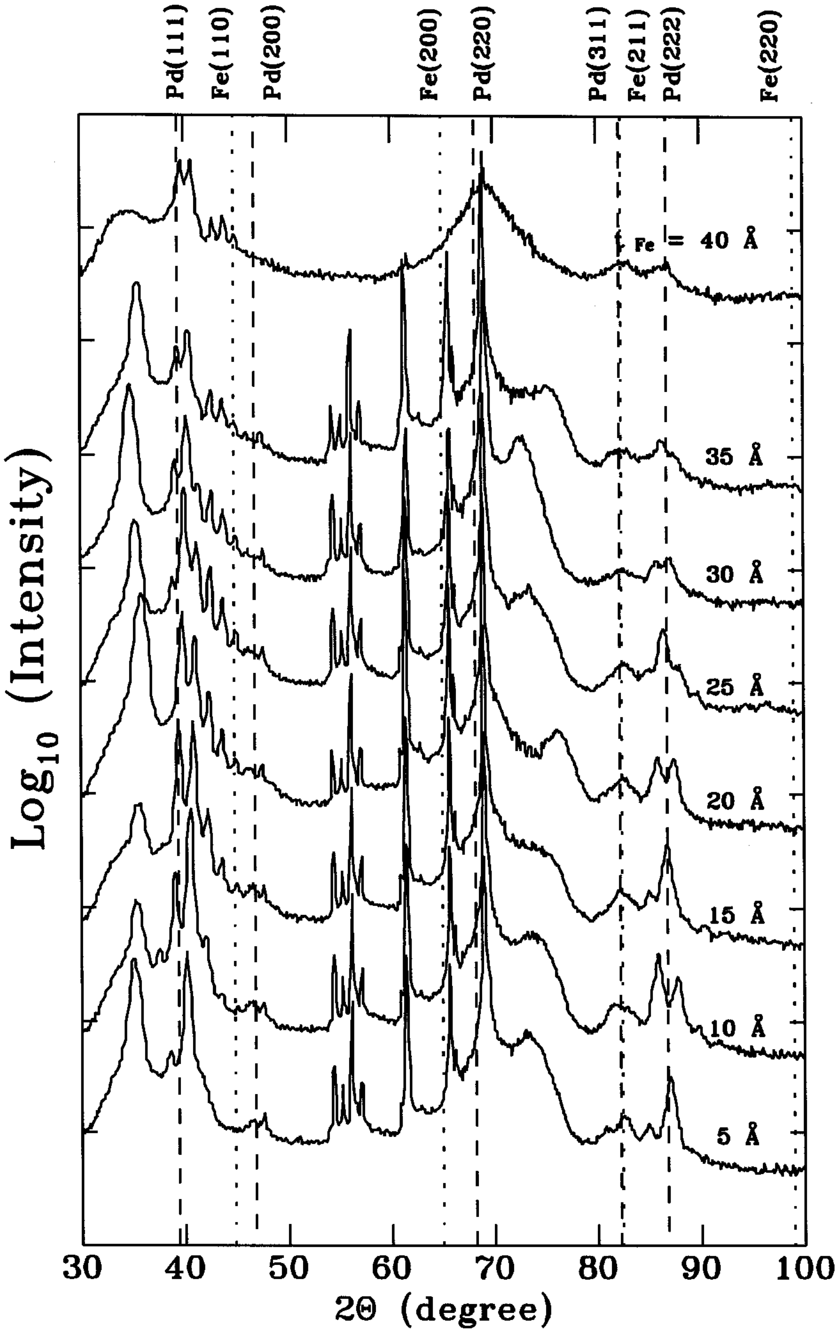

Figure 5.7: High angle x-ray diffraction profiles of [Pd50 Å/Fet Å]$_{25}$, with t = 5 – 40 Å multilayers

shown in Fig. 5.9. More than half of Fe, Pd and bilayer thicknesses obtained from these two analyses are consistent with each other, within error. However, the values from high-angle x-ray data have large uncertainties, suggesting high-angle x-ray data illustrate how the diffraction patterns vary with the layer thicknesses, and but do not provide independent and accurate determination of the layer thicknesses. The Pd and Fe thicknesses were first obtained from small angle x-ray data, then the bulk d-spacings of Pd(111) and Fe(110) were used to convert these layer thicknesses from Å to atomic layers, necessary for the analysis of magnetic data.

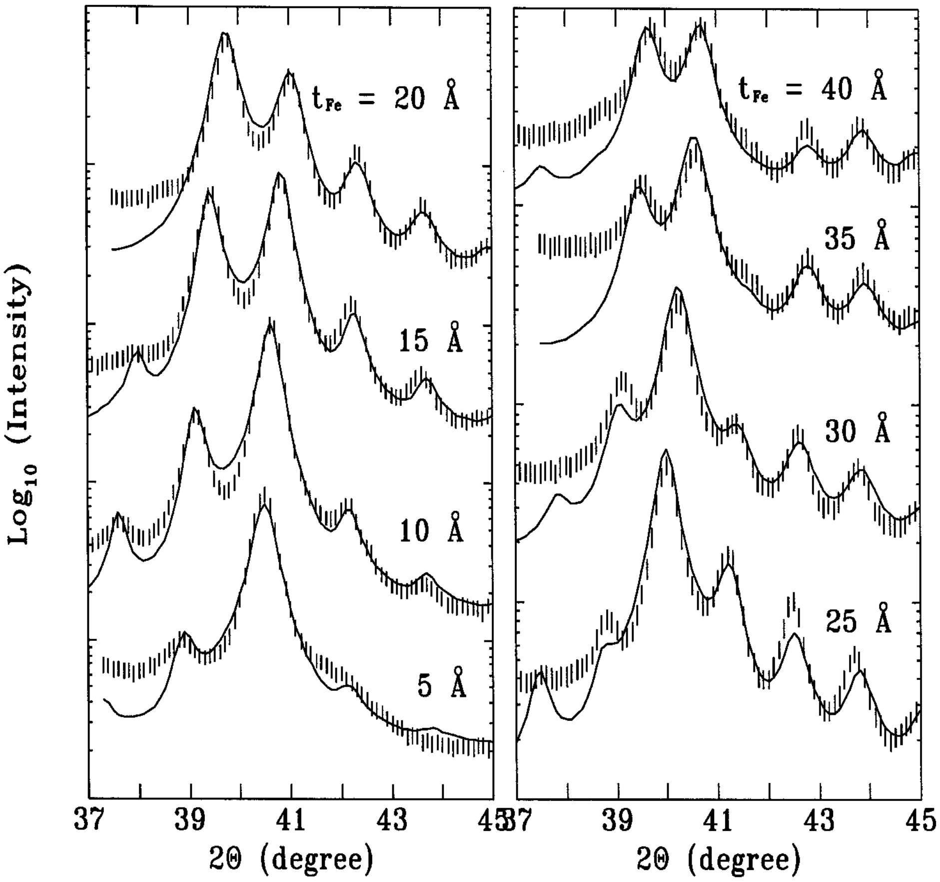

Figure 5.8: Fits to the high angle x-ray diffraction profiles of [Pd50 Å/Fet Å]$_{25}$ multilayers, with t = 5 – 40 Å. The vertical dashed lines are experimental data, and the solid lines are the calculations.

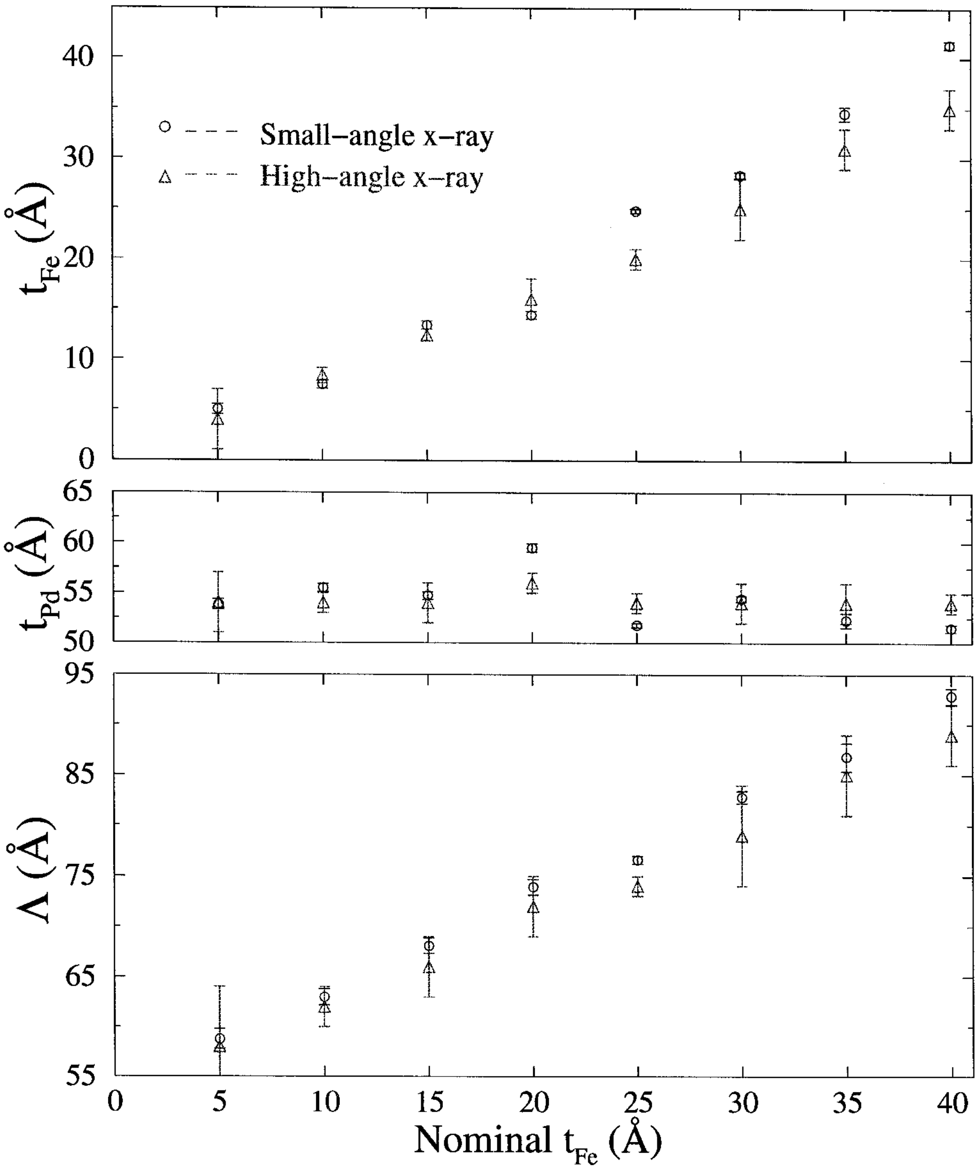

Figure 5.9: The comparison of the Fe (t_{Fe}), Pd (t_{Pd}) and bilayer (Λ) thicknesses obtained from analysis of the small-angle x-ray (○) reflectivity and high-angle x-ray diffraction (△) data of [Pd50 Å/Fet Å]$_{25}$ multilayers with t_{Fe} = 5 – 40 Å.

Table 5.4: The parameters obtained from the analysis of high-angle x-ray diffraction data of multilayers [Pd50Å/Fe t]$_{25}$ with t = 5 – 40 Å. t_{Fe} and t_{Pd} are the layer thicknesses of Fe and Pd in units of Å and atomic layers respectively, and Λ is the bilayer thickness.

Nominal t_{Fe}	t_{Fe} / Atomic Layers	t_{Pd} / Atomic Layers	Λ (Å)
5 Å	4 ± 3 Å / 2 AL	54 ± 3 Å / 24 AL	58 ± 6
10 Å	8.4 ± 0.8 Å / 4 AL	54 ± 1 Å / 24 AL	62 ± 2
15 Å	12.4 ± .6 Å / 6 AL	54 ± 2 Å / 24 AL	66 ± 3
20 Å	16 ± 2 Å / 8 AL	56 ± 1 Å / 25 AL	72 ± 3
25 Å	20 ± 1 Å / 10 AL	54 ± 1 Å / 24 AL	74 ± 1
30 Å	25 ± 3 Å / 12 AL	54 ± 2 Å / 24 AL	79 ± 5
35 Å	31 ± 2 Å / 14 AL	54 ± 2 Å / 24 AL	85 ± 4
40 Å	35 ± 2 Å / 17 AL	54 ± 1 Å / 24 AL	89 ± 3

5.2 *CEMS Study of Pd/Fe multilayers*

The conversion electron Mössbauer spectroscopy (CEMS) spectra of the [Pd50 Å/Fet Å]$_{25}$ multilayers, with t = 5, 10, 15, 20, 30, and 40 Å, denoted by S_5, S_{10}, S_{15}, ..., S_{40} respectively, taken at room temperature (RT) show typical magnetic six-line patterns (Fig. 5.10). The line shape of S_5 is very broad, but no pronounced paramagnetic component is present in the spectrum. For the S_{15}, S_{20} and S_{30} spectra, lines 1 and 2 are slightly sharper and stronger than lines 5 and 6, so two sextets with different hyperfine fields (B_{hf}'s), and isomer shifts (δ) relative to α-Fe, were assumed which when superimposed reproduce the observed asymmetry in the line shape. For S_5, S_{10} and S_{40}, only one sextet was needed because of the symmetric line shape.

The CEMS spectra were fitted using a non-linear least-squares routine. A Gaussian distribution has been assumed for B_{hf}. The hyperfine parameters obtained from the fitting are listed in Table 5.5 and shown in Fig. 5.11. For the spectra fitted with two sextets, one sextet with vanishing isomer shift, δ, and sharper lines (with a field width of $\sim$ 0.8 T) is attributed to a bulk-like Fe site, while the other with a positive δ relative to α-Fe and wider lines (with a field width of $\sim$ 1.5 T) is attributed to an interface-like

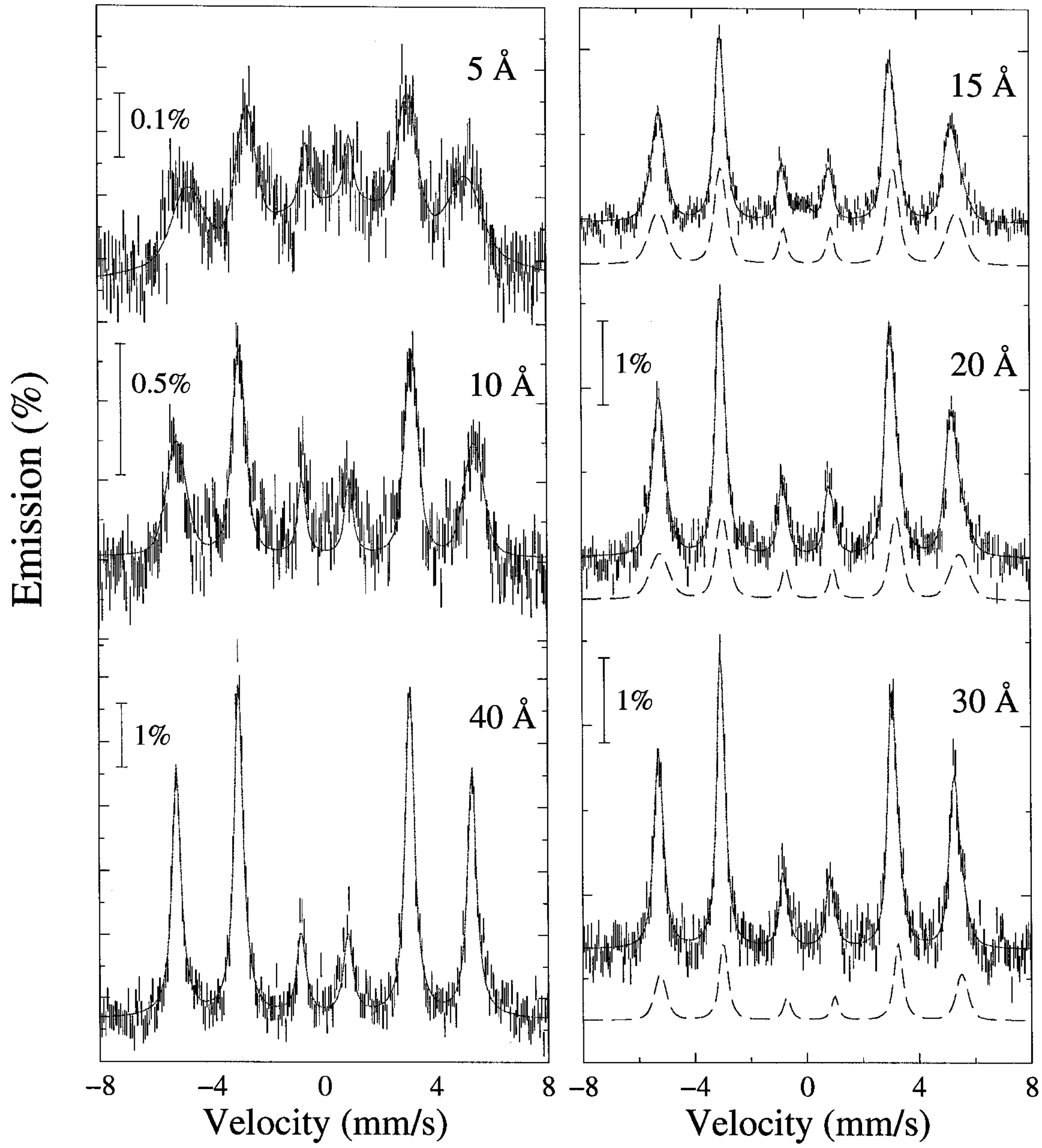

Figure 5.10: The RT-CEMS spectra of [Pd 50 Å/Fe t Å]$_{25}$, t = 5, 10, 15, 20, 30, and 40 Å as labeled in the figures. The black vertical lines are experimental data and the colour lines are fits. The red lines are the overall fits. For the spectra fitted using two sextets, the blue dashed lines, which are displaced verticaly for clarity, are fits for interface-like Fe.

Fe site. The sextets of interface-like Fe, which are depicted by blue dashed lines in Fig. 5.10, have a relative area that decreases with the total Fe thickness (as shown in Fig. 5.11b). If we convert the relative areas of the subspectra to Fe thickness by multiplying the relative area of interface-like Fe by the total Fe thicknesses, the interface-like Fe thickness is found to be constant at 8 ± 1 Å per Fe layer. If the interface-like Fe is distributed equally on each side of an Fe layer, then 4 ± 0.5 Å(or 2.0 ± 0.3 AL) of Fe are interface-like at each Pd/Fe interface. It therefore follows that all of S_5 is interface-like, 80 % of S_{10} is interface-like and 80 % of S_{40} is bulk-like. Since the uncertainty in the interface-like Fe is 10 %, the spectra of S_{10} and S_{40} can not be decomposed into two subspectra. The isomer shift of the interface-like Fe, relative to α-Fe, is in the range of 0.08 – 0.16 mm/s. The quadrupole splitting in all samples is negligible, implying cubic symmetry of the Fe lattice structure. The interface-like hyperfine fields (B^{i}_{hf}) are found to be about 33 T, while the bulk-like hyperfine fields (B^{b}_{hf}) are slightly reduced compared with the accepted value of 33 T for bulk Fe. There is no dramatic change in either δ, or B_{hf} as the Fe thickness is reduced, so our study does not show any evidence for a *bcc* to *fcc* transition as claimed by Li *et al.*[101]. Metastable *fcc* Fe layers can be grown epitaxially on substrates, such as Cu, owing to a match in lattice parameter ($a_{fcc\mathrm{Cu}} = 3.615$ Å and bulk $a_{fcc\mathrm{Fe}} = 3.588$ Å). However, *fcc* Fe can not be stabilized beyond about 13 AL (23 Å)[102, 103, 104]. With the relatively large lattice mismatch between *fcc* Pd ($a_{fcc\mathrm{Pd}} = 3.8908$ Å) and *fcc* Fe, it is very unlikely that *fcc* Fe can be stabilized for any thickness. The Fe in our multilayers is most likely *bcc* in all samples.

For all the multilayers except S_5, the Fe moment is in the sample plane, evidenced by the intensity ratios of 3:4:1:1:4:3 in all the spectra or subspectra. S_5 has a ratio of 3:3.7:1:1:3.7:3, corresponding to a slight (12° ± 7°) out of plane tilt. This strong in-plane anisotropy has been found to persist even in 1 AL of Fe grown on Pd(001), unless the Fe was deposited at low temperatures[105]. For Fe overlayer or Fe layers in multilayer and sandwich structures, with thickness of 1 AL, the perpendicular surface anisotropy usually overcomes the in-plane bulk anisotropy, leading to an out-of-plane

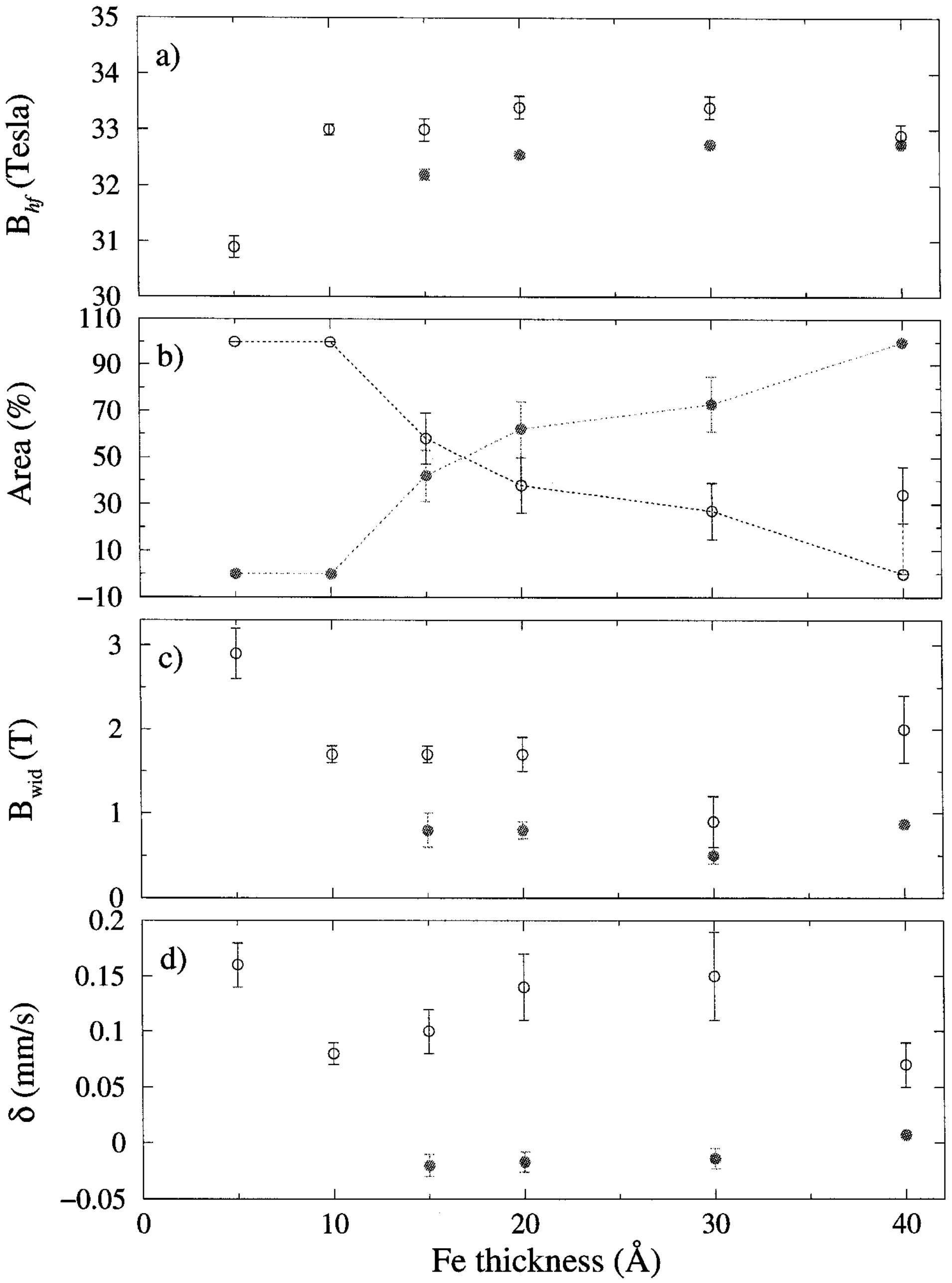

Figure 5.11: The Fe thickness dependence of hyperfine parameters, which are broken down into interface-like (blue ○) and bulk-like (green ●) Fe contributions, for the RT-CEMS spectra of [Pd 50 Å/Fe t Å]$_{25}$, t = 5, 10, 15, 20, 30, and 40 Å. The hyperfine parameters include, a) hyperfine field (B_{hf}), b) percentage area of the subspectra, c) field width (B_{wid}) and d) isomer shift (δ) relative to α-Fe.

Table 5.5: The hyperfine parameters obtained from fitting the room-temperature spectra, assuming one sextet for S_5, S_{10}, and S_{40} and two sextets for S_{15}, S_{20} and S_{30}. The parameters labeled by "b" are for the bulk-like Fe and those labeled by "i" are for the interface-like Fe. The hyperfine parameters include, isomer shift (δ) relative to α-Fe, field width (B_{wid}) of the sextet, hyperfine field (B_{hf}), percentage area (A) of the subspectra.

t_{Fe} (Å)	δ^b (mm/s)	B^b_{wid} (T)	B^b_{hf} (T)	A^b (%)	δ^i (mm/s)	B^i_{wid} (T)	B^i_{hf} (T)	A^i (%)
5	–	–	–	–	.16±.02	2.9±.3	30.9±.2	100
10	–	–	–	–	.08±.01	1.7±.1	33.0±.1	100
15	-.02±.01	.8±.2	32.2±.1	42±11	.10±.02	1.7±.1	33.0±.2	58±11
20	-.017±.009	.8±.1	32.56±.06	62±12	.14±.03	1.7±.2	33.4±.2	38±20
30	-.014±.009	.5±.1	32.74±.06	73±12	.15±.04	0.9±.3	33.4±.2	27±31
40	.007±.003	.87±.04	32.76±.03	100	–	–	–	–

preferential orientation of the magnetisation[106]. The anomalous strong in-plane effective anisotropy in Fe/Pd system was attributed to interfacial alloying during RT depositions[107, 108]. However, the morphology of the interface has long been a controversial issue, and both non-interdiffused[51, 109, 110, 111] and interdiffused[107, 108, 81] interfaces have been reported. In our case, the isomer shift of the interface-like Fe is generally lower than that of Fe atoms in Pd, which is 0.177 ± 0.002 mm/s[112]. Though the possibility of alloy formation can not be totally ruled out, at least the Pd-Fe alloying effect is insignificant in our Pd/Fe multilayers and the interdiffusion between Pd and Fe must be less than 2 AL.

In order to obtain the ground state hyperfine field of interface-like Fe and to study the evolution of B_{hf} with temperature for both interface and bulk-like Fe, CEMS spectra of S_{10} and S_{15} were taken from 90 K to 296 K. Using the RT spectrum as a guide, one-sextet and two-sextets were used to fit the spectra of S_{10} and S_{15} respectively. The hyperfine fields of the interface-like Fe and bulk-like Fe are shown in Fig. 5.12. Since magnetometry and CEMS studies on epitaxial thin films[19, 20] and our sputter-deposited Ag/Fe multilayers (section 4.3) have demonstrated that

B_{hf} measures the temperature dependence of the magnetization of ultrathin Fe films, we assume that B^{i}_{hf} represents the temperature dependence of the magnetization of Fe at the Pd/Fe interface in this system as well. $B^{b}_{hf}(T)$ of S_{15} was fitted using the $T^{3/2}$ spin-wave law[113], yielding a ground state hyperfine field of 34.3 ± 0.2 T and spin stiffness-parameter of $(1.2 \pm 0.1)\times10^{-5}$ $K^{-3/2}$. B^{i}_{hf} of S_{10} and S_{15} were fitted to $B^{i}_{hf}(T) = B^{i}_{hf}(0)\times(1\text{–}bT^{\beta})$, with $\beta = 1.5 \pm 0.4$ for both samples, suggesting the B^{i}_{hf}'s can also be described by the $T^{3/2}$ spin-wave law. The fitting yielded $B^{i}_{hf}(0) =$ 37.8 ± 0.6 T and 36.4 ± 0.4 T for S_{10} and S_{15} respectively. Taking the average of these two values we have $B^{i}_{hf}(0) = 37.1 \pm 0.7$ T, which are enhanced by 9 % relative to the bulk Fe value. If simply fit B^{i}_{hf} to the $T^{3/2}$ spin-wave law, the spin-stiffness parameters are $(2.46 \pm 0.09)\times10^{-5}$ $K^{-3/2}$ and $(1.81 \pm 0.07)\times10^{-5}$ $K^{-3/2}$ for S_{10} and interface-like Fe of S_{15} respectively, which are enhanced relative to the bulk Fe value by 4 – 5 times. The enhanced spin-stiffness parameters are consistent with the size effect predicted by many theoretical studies on the spin excitations in quasi-two-dimensional systems[114, 115, 116, 117]. These studies show that the spin-stiffness parameter increases with decreasing film thickness, as a consequence of the loss of exchange interaction across surface[118], and/or the weakening surface exchange[119].

An important but problematic issue is the relationship between B_{hf} and the local moment. In the bulk, the major contribution to B_{hf} is the negative polarisation field (B_{cp}) of the core electrons due to the *d* electrons via the Fermi contact interaction. B_{cp} is approximately proportional to the magnetization, so is B_{hf}, which is the basis of the empirical interpretation of B_{hf}. Using this empirical interpretation, the interface hyperfine field of 37.1 ± 0.7 translates into the interface Fe moment of 2.42 ± 0.05. However, at a surface or interface, the contributions from the conduction electrons (B_{ce}) and the dipolar field (B_{dip}), which are strongly dependent on the local environment, might become prominent[6, 17, 18, 93]. As a result, B_{hf} might not scale with the magnetization the same way as in the bulk. A detailed calculation of the electronic structure and B^{i}_{hf} is necessary to evaluate the Fe moment at the Pd/Fe interface. As this type of calculation is not available, we can only present

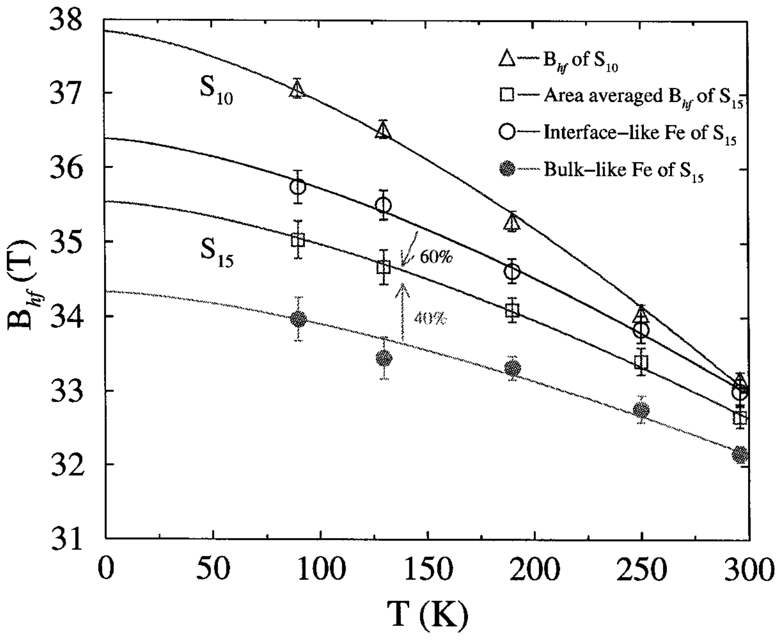

Figure 5.12: The temperature dependence of the hyperfine fields of S_{10} (red △), and S_{15}: interface-like (blue ○) and bulk-like (green ●) Fe contributions and area averaged hyperfine field (red □). The solid lines are for the fits using $T^{3/2}$.

qualitative arguments. According to calculations for Fe at a clean surface[6], and interfaces of Fe/Ag(001)[17] and Fe/W(110)[18], B_{cp} scales approximately with the moment regardless of the local environment with a scaling factor of ~ -13 to -14 T per unpaired spin. Assuming the same scaling factor at the Pd/Fe interface, a $2.7 \pm 0.2\ \mu_B$ moment could give rise to a B_{cp} of -37.1 ± 0.7 T, which is the $B^i_{hf}(0)$'s obtained in our study.

From another point of view, if the average magnetization of Fe has the same temperature dependence as the average hyperfine field, the interface Fe moment (μ_i) must scale with $B^i_{hf}(0)$ the same way as the bulk-like Fe moment does with $B^b_{hf}(0)$. However, the spin-stiffness parameter of the average magnetization is not sensitive to the change in μ_i. For example, using a straight forward calculation, for S_{15}, 1 μ_B difference in μ_i only brings about a 4 % difference in the spin-stiffness parameter. Different scaling factors between μ and B_{hf}'s for the interface and bulk-like Fe do not affect the same temperature dependence of the average magnetization and the hyperfine field.

There have been Mössbauer spectroscopy studies on Pd/Fe systems. Depth-profiling Mössbauer spectroscopy by Hosoito *et al.*[109] showed that about 30 % of the Fe in 3.5 Å probe layers at the Pd interface was paramagnetic at RT and exhibited a reduced hyperfine field of 31.5 T at 4.2 K as compared to the bulk Fe value of 34 T, while the rest of the Fe had an enhanced hyperfine field of 36.5 T at 4.2 K. In the RT-CEMS studies by Boufelfel *et al.*[81] and Li *et al.*[101], no paramagnetic component was observed, and the hyperfine field of the interface-like Fe was larger than bulk Fe. Our RT spectra have no paramagnetic components, in agreement with Boufelfel *et al.*[81] and Li *et al.*[101], but in conflict with Hosoito *et al.*[109]. We do not observe a *bcc* to *fcc* transition as the Fe thickness was reduced as claimed by Li *et al.*[101].

In summary, microscopic data of Fe in the Pd/Fe multilayers obtained by CEMS study were presented in this section. Two Fe contributions were identified: one from the bulk, the other associated with the Pd/Fe interface. The total interfacial Fe thickness was 8 ± 1 Å per Fe layer. Assuming that the interfacial Fe is distributed equally on each side of the Fe layer, then each Pd/Fe interface has an interface-like Fe thickness of 4 Å (or 2.0 ± 0.3 atomic layers). The temperature dependence of the hyperfine fields of two samples was measured between 90 – 295 K, which reflected the variation of the Fe magnetisation with temperature. Extrapolating the hyperfine field to 0 K yields a ground state hyperfine field of 37.1 ± 0.7 T, which is enhanced relative to the bulk Fe value of 34 T. If we assume a simple linear scaling between the hyperfine field and the magnetic moment, then the hyperfine field translates into an enhanced Fe moment of 2.42 ± 0.05 μ_B at the Pd/Fe interfaces. If we use the scaling factor from theoretical calculations[6, 18], the hyperfine field corresponds to 2.7 ± 0.2 μ_B. The 2.42 ± 0.05 μ_B was confirmed by the PNR study presented in section 5.4.

5.3 *Magnetometry Measurements*

5.3.1 *Fe and Pd Moments*

The saturation magnetization of a Pd/Fe multilayer, obtained by magnetometry measurements, gives the total contributions from Fe and Pd. In order to separate the Fe contribution from the total magnetization, a series of multilayers [Pd 50 Å/Fe t Å]$_{25}$ with fixed Pd thickness and varying Fe thickness, $t_{\mathrm{Fe}} = 5 - 40$ Å were investigated. Assuming that the magnitude and extent of the polarisation of Pd are not significantly dependent on the thickness of Fe, fixing the Pd thickness fixes the Pd contribution. The variation in the total magnetization with Fe thickness is then due solely to the increase in contribution from Fe.

The saturation magnetizations of multilayers [Pd 50 Å/Fe t Å]$_{25}$ with $t = 5 - 40$ Å, were measured at 5 K and up to 2 Tesla, then averaged over the number of Fe atoms, giving the average moment of the multilayer per Fe atom, $\overline{\mu}_{\mathrm{Fe}}$. The number of Fe atoms in each sample was calculated using the sample area, Fe thickness and bulk Fe density. Fig. 5.13 shows a plot of $\overline{\mu}_{\mathrm{Fe}}$ against t_{Fe}. As mentioned on page 81, the actual $t_{\mathrm{Fe}} = 4.8 - 38.7$ Å (or $t_{\mathrm{Fe}} = 2.4 - 19.1$ AL). $\overline{\mu}_{\mathrm{Fe}}$ is as large as 3.65 μ_{B} per Fe for the sample with 2.4 AL Fe, and decreases with t_{Fe}, reaching 2.5 μ_{B} for the sample with 19.1 AL Fe. This *apparent* enhancement in $\overline{\mu}_{\mathrm{Fe}}$ relative to the bulk Fe value of 2.2 μ_{B} is interpreted as a result of (a) enhanced interface-like Fe moment, and (b) contribution from Pd polarisation.

For a clearer understanding of the variation of the total magnetization with t_{Fe}, the total magnetization (M_{tot}) of a multilayer is written in terms of $\overline{\mu}_{\mathrm{Fe}} \cdot t_{\mathrm{Fe}}$ and is shown as a function of t_{Fe} in Fig. 5.14. The data lie on a straight line (except for the sample with the thinnest Fe layer, which falls just below the line). This implies that to a good approximation, the Pd polarisation (M_{Pd}), bulk (μ_{b}) and interfacial (μ_{i}) Fe moments are independent of t_{Fe}. The magnetic profile of the Pd/Fe multilayers can be described in the following way. The Pd polarisation has a constant contribution of $M'_{\mathrm{Pd}} = M_{\mathrm{Pd}} \cdot \frac{\sigma_{\mathrm{Pd}}}{\sigma_{\mathrm{Fe}}}$, to M_{tot}, where σ_{Pd} and σ_{Fe} are the in-plane densities of Pd and Fe respectively (for bulk Fe(110), $\sigma_{\mathrm{Fe}} = 0.1721$ atoms per Å^2; and for bulk Pd(111),

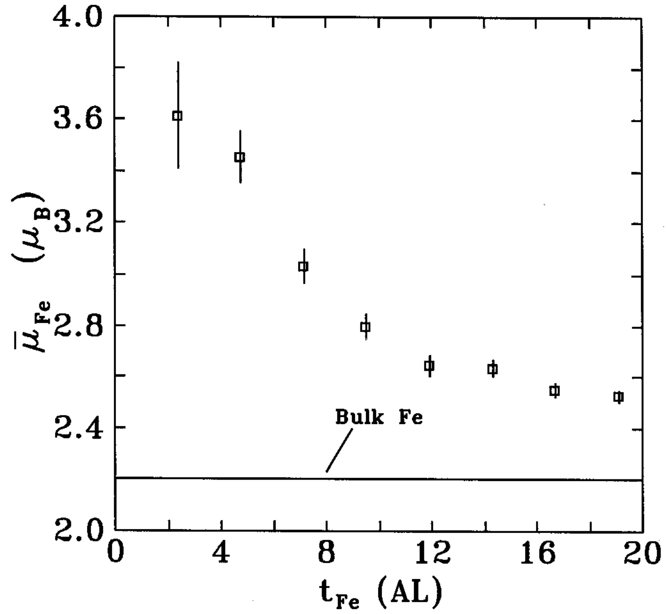

Figure 5.13: The moment per Fe ($\overline{\mu}_{Fe}$) as a function of Fe thickness t for multilayers [Pd24 AL/Fe t]$_{25}$ with t = 2.4 - 19.1 AL. The $\overline{\mu}_{Fe}$'s are enhanced relative to bulk Fe value.

σ_{Pd} = 0.1526 atoms per Å^2). If the Fe layer is thinner than 2t$_\mathrm{i}$, where t$_\mathrm{i}$ is the maximum interfacial Fe thickness on each side of Fe, all Fe atoms are interface-like, and M$_{\mathrm{tot}}$ increases with t$_{\mathrm{Fe}}$ proportionally at a rate of μ_i. This can be expressed by the following equation

$$\mathrm{M_{tot}} = \mu_\mathrm{i} \times \mathrm{t_{Fe}} + \mathrm{M'_{Pd}}, \qquad \mathrm{t_{Fe}} \leq 2\mathrm{t_i}. \tag{5.2}$$

As t$_{\mathrm{Fe}}$ exceeds 2t$_\mathrm{i}$, the interface-like Fe stops growing while the bulk-like Fe emerges. The M$_{\mathrm{tot}}$ can be expressed as,

$$\mathrm{M_{tot}} = \mu_\mathrm{i} \times 2\mathrm{t_i} + \mu_\mathrm{b} \times (\mathrm{t_{Fe}} - 2\mathrm{t_i}) + \mathrm{M'_{Pd}}, \qquad \mathrm{t_{Fe}} > 2\mathrm{t_i}. \tag{5.3}$$

According to Eqns. (5.2) and (5.3), ideally, two straight lines should be seen in Fig. 5.14 of M$_{\mathrm{tot}}$ vs. t$_{\mathrm{Fe}}$. One, the blue dashed line in the figure, has a slope of μ_i and an intercept of M$'_{\mathrm{Pd}}$ for the data with t$_{\mathrm{Fe}}$ < 2t$_\mathrm{i}$; the other, the green solid line in the figure, has a slope of μ_b and an intercept of M$'_{\mathrm{Pd}}$+ ($\mu_\mathrm{i} - \mu_\mathrm{b}$) × 2t$_\mathrm{i}$, for the data with t$_{\mathrm{Fe}}$ > 2t$_\mathrm{i}$. From Fig. 5.14, it is clear that 2t$_\mathrm{i}$ is less than 4.8 AL which is consistent with the CEMS study. The blue dashed line is not from a fitting using Eqn. 5.2,

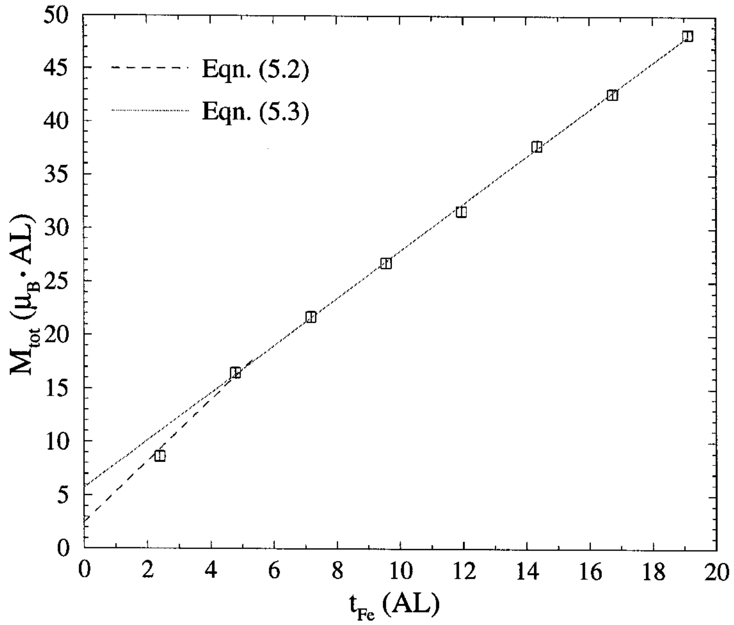

Figure 5.14: M_{tot} vs. Fe thickness t_{Fe} for multilayers [Pd 24 AL/Fe t]$_{25}$ with t = 2.4 - 19.1 AL. The blue dashed line is the illustration of Eqn. (5.2), while the green solid line is the fit using Eqn. (5.3).

but an illustration since there is only one data point below 4.8 AL. Moreover, the Fe layers with thickness less than 7 Å(3.5 AL) break into an island structure[120], and the values of μ_i and M'_{Pd} can not be determined from samples with $t_{Fe} \leq 4.8$ AL. Upon fitting a straight line to the data with $t_{Fe} \geq 4.8$ AL, a slope of 2.22 ± 0.03 μ_B, and an intercept of 5.7 ± 0.4 μ_B·AL are obtained. It follows that $\mu_b = 2.22 \pm 0.03$ μ_B, which is consistent with the value of bulk Fe. Also $M'_{Pd} + (\mu_i - \mu_b) \cdot 2t_i = 5.7 \pm 0.4$ μ_B·AL. Taking $\mu_i = 2.42 \pm 0.05$ μ_B/Fe and $t_i = 2.0 \pm 0.3$ AL from our CEMS data, we find that the interfacial Fe contribution to this intercept is ~0.8 ± 0.3 μ_B·AL, less than 15 % of the total, implying that there must be significant polarisation of the Pd atoms.

In order to investigate how the Pd moment is distributed across a Pd layer, a series of multilayers, [Pd t /Fe 20 Å]$_5$, with nominal $t_{Pd} = 5 - 50$ Å were studied. From our small-angle x-ray study, the actual $t_{Fe} = 18.9 \pm 0.2$ Å, and the nominal 5 Å of Pd has an actual thickness 5.20 ± 0.05 Å. In units of AL, this series of multilayers can be denoted by [Pd t AL/Fe 9.4 AL]$_5$ in which t = 2.3 – 23.1 AL.

As shown in Fig. 5.15, $\overline{\mu}_{\mathrm{Fe}}$ is essentially a constant of 3.0 μ_{B} within error. The 6% uncertainty of each datum comes from magnetometry measurement (3%) and sample area measurement (3%), which are random errors. However, the plot of $\overline{\mu}_{\mathrm{Fe}}$ against t_{Pd} shows an interesting systematic variation: $\overline{\mu}_{\mathrm{Fe}}$ first increases with t_{Pd}, reaching a maximum at $\mathrm{t}_{\mathrm{Pd}} = 11.6$ AL, then decreases with t_{Pd}, reaching a minimum at $\mathrm{t}_{\mathrm{Pd}} = 18.5$ AL. The difference between the maxima and minima is about 9% of the average $\overline{\mu}_{\mathrm{Fe}}$ of 3.0 μ_{B}. The question is whether this variation of $\overline{\mu}_{\mathrm{Fe}}$ with t_{Pd} is an intrinsic property or an experimental artifact. The number of Fe atoms is calculated using the Fe thickness obtained from the analysis of small-angle x-ray reflectivity data. The samples were prepared in sequence starting from the sample with the largest t_{Pd} to the sample with smallest t_{Pd}, so there might be a small systematic variation in the Fe layer thickness. We can not categorically rule out the possibility that there is an intrinsic oscillation in $\overline{\mu}_{\mathrm{Fe}}$ as a function of t_{Pd}, but as these oscillations in $\overline{\mu}_{\mathrm{Fe}}$ are within the errors of the experimental measurements, for the rest of the analysis we will assume that $\overline{\mu}_{\mathrm{Fe}}$ is independent of t_{Pd}.

A few groups have also studied the polarisation of Pd by means of magnetic measurements on samples with fixed Fe thickness while varying the Pd thickness. Childress *et al.*[53] measured the saturation magnetization at 15 K of MBE synthesized Fe/Pd(001) superlattices, in which $\mathrm{t}_{\mathrm{Fe}} = 18$ Å, $\mathrm{t}_{\mathrm{Pd}} = 12 - 26$ Å. They found that the saturation magnetization was essentially independent of t_{Pd}, and $\overline{\mu}_{\mathrm{Fe}}$ was 23 % enhanced with respect to the bulk Fe value, corresponding to a total magnetization enhancement of 6.6 ± 3.2 μ_{B}·AL.

In the study of Li *et al.*[101], at 5 K, $\overline{\mu}_{\mathrm{Fe}}$ of the electron-beam evaporated [Fe 20 Å/Pd t Å]$_{25}$, t = (6 – 60 Å) multilayers, which have strong Pd(111)/Fe(110) texture, shows an interesting oscillatory behavior as t_{Pd} increases, and was enhanced by ∼ 35 % at the maxima. They explained the oscillation in $\overline{\mu}_{\mathrm{Fe}}$ by assuming that the Pd atoms at the interface were directly polarised by Fe atoms through 3*d*-4*d* hybridization, while the Pd atoms not in proximity with Fe were polarised by indirect Ruderman-Kittel-Kasuya-Yosida (RKKY) interaction, which oscillates between ferromagnetic

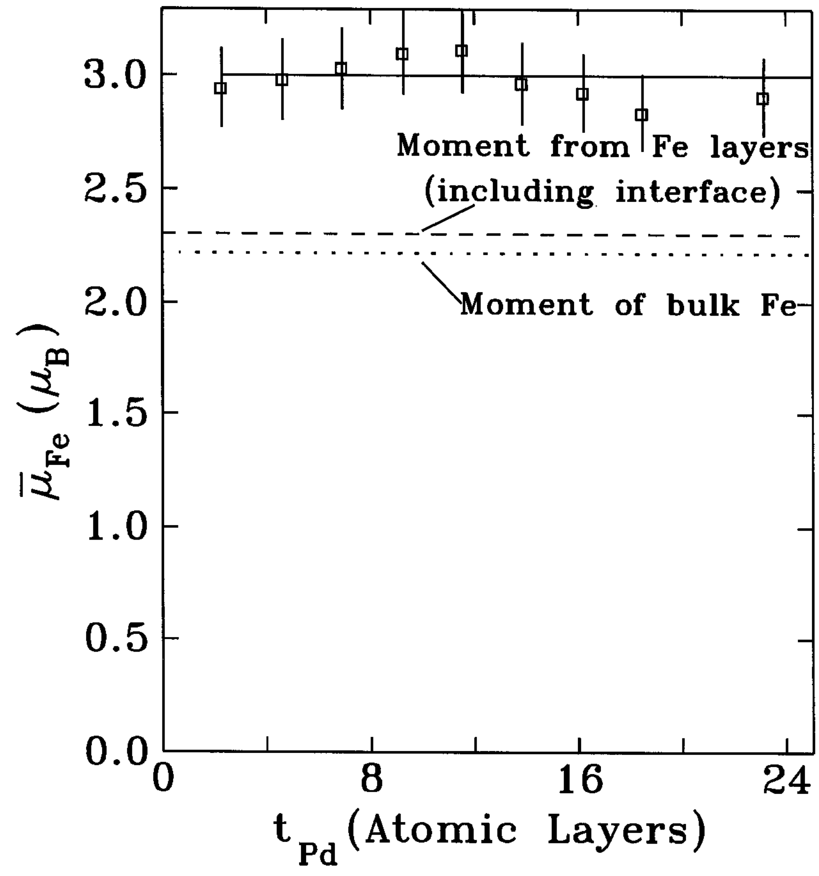

Figure 5.15: The plot of saturation magnetization at 5 K averaged on Fe layers $\overline{\mu}_{\mathrm{Fe}}$ (□) against Pd thickness (t_{Pd}) for [Pd t/Fe 9.4 AL$]_5$ multilayers with t = 2.3 - 23.1 AL. The dotted line represents the moment of bulk like Fe. The dashed line represents the average moment of 9.4 AL Fe. The solid line is for the average value of $\overline{\mu}_{\mathrm{Fe}}$.

and antiferromagnetic coupling and changes the direction of Pd moment relative to that of the Fe moment from positive to negative at various distances from the Fe/Pd interface. However, their explanation is questionable. Firstly, the strength of the RKKY interaction decays rapidly with distance from the interface[121, 122]. The negative Pd polarisation in the inner Pd layer is not large enough to cancel the positive Pd polarisation, carried by Pd atoms close to the interface, and account for their observed oscillatory $\overline{\mu}_{\mathrm{Fe}}$. Secondly, according to the calculation by Shi *et al.*[123], the coupling between the Fe layers across the Pd spacer is predominantly ferromagnetic. Turning to Li's[101] small-angle x-ray reflectivity data, one can see that the variation of the bilayer thickness of the samples does not follow their nominal thickness. The oscillatory behavior of $\overline{\mu}_{\mathrm{Fe}}$ is likely due to variations in the Fe thickness. Wang *et al.*[124] also observed oscillatory $\overline{\mu}_{\mathrm{Fe}}$ at room temperature in their magnetron-sputtered multilayers. However, the oscillation period from Wang's[124] study is quite different from that from Li's[101] study. Moreover, Wang's[124] measurements were done at room temperature, where $\overline{\mu}_{\mathrm{Fe}}$ is affected by the spin excitations, so that they do not necessarily reflect the ground state values.

The results of our study of Pd/Fe multilayers with constant Fe thickness and varying Pd thickness show a constant $\overline{\mu}_{\mathrm{Fe}}$ for multilayers with $t_{\mathrm{Pd}} \geq 2.3$ AL, and are qualitatively consistent with Childress *et al.*[53]. Our results certainly do not agree with the oscillatory $\overline{\mu}_{\mathrm{Fe}}$ as a function of Pd thickness, observed by Li *et al.*[101] and Wang *et al.*[124]. The oscillatory $\overline{\mu}_{\mathrm{Fe}}$ as a function of Pd thickness is not necessarily an intrinsic property of Pd/Fe system, but an experimental artifact.

5.3.2 *The Temperature Dependence of the Magnetization*

The magnetisation measurements were made at different temperatures between 5 – 290 K in fields of up to 3 Tesla. The saturation magnetisation was obtained by extrapolating the high field data to zero field in order to remove the demagnetizing signal from Si substrate and sample holder. The magnetization and hyperfine field (B_{hf}) normalized by their ground state values are shown as a function of temperature in Fig. 5.16. The saturation magnetisation drops twice as fast as B_{hf} with temperature. Since the magnetization of Fe follows the same temperature dependence as that of the hyperfine field, the temperature dependence of Pd must decrease faster with temperature than the total magnetization. This directly leads to the conclusion that: 1) Pd is significantly polarised at low temperature; 2) the Pd polarisation is strongly temperature dependent.

Using the temperature dependence of the hyperfine fields we can extend the CEMS data below 90 K (the total extrapolated change over this region is less than 3%). Furthermore, using the interfacial Fe moment and thickness obtained from the CEMS measurement, which are introduced in section 5.2, the contributions of the bulk and

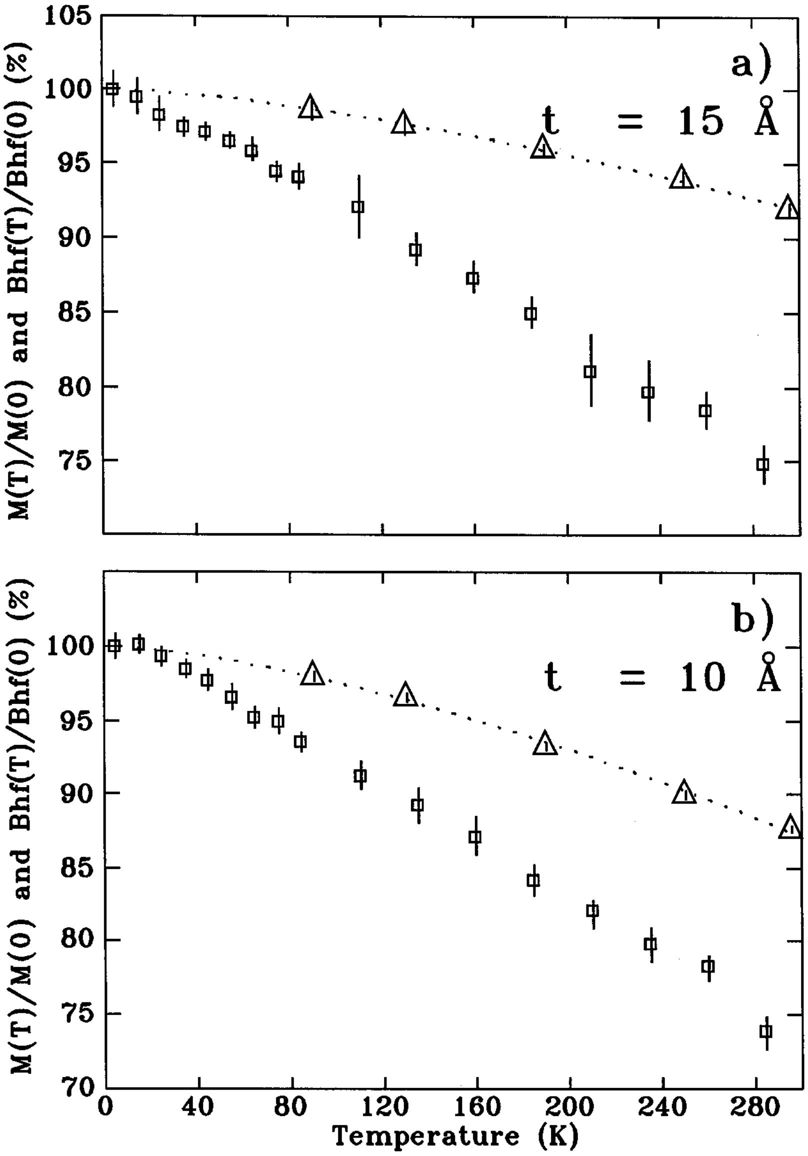

Figure 5.16: The normalized temperature dependence of hyperfine field (△) and saturation magnetisation (□) for a) [Pd 50 Å/Fe 15 Å]$_{25}$, and b) [Pd 50 Å/Fe 10 Å]$_{25}$. Dotted lines through hyperfine field is $T^{3/2}$ fits.

interfacial Fe to the total magnetisation can be obtained. Subtraction from the measured total then yields an estimate of the temperature dependent Pd polarisation (Fig. 5.17). The dotted lines indicate the limits of uncertainty in M_{Fe} and M'_{Pd} arising from uncertainties in the thickness of the interfacial Fe component and its moment. M'_{Pd} approximately follows a linear temperature dependence. There is almost no Pd polarisation surviving at room temperature.

5.3.3 *Magnetic Coupling and Magnetic Reversal*

The phenomenon of the oscillatory nature of the magnetic coupling between two ferromagnetic thin films separated by a layer of non-magnetic transition metal as a function of the non-magnetic spacer thickness has long been a subject of intensive study[121, 122]. The magnetic coupling between Fe layers through a Pd layer has been studied in an MBE-grown Fe/Pd(001) system. Using ferromagnetic resonance and Brillouin light scattering, Celinski *et al.*[125] found the exchange coupling in the Fe/Pd/Fe/Ag(001) trilayer structures remained ferromagnetic (FM) up to 12 AL with a distinct oscillatory behavior (with a period of 4 AL) superimposed on a decreasing background. Between 13 – 18 AL, the coupling changed to a weak anti-ferromagnetic (AF) coupling. By contrast, from the magnetisation and Kerr imaging studies of Fe/Pd/Fe/MgO(100) trilayer structures, Childress *et al.*[53] found that the coupling was FM for a wide range of Pd thickness(5 – 25 AL). Hicken *et al.*[126] studied the trilayer structures, which were grown under conditions similar to those of Childress *et al.*. Using BLS and polar magneto-optic Kerr effect, they also found FM exchange coupling in all the samples they studied, the Pd thickness lying between 14 – 30 Å(7.2 – 15.4 AL).

In order to resolve these contradictions, we examined magnetic coupling in our Pd/Fe multilayers by measuring the magnetic hysteresis loops of [Pd t Å/Fe 15 Å]$_{25}$ multilayers, with t_{Pd} = 10 – 55 Å, between 5 – 290 K. Fig. 5.18 shows the hysteresis loops of three multilayers with t_{Pd} = 25, 40 and 55 Å, namely S_{25}, S_{40} and S_{55} respectively. The hysteresis loops of multilayers with t_{Pd} = 10 – 30 Å resemble those of S_{25}, and are characterized by a small coercive field of less than 0.5 mT,

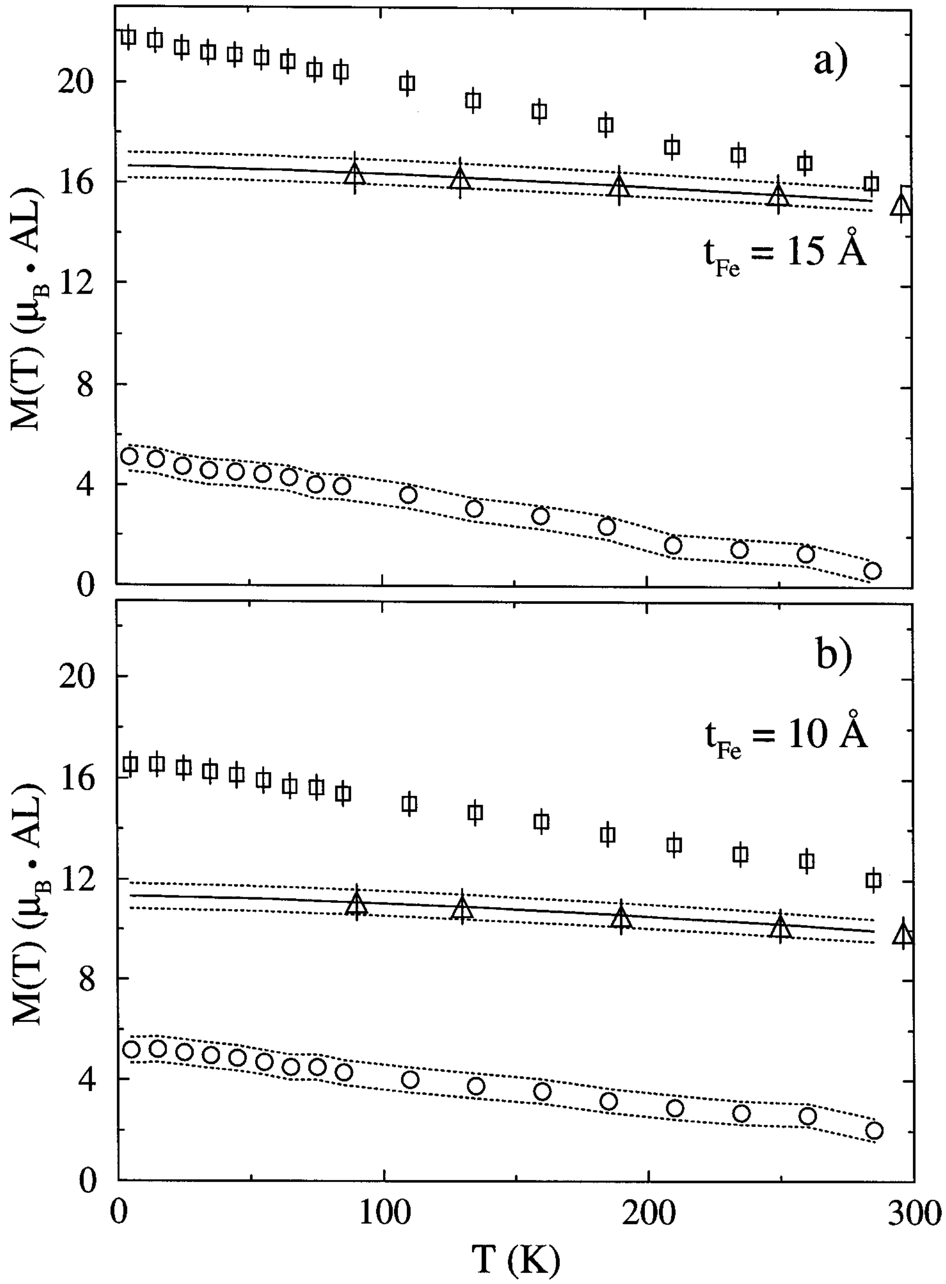

Figure 5.17: The temperature dependence of the palladium polarisation M'_{Pd} (○) obtained by subtracting M_{Fe} (△ – derived from CEMS data) from M_{tot} (□) for a) [Pd 50 Å/Fe 15 Å]$_{25}$, and b) [Pd 50 Å/Fe 10 Å]$_{25}$ (see text). Dotted lines indicated the range of uncertainty in M_{Fe} and M'_{Pd} arising from uncertainties in the thickness of the interfacial Fe component and its moment. Solid line through CEMS data is $T^{3/2}$ fit used to extend the data down to 5 K.

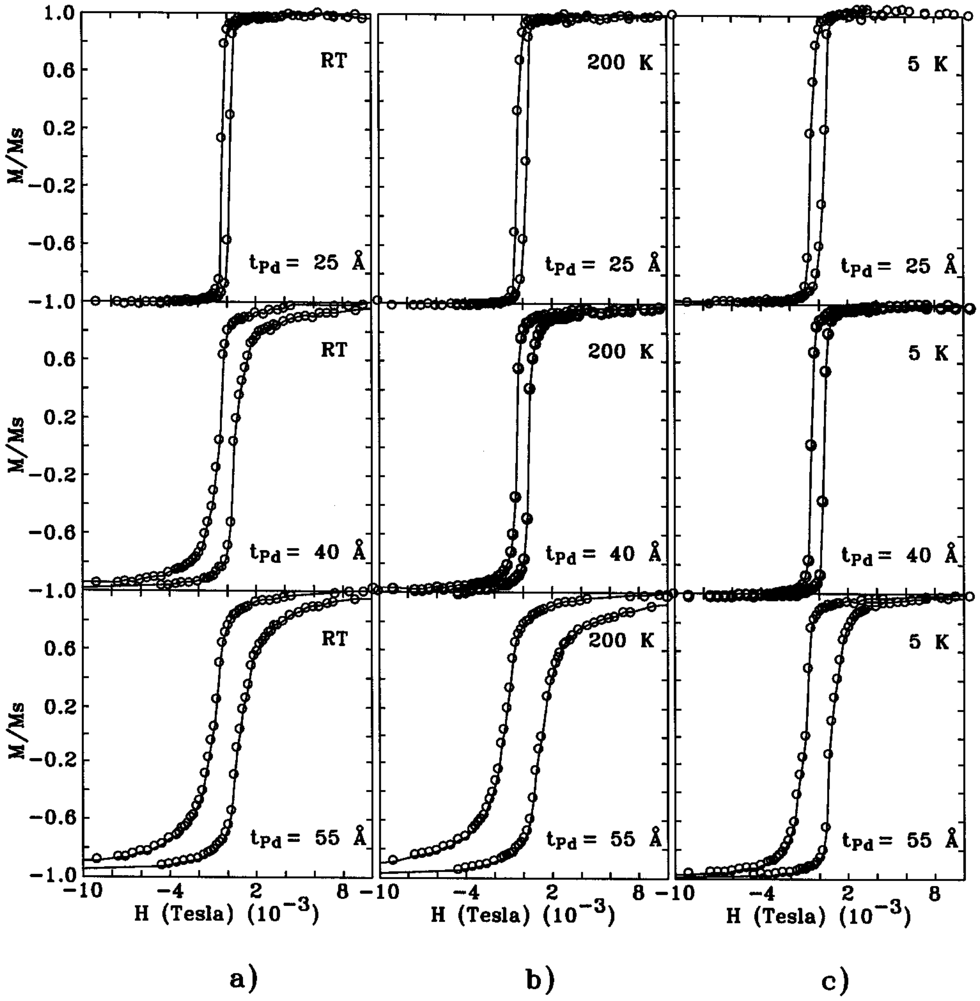

Figure 5.18: The hysteresis loops for [Pd tÅ/Fe 15Å]$_{25}$ with t = 25, 40 and 55 Å, measured at a) RT, b) 200 K and c) 5 K.

with an abrupt reversal of the magnetisation, indicating that the coupling is FM. However, an interesting "wasp-waisted" shape feature was observed for the hysteresis loops of S_{40} and S_{55}. The "wasp-waisted" shape feature is generally associated with either AF coupling[121, 122], or incoherent reversals of magnetic layers with different coercivities[127]. However, the "wasp-waisted" shape feature disappeared for the multilayers with small number of bilayer period (N), ruling out the possibility of AF coupling in our Pd/Fe multilayers.

The multilayers used to study the N dependence of the hysteresis loop are denoted by [Pd 50Å/Fe 20Å]$_N$, where N = 5, 10, 15, and 20. The hysteresis loops measured at

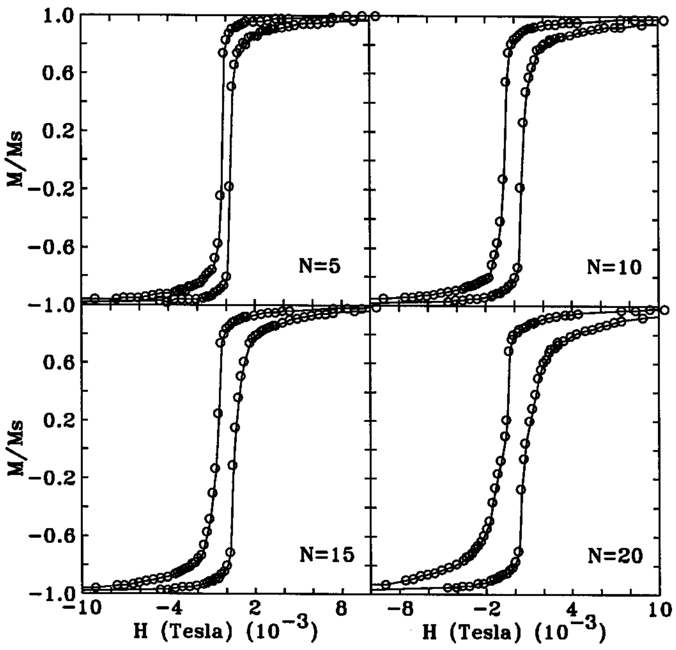

Figure 5.19: The RT hysteresis loops for [Pd 50Å/Fe 20Å]$_N$ with N = 5, 10, 15, and 20.

RT are shown in Fig. 5.19. The coercivity increases as N increases from 5 to 20, and the wasp-waisted shape feature becomes significant as N reaches 20. According to previous results (section 5.3.1 and section 5.3.2), the Pd contributes to about 30 % of the total magnetization of a multilayer with configuration of Pd 50Å/Fe 20Å at 5 K, and the Pd moment is dramatically reduced to near zero at RT. So the RT hysteresis loops of the Pd/Fe multilayers manifest the magnetic reversal of the Fe layers. The first five Fe layers deposited on Si substrate are homogeneous with a small coercivity. The Fe layers deposited later gradually become magnetically harder, which leads to the "tail" extending into higher fields in the hysteresis loop as seen for the multilayer with N = 20.

The coercivity causes the delay of magnetic reversal, and the magnetic reversal in ultrathin film occurs by nucleation and domain wall propagation. The domain wall in a thin film is a Néel wall due to the limited thickness of the film. For a given material, the coercivity of a thin film is influenced by various factors, such as preparation conditions, thickness, crystalline structure, roughness and etc. For the Fe layers deposited in the same film, the structural factors remain the same except for the roughness which increases cumulatively, as demonstrated by the small angle x-ray reflectivity study (section 5.1.1). It is plausible to associate the cumulative increase in the coercivity to the cumulative roughness. A calculation[128] has shown that the roughness increases the wall energy, decreases the thickness of the Néel wall and the size of the Néel domain. Higher magnetic fields are required for domain wall nucleation, and in turn the coercivity is increased. The motion of the domain wall could also be inhibited by the inhomogeneities in the film caused by the roughness, and domain wall pinning will enhance the coercivity. Experimentally, various studies have shown that the coercivity increased as the surface roughness increases. Examples are chemically etched NiFeCo films[129], epitaxial Ni/Cu(100)[130] and Co/Cu(001) thin films[131].

Returning to Fig. 5.18, the "wasp-waisted" shape feature has clearly disappeared from the hysteresis of S_{40} when the temperature was lowered to 200 K, while it is present at all temperatures for S_{55}. This can be explained by assuming that the Pd layers in S_{40} were nearly completely polarised as the temperature decreases. The FM coupling between the Fe layers is enhanced by the Pd polarisation, and the magnetic reversal of the Fe layers becomes more coherent. While in S_{55}, even at the ground state, the center of the Pd layer remains non-magnetic, the FM coupling is weaker than that of S_{40}. The absence of "wasp-waisted" feature for multilayers with thin t_{Pd} could be due to either smaller interfacial roughness as compared to S_{40} and S_{55}, or Fe layers are strongly coupled at all temperatures.

The saturation magnetizations of the multilayers with different N were also measured at 5 K, which were consistent with each other within error. The temperature dependence of the magnetization was also similar. It can be concluded that while the interfacial roughness increases the coercivity, it does not affect the magnetic moment or the spin-stiffness of the multilayers.

The present study show that magnetic coupling between Fe layers across a Pd layer is FM for the *entire* range of Pd thicknesses (t_{Pd} = 10 – 55 Å). According to a theoretical calculation by Wang *et al.*[132], the interlayer coupling has combined

RKKY-like and superexchange contributions. The RKKY-like contribution due to the polarisation of the conduction electrons gives rise to FM interlayer coupling, while the superexchange contribution leads to AF interlayer coupling. Shi *et al.*[123] calculated the interlayer coupling of Fe/Pd(001) multilayer structures, and indicated that due to the spin polarisation in the Pd spacer, the RKKY-like contribution was dominant, consequently, the interlayer coupling with Pd spacer was predominantly FM. This theoretical calculation is consistent with our result, as well as other experimental data[53, 101].

5.4 Polarised Neutron Reflectometry Study

As neutrons interact with both the nuclei and the atomic moments, both chemical and magnetic structures contribute to neutron scattering. Neutron reflectivity will depend on the magnetic profile in the sample. However, it is difficult to determine unequivocally small additional moments associated with enhanced Fe moment and Pd polarisation in a Pd/Fe multilayer by PNR study. There are two main reasons. Firstly, there are uncertainties in measuring the neutron reflectivities due to factors such as mis-alignment, and de-polarising scattering of neutrons (since the sample is not saturated in the applied magnetic field). Secondly, there are too many unknown parameters making the fitting ambiguous. For example, a PNR study on Pd/Co multilayers did not detect any excess moment due to Pd polarisation, and the Co moment was even found to be reduced from its bulk value[133] (which is very likely due to part of Co moments were not aligned by the applied field, lying perpendicular to the sample plane, or in a disordered state). Our calculations with hypothetical models show that the most sensitive way to detect an induced Pd magnetic moment in Pd/Fe multilayers by PNR is to use samples with matched Pd and Fe layer thicknesses. For such samples, the contributions to the even-order superlattice reflections from the chemical structure are ideally zero, so that the sensitivity of the even-order superlattice reflections to non-uniform Pd polarisation effects is greatly enhanced. Non-uniformity is an essential feature, as it gives rise to the development of a new periodicity, while a uniform change throughout the layers would simply lead to a change in contrast that will not give rise to even-order peaks.

Reflectivity scans have been made for two samples, [Pd 60Å/Fe 60Å]$_4$ and [Pd 30Å/Fe 30Å]$_5$, in all four neutron spin-dependent cross sections. The scattering takes place only in the NSF channels, and the small intensity seen in the SF channels is consistent with the measured flipping ratios of the Mezei flippers, verifying that the field was strong enough to align the moments. The NSF reflectivities, R^{++} and R^{--}, measured at RT and 4.5 K are shown in Fig. 5.20 – Fig. 5.23. The positions for the superlattice peaks are as indicated in the figures.

The R^{++}'s at RT (Fig. 5.20 and Fig. 5.22) show dominant odd-order peaks. As expected the 2^{nd} and 4^{th} order peaks are suppressed by the Pd/Fe layer matching. There is a pronounced 2^{nd} order peak in the R^{--} of [Pd 60Å/Fe 60Å]$_4$ at 4.5 K which however is only barely visible at RT. A similar increase takes place for [Pd 30Å/Fe 30Å]$_5$, in the second order peak of R^{--}, but the effect is less visually dramatic as the low-temperature peak is quite broad. The 2^{nd} order peaks in the R^{++} also manifest increases but the change is much smaller compared to the R^{--} channel. Increase of the intensity at the 2^{nd} order peak signals deviations from a simple square-wave scattering length profile, and must be magnetic in origin as the chemical structure can not change on cooling. It can only arise in the current system through a significant and non-uniform magnetic polarisation of the Pd layers, or a change in the moments of the interfacial Fe.

In order to have a quantitative description of the magnetic profile in the Pd/Fe multilayers, the R^{++} and R^{--} are calculated using a matrix method[69] based on the classic optical formalism[70]. The analysis code was developed from the one used to analyze the x-ray reflectometry data on the same samples. The Pd and Fe layer thicknesses and interfacial roughness parameters were all fixed at values obtained from x-ray reflectometry. The bulk Fe moment was taken to be 2.2 μ_B, and the thickness of the interfacial Fe layer was set at its CEMS derived value of 4 Å. The three unknown parameters, μ_i^{Fe}, μ_{Pd} and t_{pol} were adjusted until the calculated reflectivities fit the

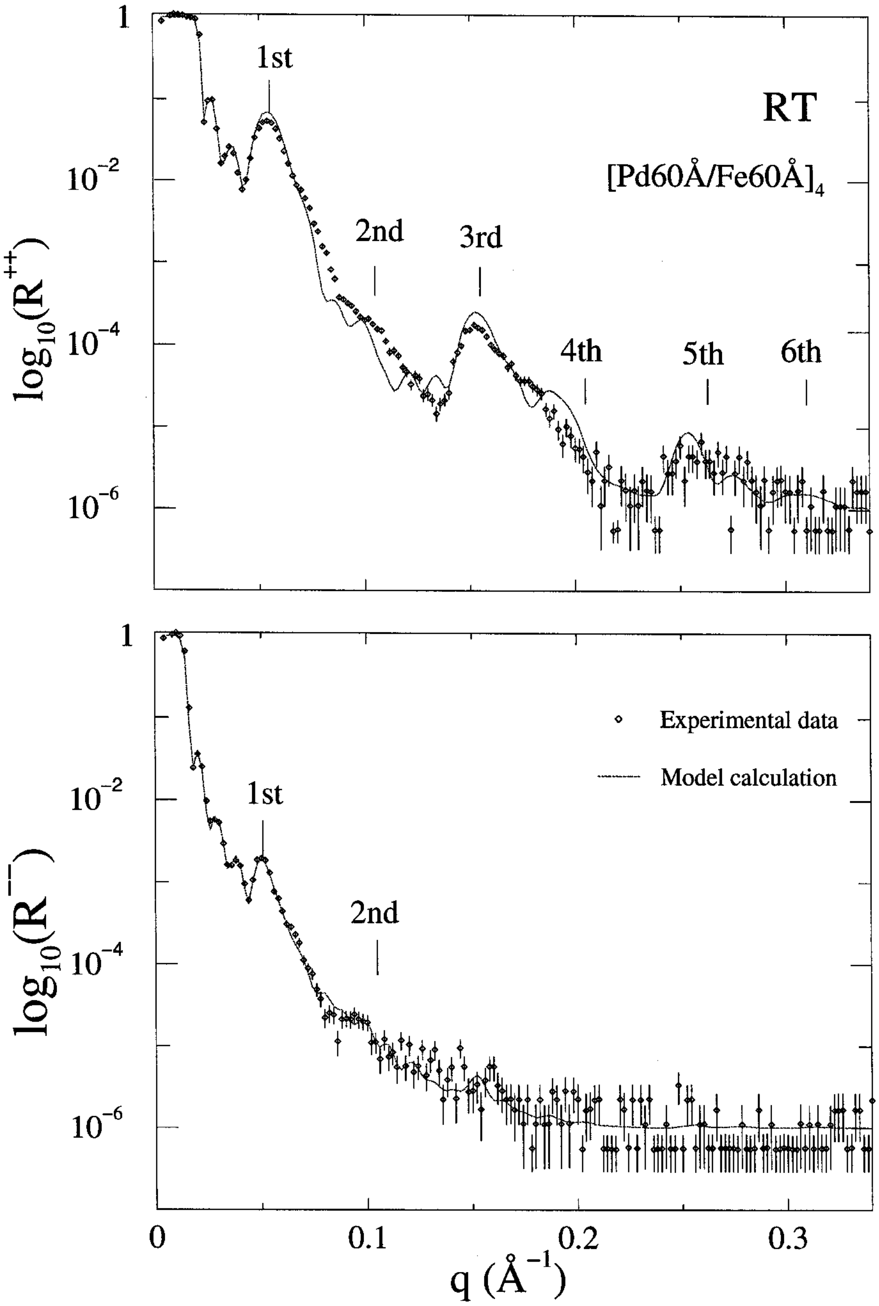

Figure 5.20: Polarised neutron reflectivity data at RT for multilayers [Pd 60Å/Fe 60Å]$_4$ in the spin up-up (R^{++}) channel, and spin down-down (R^{--}) channel. The R^{++} channel is dominated by the chemical structure and shows strong odd-order peaks to 5^{th} order. The R^{--} channel only shows the 1^{st} order peak. The black vertical lines are experimental data with error bars, and the red solid lines are the fits as described in the text.

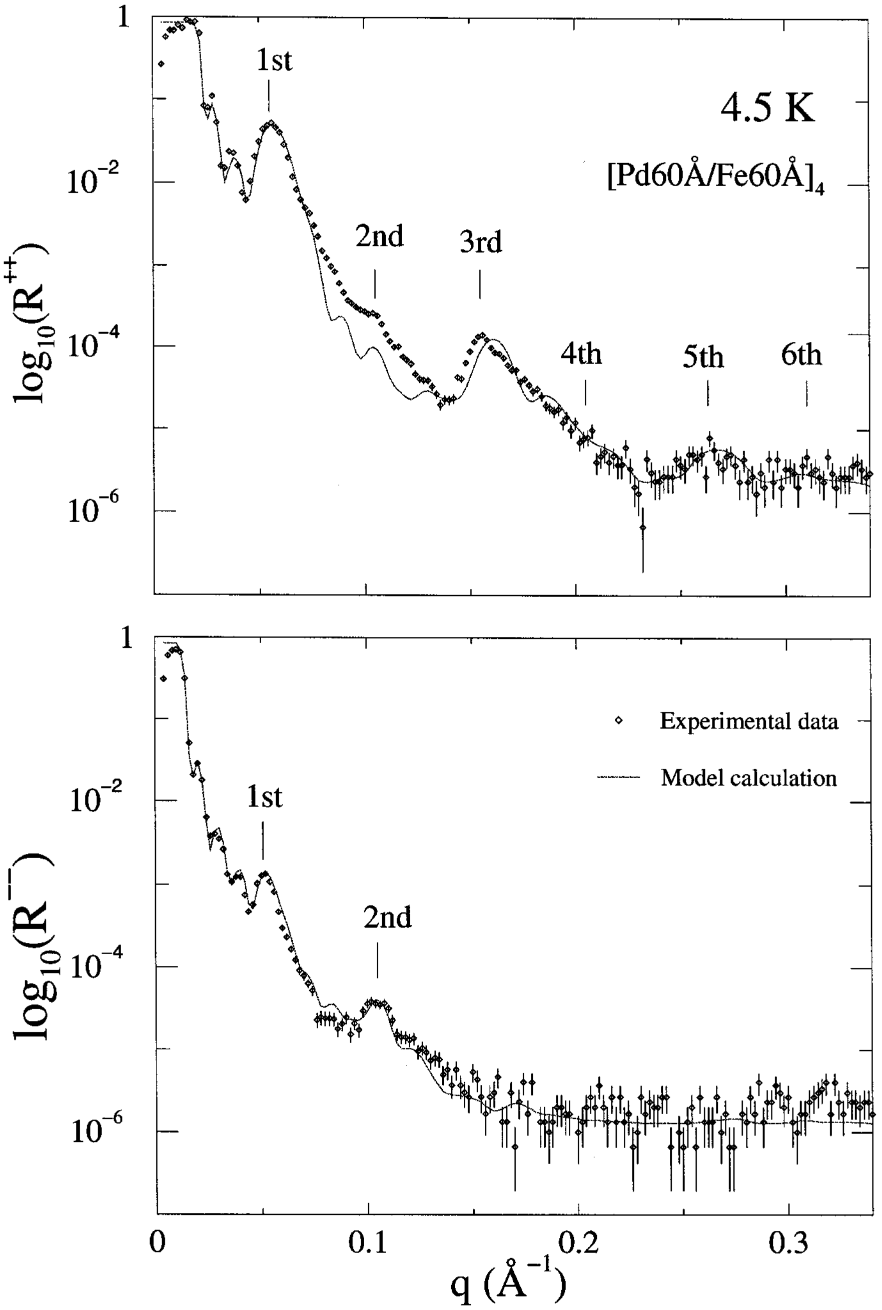

Figure 5.21: Polarised neutron reflectivity data at 4.5 K for multilayers [Pd 60Å/Fe 60Å]$_4$ in the spin up-up (R^{++}) channel and spin down-down (R^{--}) channel. The R^{--} channel shows the growth of the 2^{nd} order peak associated with polarisation in the Pd layer. The large change in the 2^{nd} order R^{--} channel scattering reflects the strong temperature dependence of the Pd polarisation. The black vertical lines are experimental data with error bars, and the red solid lines are the fits as described in the text.

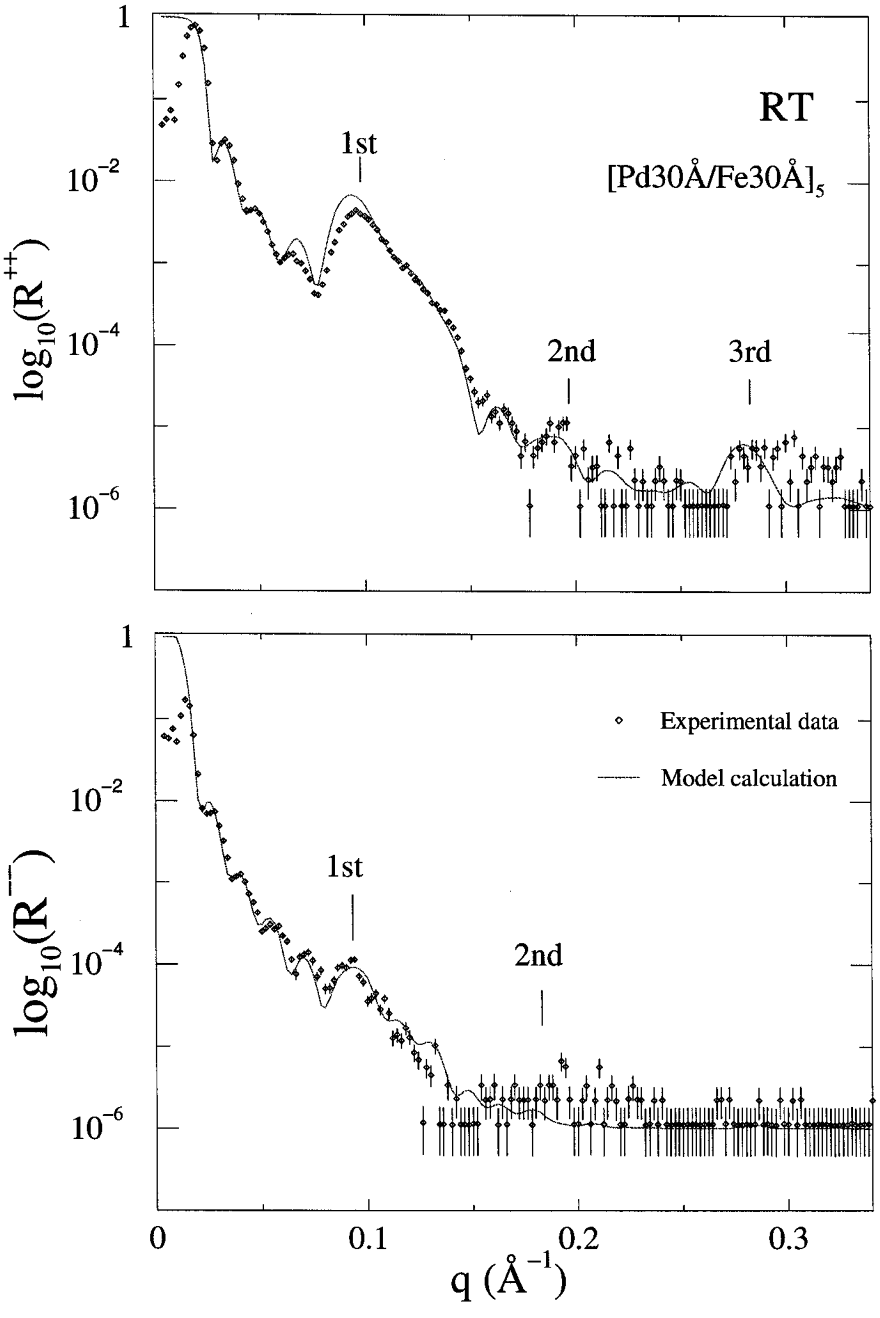

Figure 5.22: Polarised neutron reflectivity data at RT for multilayers [Pd 30Å/Fe 30Å]$_5$ in the spin up-up (R^{++}) channel and spin down-down (R^{--}) channel. The black vertical lines are experimental data with error bars, and the red solid lines are the fits as described in the text.

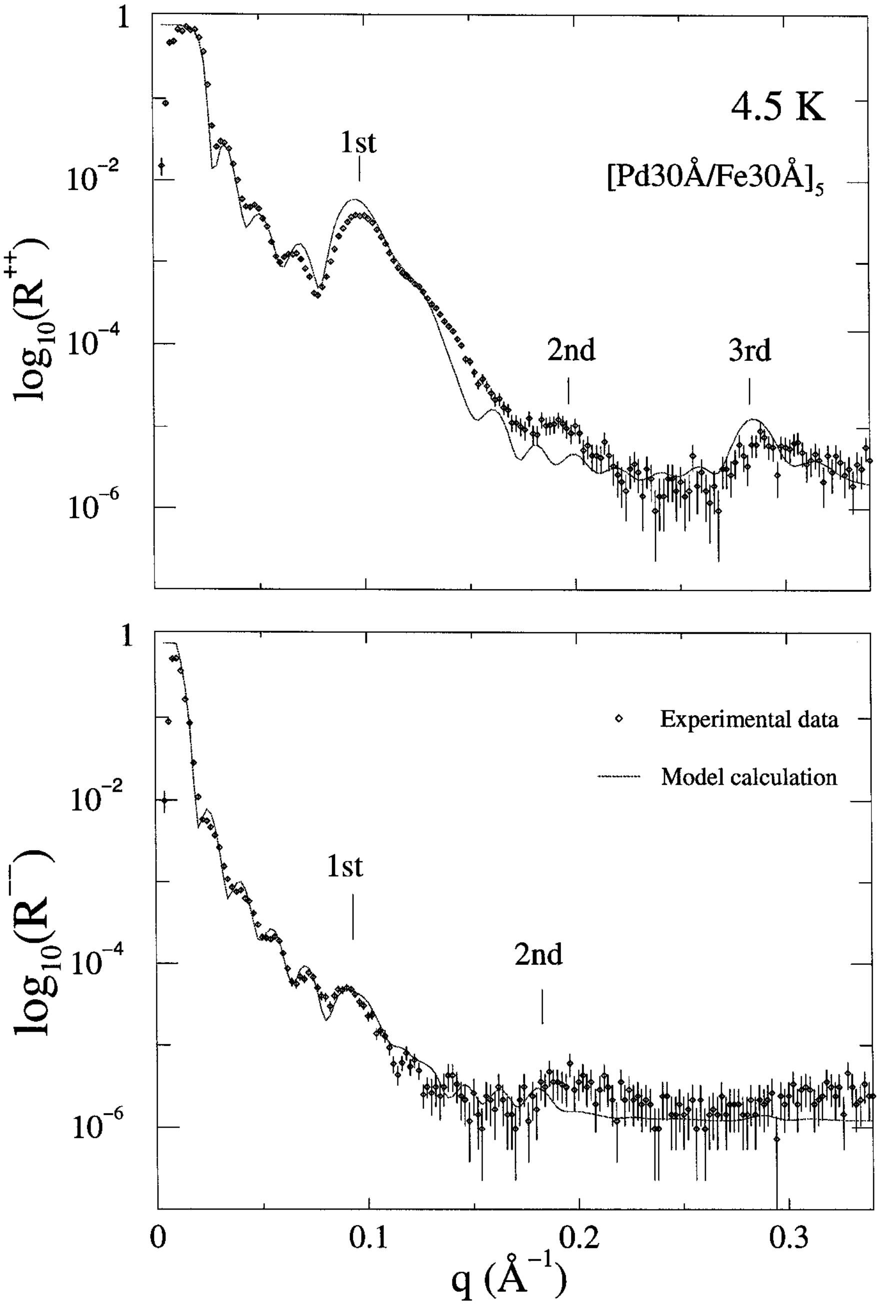

Figure 5.23: Polarised neutron reflectivity data at 4.5 K for multilayers [Pd 30Å/Fe 30Å]$_5$ in the spin up-up (R^{++}) channel and spin down-down (R^{--}) channel. The 2^{nd} order peak in the R^{--} channel is quiet broad. The black vertical lines are experimental data with error bars, and the red solid lines are the fits as described in the text.

experimental data. Spot measurements across the 100 mm diameter samples using x-ray reflectometry showed ~10% average thickness variations which were also included in the PNR fits. They lead only to a broadening of the reflectivity features, and do not affect the intensities. The PNR scattering profile includes the Si substrate with its native $\mathrm{SiO_2}$ layer.

If we use only the 4 Å interfacial Fe component as seen by CEMS and either enhance or reduce the moment to fit the intensity of the 2^{nd} order peak, then the intensities of the 3^{rd} and 4^{th} order peaks become significantly stronger than what is observed. From this we conclude that the 4 Å interfacial Fe component can not, on its own, describe the data. This leads to the conclusion that the Pd layer in [Pd 60Å/Fe 60Å]$_4$ is non-uniformly and significantly polarised at 4.5 K.

The 4.5 K reflectivity calculated with finite μ_{Pd} and $\mathrm{t_{pol}}$ were fitted to the experimental data. The main fitting criterion is that the calculated R^{--} should fit the experimental R^{--} at the 1^{st} and 2^{nd} order superlattice peaks. The values of the three unknown quantities, $\mu_{\mathrm{i}}^{\mathrm{Fe}}$, μ_{Pd} and $\mathrm{t_{pol}}$ with which the R^{--} measured at 4.5 K could be satisfactorily fitted, turn out to have a wide range: $\mu_{\mathrm{i}}^{\mathrm{Fe}} = 2.4 \pm 0.4\ \mu_{\mathrm{B}}$, $\mu_{\mathrm{Pd}} = 0.4 \pm 0.2\ \mu_{\mathrm{B}}$, and $\mathrm{t_{pol}} = 21 \pm 9$ Å. The magnetometry measurements have suggested that the value of $\mu_{\mathrm{Pd}} \cdot \mathrm{t_{pol}}$ is a constant for samples with different Fe thicknesses. So we require that the values of μ_{Pd} of [Pd 30Å/Fe 30Å]$_5$ and [Pd 60Å/Fe 60Å]$_4$ should be the same at the same value of $\mathrm{t_{pol}}$. Furthermore, we require that the value of $\mathrm{M'_{Pd}}+(\mu_{\mathrm{i}}^{\mathrm{Fe}}-\mu_{\mathrm{b}}^{\mathrm{Fe}})\times 2\mathrm{t_i}$ from the PNR analysis to be consistent with the result from our magnetometry measurement ($5.7 \pm 0.4\ \mu_{\mathrm{B}}\cdot$AL, see p. 97). With these criteria, the values of the three unknown quantities were narrowed down to $\mu_{\mathrm{i}}^{\mathrm{Fe}} = 2.4 \pm 0.1\ \mu_{\mathrm{B}}$, the thickness of the polarised Pd layer $\mathrm{t_{pol}} = 20 \pm 4$ Å, and an average Pd moment of $\mu_{\mathrm{Pd}} = 0.32 \pm .02\ \mu_{\mathrm{B}}$. Since $\mu_{\mathrm{i}}^{\mathrm{Fe}} = 2.4\ \mu_{\mathrm{B}}$ at 4.5 K, using our CEMS result, this value is reduced to 2.2 μ_{B} at RT. From the fitting of the RT PNR reflectivities of [Pd 60Å/Fe 60Å]$_4$ and [Pd 30Å/Fe 30Å]$_5$, we see that the spin polarisation extends to 15 ± 10 Å from the interface leaving an average Pd moment of 0.15 ± 0.07 μ_{B} at RT.

The neutron reflectivity is the square of the Fourier transform of the scattering length density ρ (Eqn. (3.16)). The values of ρ corresponding to the best fit parameters of [Pd 30Å/Fe 30Å]$_5$ and [Pd 60Å/Fe 60Å]$_4$ at 4.5 K are shown in Fig. 5.24 and Fig. 5.25. The nuclear (ρ_n) and magnetic (ρ_M) scattering length densities of Fe are comparable in magnitude and considerably stronger than those of Pd, so when added in the R^{++} channel, the large contrast between the scattering densities of Fe and Pd causes the R^{++} channel to be dominated by the chemical structure distribution. However, as ρ_n and ρ_M are subtracted in the R^{--} channel, it so happens that ρ_{Fe} nearly matches ρ_{Pd}, so that the large-scale structural contrast almost vanishes, and the effect of non-uniform moment distributions on ρ stand out in the R^{--} channel. This explains why the 2nd order peak is much more pronounced in the R^{--} channel than in the R^{++} channel. In [Pd 30Å/Fe 30Å]$_5$, 30 Å of Pd is uniformly polarised, the enhanced Fe moment at the Pd/Fe interfaces is the only non-uniform feature seen in the calculated R^{--} profile. While in [Pd 60Å/Fe 60Å]$_4$, 20 Å of Pd from the interface is magnetically polarised, leaving the center 20 Å of Pd non-magnetic. Both the interface Fe moment and the non-uniform Pd polarisation seen in the calculated R^{--} profile give rise to the distinct 2nd order superlattice peak in the low-T R^{--} profile of [Pd 60Å/Fe 60Å]$_4$.

In summary, we have undertaken a series of complementary measurements at both RT and low-T. With microscopic data from CEMS, we found that 2.0 ± 0.3 AL of Fe at each interface is interface-like. The variation of the Fe moment with temperature was determined from the temperature dependence of hyperfine field of Fe, and the ground state moment of interface Fe was found to be 2.42 ± 0.05 μ_{B}, slightly enhanced from bulk Fe value of 2.22 μ_{B}. The magnetometry measurements revealed that Pd layers are significantly polarised at low temperature. Combining CEMS and magnetometry data, the temperature dependence of total Pd polarisation was determined for the first time. This result suggests that very little Pd polarisation survives at RT, and that the Curie temperature is much lower for magnetically polarised Pd than for Fe thin films. The PNR measurements were performed on multilayers with matched Pd and Fe layer thicknesses in order to minimize the structural contributions to the

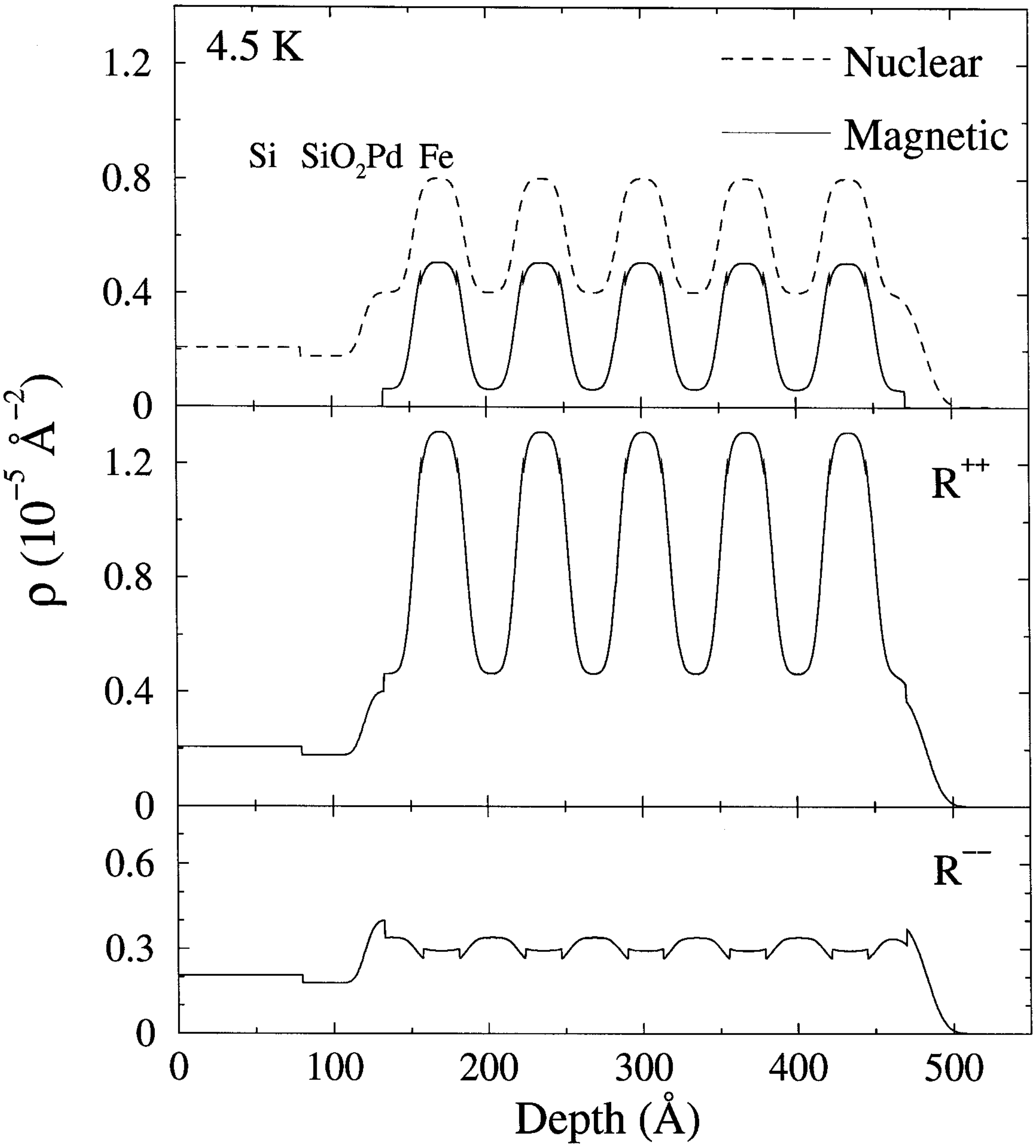

Figure 5.24: Neutron scattering length densities at 4.5 K for multilayers [Pd 30Å/Fe 30Å]$_5$ in the non-spin-flip channels. Top: Magnetic and nuclear scattering densities. Middle: magnetic and nuclear scattering add in the R^{++} channel. Bottom: The subtraction of magnetic from nuclear scattering density gives R^{--} channel.

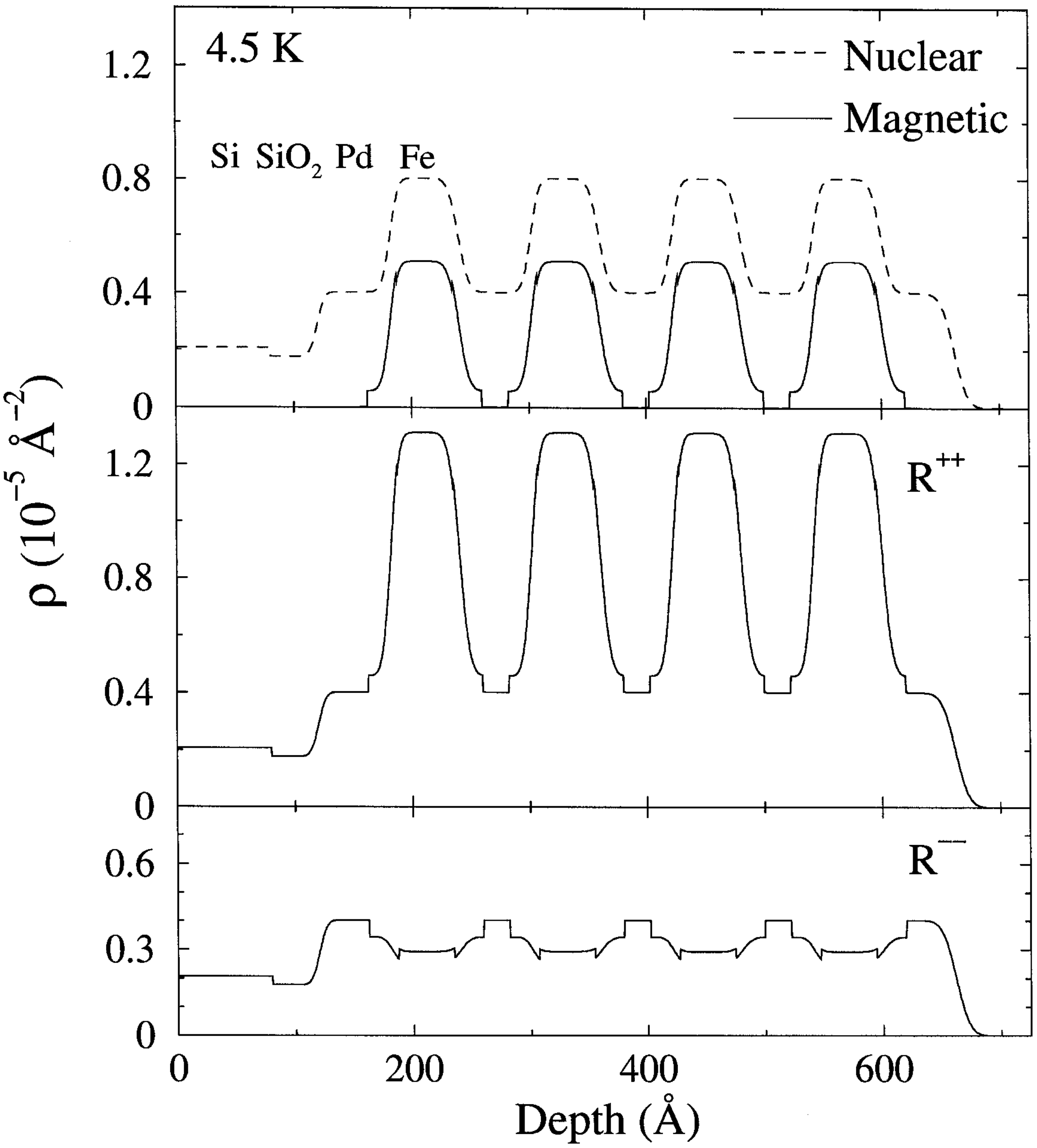

Figure 5.25: Neutron scattering length densities at 4.5 K for multilayers [Pd 60Å/Fe 60Å]$_4$ in the non-spin-flip channels. Top: Magnetic and nuclear scattering densities. Middle: The scattering density in the R^{++} channel. Bottom: The scattering density in R^{--} channel.

even-order superlattice reflections and thus greatly enhancing the sensitivity to Pd polarisation effects. Using CEMS and magnetometry data as a guide, the analysis of PNR data allows us to determine the induced moment on the Pd atom and the extent of the Pd polarisation.

From the intersection of the results of these complementary measurements we have been able to determine with reasonable accuracy the interface moments and the extent of Pd polarisation. Specifically, at 4.5 K, 20 ± 4 Å(9 ± 2 AL) of Pd layer from Fe surface is magnetically polarised with an average moment of 0.32 ± 0.02 μ_B. The Pd polarisation of 0.32 ± 0.02 μ_B per Pd atom is consistent with values obtained from dilute bulk alloys[30, 32], and is in the same order as the value obtained for MBE-grown films[55] as well. However, our polarisation distance, t_{pol}, is significantly larger than those obtained from previous measurements[50, 51, 52, 55] ($t_{pol} \leq 4$ AL). It should be noted that all previous experiments were carried out at RT[50, 51, 55] or 77 K[52], at which both the magnitude and extent of Pd polarisation are reduced from the ground state value as demonstrated in our study. Thus the values of t_{pol} from these studies are expected to be larger at 5 K than what have been reported, and could agree better with our result. Our value of t_{pol} is also significantly larger than the value of 2 AL predicted by various theoretical calculations[56, 57]. Although an interfacial roughness of about 3 AL exists in our multilayers, this is unlikely to account for the large discrepancy in t_{pol}. Our much large value of t_{pol} suggests that the band structure calculations need to be refined to improve the accuracy.

A phenomenological picture can be drawn using the values obtained in this study. Since the average value for the Pd polarisation is quite close to the number of holes in the Pd *d*-bands[22, 67], it is reasonable to assume that for a significant distance from the Fe surface, the exchange splitting, Δ, of the Pd *d*-band is complete, leaving the spin-up *d*-band full. The moment in the Pd atoms results from the 0.36 μ_B of spin-down holes. It seems reasonable to suppose that with each layer further away from the Fe surface, Δ diminishes. It is in fact possible that Δ decreases with the layer number at a fast enough rate so that one passes from having just spin-down holes to having no polarisation within the space of two layers, as shown in the Fig. 5.26.

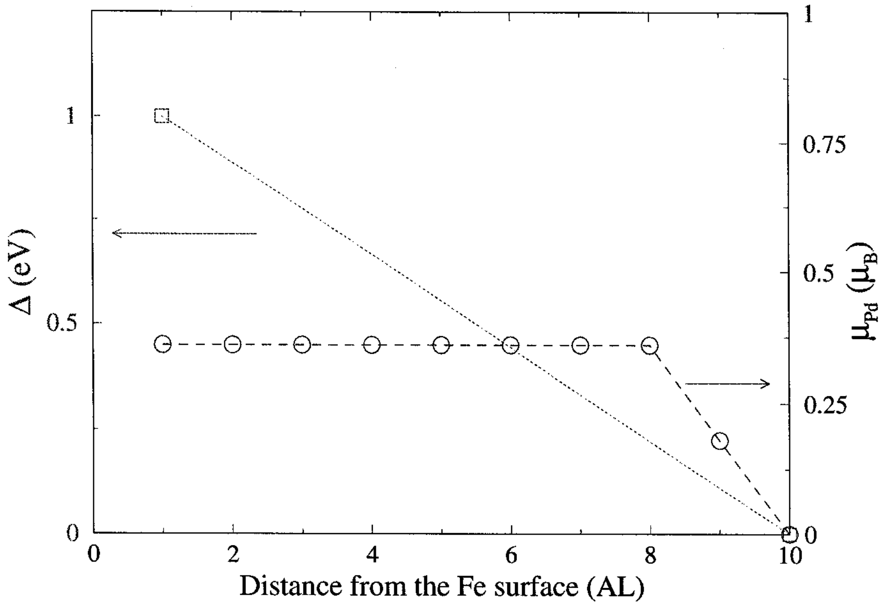

Figure 5.26: A phenomenological picture of the exchange splitting (red □) and induced polarisation (blue O) of Pd atoms varying with the distance to Fe surface. The Δ value for 1 AL is from reference: H. Huang *et al.*, *Surf. Sci.*, 172:363, 1986.

Turning now to the values for the interfacial Fe, we have found that the 2.0 ± 0.3 atomic layers at the interface have an average Fe moment of 2.42 ± 0.05 μ_B, a 10 % increase from bulk Fe. Our results are in agreement with a recent magnetic circular x-ray dichroism experiment[60]. However, the increase in the interface Fe moment is lower than that predicted by calculations on an Fe/Pd(001) system[56, 58, 59]. According to these calculations, the enhancement in the Fe moment due to hybridisation between Fe and Pd *d*-bands should be 0.6 μ_B[58, 59] – 1 μ_B[56]. Our values for the interface Fe moment and thickness indicate that the presence of the Pd surface has much less influence on the magnetism of Fe compared to the role of Fe on the magnetism of Pd. Only the moment on the Fe atoms within about 2 atomic layers nearest to the interface is enhanced relative to the bulk Fe. Moreover, the enhancement in the Fe moment is most likely to be attributed to the broken symmetry at the interface, rather than the hybridisation of the Fe and Pd *d*-bands. This follows from the observation that the Fe moment at a Pd/Fe interface is not higher than the Fe moment at a Ag/Fe interface[15, 16]. The enhancement in the Fe moment at a Ag/Fe interface is due to the broken symmetry at the interface since hybridisation between Ag and Fe *d*-bands is negligible[14].

6

Conclusions

The main topic of this thesis has been to investigate the magnetic properties of Pd/Fe multilayers with the principal goal of determining the extent to which the Pd layers are polarised by the Fe atoms and the average moment induced on each Pd atom. Although Pd/Fe multilayers have been the subject of several studies, no consensus on the behavior of magnetically polarised Pd has emerged. This work has the novel feature of applying a wide range of characterization techniques on the *same* sample. These techniques included x-ray diffraction, CEMS, magnetometry and PNR. As a consequence we are able to offer answers to the above questions with a great deal more confidence than in previous work.

Ag/Fe multilayers with immiscible interfaces were first investigated to confirm that analysis of small-angle x-ray data give a fast and accurate determination of the bilayer thickness of the multilayers. The Pd and Fe individual thicknesses were then obtained by fitting the small-angle x-ray reflectivity profiles, while high-angle x-ray diffraction patterns revealed the preferential orientations of the layers perpendicular to the film plane. This structural information is crucial in calculating the magnetic moments.

The CEMS study has been carried out to determine the values of interfacial Fe thickness and moment, and the temperature dependence of the hyperfine field of Fe in the Pd/Fe multilayers. In the CEMS study of Ag/Fe multilayers with no polarisation moment in Ag layers, we confirmed that the variation of hyperfine field with temperature indeed reflects the temperature dependence of the magnetisation of Fe. So the Fe contribution to the total magnetisation of Pd/Fe was determined using the temperature dependence of hyperfine field obtained from the CEMS study. Combining CEMS and magnetometry studies allows us to distinguish the individual Fe and Pd contributions to the observed temperature dependence of the total magnetisation. The PNR study, which is the key of this thesis, has been employed to probe the magnetic profile in the Pd/Fe multilayers with the guidance of CEMS and magnetometry measurements. Multilayers with matched Pd and Fe layer thicknesses were used in the PNR study in order to minimize the structural contributions to the even-order superlattice reflections and thus greatly enhance the sensitivity to Pd polarisation effects.

From the intersection of the results of these complementary measurements we have been able to determine with reasonable accuracy the induced moment on the Pd atom, the extent of the Pd polarisation, and the value of the interfacial Fe moment. Specifically, we have found that the average value for the Pd polarisation is 0.32 ± 0.02 μ_B, a figure which is quite close to the known number of holes in the Pd *d*-bands[22, 67]. The Pd layer has been found to be polarised for a distance of 20 ± 4 Å from the Fe surface, which corresponds to about 9 ± 2 atomic layers of Pd. This value of the extent of Pd polarisation, t_{pol}, is significantly larger than the value of 2 AL predicted by theoretical calculations[56, 57]. Although interfacial roughness of about 3 AL exists in our multilayers, it is unlikely to account for the large discrepancy in t_{pol}. Our much larger value of t_{pol} indicates that the band structure calculations need to be refined to improve this accuracy.

Taking together the values from our study, we propose that, for a significant distance from an Fe surface, the exchange splitting, Δ, of the Pd *d*-bands is large enough to ensure that the spin-up band is full and the moment in the Pd atoms results from the 0.36 μ_B of spin-down holes. It seems reasonable to suppose that with each layer further away from the Fe surface, Δ diminishes. It is in fact possible that Δ decreases with layer number at a fast enough rate so that one passes from having just spin-down holes to having no polarisation within the space of two layers.

Turning now to the value of the interface Fe moment, we have found that 2.0 ±

0.3 AL of Fe at the interface has an average moment of 2.42 ± 0.05 μ_B, about a 10 % increase from bulk Fe. Our result is in agreement with a previous work[60], but in conflict with various theoretical calculations[58, 56, 59] which predicted higher enhancements in the interface Fe moment due to Pd and Fe *d*-bands hybridisation. Our values for the interface Fe indicate that the presence of the Pd surface has relatively less influence on the magnetism of Fe as compared to the role of Fe on Pd. Only about 2 atomic layers of Fe nearest to the interface have enhanced moments. Moreover, the enhancement in the Fe moment is attributed to the broken symmetry at the interface, rather than the hybridisation of the Fe and Pd *d*-bands.

The following topics are suggested for future studies:

- Study the spin excitation in magnetically polarised Pd layers. For example, by investigating the temperature dependence of the Pd polarisation for samples with different Pd thicknesses, one can learn if there is any size effect of the spin excitation in the Pd layer, and cross over from $T^{3/2}$ to linear temperature dependence of the Pd polarisation.

- Study the role of roughness on the Pd polarisation by comparing results of Pd/Fe multilayers prepared by sputtering and MBE.

- The magnitude and extent of magnetic polarisation in Pd layer can be studied for Co/Pd and Ni/Pd multilayers by combining magnetometry and PNR measurements. The results may clarify how the Pd polarisation is affected by the 3-*d* magnetic metals.

Appendices

A.1 Low-angle X-ray Reflectivity of Multilayers

X-ray is essentially an electromagnetic plane wave. The propagations of electric (**E**) and magnetic (**H**) field components of an x-ray in a medium obey Maxwell's equations:

$$\nabla \times \mathbf{E} = -\frac{\partial \mathbf{B}}{\partial t}, \tag{A.1}$$

$$\nabla \times \mathbf{H} = \mathbf{J} + \frac{\partial \mathbf{D}}{\partial t}, \tag{A.2}$$

where $\mathbf{D} = \varepsilon\mathbf{E}$, $\mathbf{B} = \mu\mathbf{H}$, and ε and μ are the electric permittivety and magnetic permeability, respectively. When combined, the Maxwell's equations lead to the propagation equation of the electric field known as Helmholtz equation,

$$\nabla^2\mathbf{E} + \mathrm{k}^2\mathbf{E} = 0. \tag{A.3}$$

where $\mathrm{k} = \mathrm{nk_o}$, is the wave vector in the medium with refractive index of n, which is related to the ε and μ by $\mathrm{n}^2 = \varepsilon\mu$. The electric field which is the solution of Eqn. (A.3) is given by,

$$\mathrm{E} = \tilde{\mathrm{A}}\mathrm{e}^{\mathrm{i}\mathbf{k}\cdot\mathbf{r}}, \tag{A.4}$$

and the intensity of the x-ray is given by $|\tilde{\mathrm{A}}|^2$. The calculation of reflectivity of a medium is to relate the electric components of the incident x-ray and reflected x-ray. There are several approaches to calculate the reflectivity of a multilayer, which is a stratified medium consisting of many homogeneous films piling along the same direction perpendicular to the film plane. We follow the method of Vidal[70] for the reflectivity calculation in the fitting program.

Consider a TE x-ray wave impinging on a stratified medium with ideally flat interfaces, the incident angle is θ and the incident plane is x-y. Assuming lateral invariance in the incident plane, the electric field can be written as, $\mathrm{E} = \tilde{\mathrm{A}}\mathrm{e}^{\mathrm{ik_z z}}\mathrm{e}^{\mathrm{ik_{\|}r_{\|}}}$, and Eqn. (A.3) can be reduced to one-dimentional Helmholtz equation,

$$\left(\frac{\mathrm{d}^2}{\mathrm{dz}^2} + \mathrm{k_z^2}\right)\mathrm{E(z)} = 0. \tag{A.5}$$

Then the electric field in j^{th} layer can be written in terms of incident wave and reflected wave,

$$\mathrm{E(z)} = \tilde{\mathrm{A}}\mathrm{e}^{-\mathrm{ik_{jz}z}} + \tilde{\mathrm{B}}\mathrm{e}^{\mathrm{ik_{jz}z}}, \tag{A.6}$$

in which, straight forwardly,

$$\mathrm{k_j} = \mathrm{k_o n_j}, \tag{A.7}$$

$$\mathrm{k_{jz}} = \sqrt{\mathrm{k_j^2} - \mathrm{k_{j\|}^2}} = \sqrt{\mathrm{k_o^2 n_j^2} - \mathrm{k_o^2 n_j^2}\cos^2\theta_\mathrm{j}}. \tag{A.8}$$

According to the Snell-Descartes' second law,

$$\cos\theta \;=\; \mathrm{n_1}\cos\theta_1 \;=\; \mathrm{n_2}\cos\theta_2 \;=\; \cdots \;= \mathrm{n_j}\cos\theta_\mathrm{j}. \tag{A.9}$$

Then we have $\mathrm{k_{jz}} \;=\; \mathrm{k_o}\sqrt{\mathrm{n_j^2} - \cos^2\theta}$.

If an interface is positioned at $\mathrm{z_o}$, ignoring the subscript z, the electric field in medium 2 and 1 can be written as,

$$\mathrm{E(z)} \;=\; \tilde{\mathrm{A}}\mathrm{e}^{-\mathrm{ik_2z}} + \tilde{\mathrm{B}}\mathrm{e}^{\mathrm{ik_2z}}, \quad (\mathrm{z} > \mathrm{z_o}), \tag{A.10}$$

$$\mathrm{E(z)} \;=\; \tilde{\mathrm{C}}\mathrm{e}^{-\mathrm{ik_1z}} + \tilde{\mathrm{D}}\mathrm{e}^{\mathrm{ik_1z}}, \quad (\mathrm{z} < \mathrm{z_o}). \tag{A.11}$$

The continuity of the electric field and its first derivative across the interface can be written in terms of the matrix,

$$\begin{bmatrix} \tilde{\mathrm{A}} \\ \tilde{\mathrm{B}} \end{bmatrix} = \frac{1}{2}\begin{bmatrix} m_{11} & m_{12} \\ m_{21} & m_{22} \end{bmatrix}\begin{bmatrix} \tilde{\mathrm{C}} \\ \tilde{\mathrm{D}} \end{bmatrix} \tag{A.12}$$

where

$$\mathrm{m_{11}} = \alpha_1\ \mathrm{e}^{-\mathrm{i(k_1-k_2)z}}, \tag{A.13}$$

$$\mathrm{m_{12}} = \alpha_2\ \mathrm{e}^{+\mathrm{i(k_1+k_2)z}}, \tag{A.14}$$

$$\mathrm{m_{21}} = \alpha_2\ \mathrm{e}^{-\mathrm{i(k_1+k_2)z}}, \tag{A.15}$$

$$\mathrm{m_{22}} = \alpha_1\ \mathrm{e}^{+\mathrm{i(k_1-k_2)z}}, \tag{A.16}$$

$$\alpha_1 = 1 + \frac{\mathrm{k_1}}{\mathrm{k_2}}, \tag{A.17}$$

$$\alpha_2 = 1 - \frac{\mathrm{k_1}}{\mathrm{k_2}}. \tag{A.18}$$

and the subscript o in $\mathrm{z_o}$ is neglected for simplicity. The transfer matrix M relates the components of the electric fields in the two media separated by an interface. The transfer matrix ($\mathrm{M_{total}}$) for a stratified medium consisting of many thin homogeneous films piling along z(Figure 3.2) is given by the product of the matrices of all the interfaces,

$$\mathrm{M_{total}} \;=\; \mathrm{M_{N,N-1}M_{N-1,N-2}\cdots M_{2,1}}. \tag{A.19}$$

$\mathrm{M_{total}}$ relates the components of the electric fields of the incident wave, reflected wave and transmit wave as

$$\begin{bmatrix} 1 \\ r \end{bmatrix} = \mathrm{M_{total}}\begin{bmatrix} 0 \\ t \end{bmatrix} \tag{A.20}$$

where t and r are the transmission and specular reflection coefficients. Then the reflection and transmission amplitudes can be calculated from the matrix elements of $\mathrm{M_{total}}$ by

$$\mathrm{R} = \left(\frac{\mathrm{m_{21}}}{\mathrm{m_{11}}}\right)^2, \tag{A.21}$$

$$\mathrm{T} = \left(\frac{1}{\mathrm{m_{11}}}\right)^2. \tag{A.22}$$

For a real multilayer, the effect of interface roughness have to be included into the reflectivity calculation. This is usually done by using an analytical function to model the electron profile. For a diffused interface, the variation in composition at the interface can be best described by an error function[79]. At a rough interface, the interface position varies randomly at different depths with respect to an average interface interface. If the probability distribution of the interface height deviation from the mean position follows a Gaussian distribution, the effective electron density profile also follows an error function. The reflectivity can be calculated exactly using the electron profile, or using a matrix method[69] as well. The transform matrix of a rough interface is given by [70]:

$$\begin{bmatrix} \tilde{\mathrm{A}} \\ \tilde{\mathrm{B}} \end{bmatrix} = \frac{1}{2} \begin{bmatrix} \mathrm{m}_{11}\ \mathrm{e}^{-(\mathrm{k}_1-\mathrm{k}_2)^2\frac{\sigma^2}{2}} & \mathrm{m}_{12}\ \mathrm{e}^{-(\mathrm{k}_1+\mathrm{k}_2)^2\frac{\sigma^2}{2}} \\ \mathrm{m}_{21}\ \mathrm{e}^{-(\mathrm{k}_1+\mathrm{k}_2)^2\frac{\sigma^2}{2}} & \mathrm{m}_{22}\ \mathrm{e}^{-(\mathrm{k}_1-\mathrm{k}_2)^2\frac{\sigma^2}{2}} \end{bmatrix} \begin{bmatrix} \tilde{\mathrm{C}} \\ \tilde{\mathrm{D}} \end{bmatrix} \tag{A.23}$$

where σ is the root-mean-square value of the roughness.

A.2 Neutron Reflectivity of Multilayers

Neutron is a particle with practically zero electric charge. A beam of neutrons have wave-like properties and can be described by a wave of wavelength λ appropriate to neutron velocity v, and given by the de Broglie relation,

$$\lambda = h/mv \tag{A.24}$$

where h is the Planck's constant. The wave function of the neutron satisfies the Schrödinger equation:

$$\left(-\frac{\hbar^2}{2m}\nabla^2 + \mathrm{V}(\mathbf{R})\right)\Psi = \mathrm{E}\Psi. \tag{A.25}$$

where $\mathrm{V}(\mathbf{R})$ is the neutron potential energy at position $\mathbf{R}$. For a homogeneous magnetic layer, the mean interaction potential energy can be written as,

$$\mathrm{V} = \frac{2\pi\hbar^2}{m}\rho\cdot\mathrm{b}, \tag{A.26}$$

where $\mathrm{b} = \mathrm{b_n} + \mathrm{b_m}$, $\mathrm{b_n}$ and $\mathrm{b_m}$ are the neutron nuclear and magnetic scattering lengths, respectively. $\mathrm{b_m}$ is related to the in plane magnetic moment $\mathbf{M}_{\|}$ (given in μ_B per atom) by $\mathrm{b_m} = 2.696\ \boldsymbol{\sigma}\cdot\mathbf{M}_{\|}$ fm.

The Schrödinger equation (A.25) can be reduced to a Helmholtz propagation equation:

$$\frac{\mathrm{d}^2\Psi}{\mathrm{dr}^2} + \mathrm{k}^2\Psi = 0 \tag{A.27}$$

with $\mathrm{k}^2 = \frac{2m}{\hbar^2}(\mathrm{E}-\mathrm{V})$. The refractive index n is defined as

$$\mathrm{n} = \frac{\mathrm{k}}{\mathrm{k_o}} = \left(1-\frac{\mathrm{V}}{\mathrm{E}}\right)^{1/2} \approx 1-\frac{\lambda^2}{2\pi}\rho\mathrm{b}, \tag{A.28}$$

and the critical angle is given by

$$\theta_c = \sqrt{\frac{\rho b}{\pi}}\lambda \tag{A.29}$$

Assume the multilayer has translational invariance in the x-y plane, the neutron wave function can be written as, $\Psi(r) = \psi(z)e^{ik_{\|}\cdot r_{\|}}$, with $k_{\|} = k_o \cos\theta$, where θ is the incident angle and Eqn. (A.27) reduced to the one-dimensional Helmholtz equation,

$$\left(\frac{d^2}{dz^2} + k_z^2\right)\psi(z) = 0 \tag{A.30}$$

with $k_z = (k^2 - k_{\|}^2)^{1/2} = \left[(k_o n)^2 - (k_o \cos\theta^2\right]^{1/2}$. For a non-magnetic medium, or a magnetic medium with magnetisation parallel or anti-parallel to the magnetic field, only non-spin-flip (NSF) scatterings occur, giving rise to NSF reflectivities, i.e., spin up-up (R^{++}) and spin down-down (R^{--}) reflectivities. The magnetic moment contributes to the reflectivity via the neutron scattering length, $b = b_n \pm b_m$, where $+$ and $-$ signs are for spin-up and spin-down electrons respectively. Eqn. (A.30) has a general solution

$$\psi^S(z) = Ae^{ik_z^S \cdot z} + Be^{-ik_z^S \cdot z}, \tag{A.31}$$

where $s = +$ and $-$ are for spin-up and spin-down electrons respectively. Eqn. (A.31) has the same form as Eqn. (A.6), which is the wavefunction of the electric field of an x-ray. The matrix method using to calculate the x-ray reflectivity described in Appendix *A*.1, and formulae from Eqn. (A.10) – Eqn. (A.21) can be applied directly to calculate the NSF neutron reflectivities of a multilayer.

If the magnetization in a medium has an angle of θ_M with respect to the neutron spin, a spin flipping (SF) process occurs, giving rise to the spin up-down (R^{+-}) or down-up (R^{-+}) reflectivities. The NSF and SF reflectivities depend on θ_M. Here the calculation of neutron reflectivities of a general case in which the effective magnetic fields in two adjacent media have a relative angle of θ_{12} is given. When the neutron is incident at an angle of θ on an interface, which is in the x-y plane at position z, the wave functions are written as:

$$\psi_i = A_i e^{ik_i^+ z} + B_i e^{-ik_i^+ z} + C_i e^{ik_i^- z} + D_i e^{-ik_i^- z} \tag{A.32}$$

with $i = 1, 2$ for the neutron in media 1 and 2 respectively, and $k_i = (k^2 - k_{\|}^2)^{1/2} = \left[(k_o n)^2 - (k_o \cos\theta)^2\right]^{1/2}$. The neutron quantization axis is defined as the direction of the effective field in the medium. If the effective fields in the adjacent medium differ by θ_{12}, in medium 2, ψ_1 should be written as $R(\Theta)\psi_1$, where the rotation matrix $R(\Theta)$ is a 4×4 matrix expressed by Θ which is half of θ_{12},

$$\begin{bmatrix} \cos(\Theta) & 0 & \sin(\Theta) & 0 \\ 0 & \cos(\Theta) & 0 & \sin(\Theta) \\ -\sin(\Theta) & 0 & \cos(\Theta) & 0 \\ 0 & -\sin(\Theta) & 0 & \cos(\Theta) \end{bmatrix} \tag{A.33}$$

The boundary conditions require that the neutron wave-functions of and their first order derivatives are continuous at z respectively, which can be written in terms of the matrix,

$$\mathrm{M}_2 \begin{bmatrix} \mathrm{A}_2 \\ \mathrm{B}_2 \\ \mathrm{C}_2 \\ \mathrm{D}_2 \end{bmatrix} = \mathrm{R}(\Theta)\mathrm{M}_1 \begin{bmatrix} \mathrm{A}_1 \\ \mathrm{B}_1 \\ \mathrm{C}_1 \\ \mathrm{D}_1 \end{bmatrix} \tag{A.34}$$

with

$$\mathrm{M}_\mathrm{i} = \begin{bmatrix} e^{\mathrm{i}k_\mathrm{i}^+ z} & e^{-\mathrm{i}k_\mathrm{i}^+ z} & 0 & 0 \\ k_\mathrm{i}^+ e^{\mathrm{i}k_\mathrm{i}^+ z} & -k_\mathrm{i}^+ e^{-\mathrm{i}k_\mathrm{i}^+ z} & 0 & 0 \\ 0 & 0 & e^{\mathrm{i}k_\mathrm{i}^- z} & e^{-\mathrm{i}k_\mathrm{i}^- z} \\ 0 & 0 & k_\mathrm{i}^- e^{\mathrm{i}k_\mathrm{i}^- z} & -k_\mathrm{i}^- e^{-\mathrm{i}k_\mathrm{i}^- z} \end{bmatrix} \tag{A.35}$$

Then the transfer matrix M_{12}, relating the components of the wave-functions in medium 1 and 2 separated by an interface, is given by:

$$\mathrm{M}_{12} = \mathrm{M}_2^{-1}\mathrm{R}(\Theta)\mathrm{M}_1 \tag{A.36}$$

Incorporated the interfacial roughness, M_{12} is given by:

$$\mathrm{M}_{12} = \frac{1}{2}\begin{bmatrix} \cos\Theta \mathrm{m}_{11} & \sin\Theta \mathrm{m}_{12} \\ -\sin\Theta \mathrm{m}_{21} & \cos\Theta \mathrm{m}_{22} \end{bmatrix} \tag{A.37}$$

where $\mathrm{m_{ij}}$ are 2×2 matrices given by:

$$\mathrm{m_{ij}} = \begin{bmatrix} (1+\frac{k_1^{s_1}}{k_2^{s_2}})e^{-\mathrm{i}(k_1^{s_1}-k_2^{s_2})z}e^{-(k_1^{s_1}-k_2^{s_2})^2\frac{\sigma^2}{2}} & (1-\frac{k_1^{s_1}}{k_2^{s_2}})e^{\mathrm{i}(k_1^{s_1}+k_2^{s_2})z}e^{-(k_1^{s_1}+k_2^{s_2})^2\frac{\sigma^2}{2}} \\ (1-\frac{k_1^{s_1}}{k_2^{s_2}})e^{-\mathrm{i}(k_1^{s_1}+k_2^{s_2})z}e^{-(k_1^{s_1}+k_2^{s_2})^2\frac{\sigma^2}{2}} & (1+\frac{k_1^{s_1}}{k_2^{s_2}})e^{\mathrm{i}(k_1^{s_1}-k_2^{s_2})z}e^{-(k_1^{s_1}-k_2^{s_2})^2\frac{\sigma^2}{2}} \end{bmatrix} \tag{A.38}$$

where s_i represents + or −. For
m_{11}, $s_1 = +$, $s_2 = +$;
m_{12}, $s_1 = -$, $s_2 = +$;
m_{21}, $s_1 = +$, $s_2 = -$;
m_{22}, $s_1 = -$, $s_2 = -$.

The total transfer matrix ($\mathrm{M_{total}}$) of a stratified film is the product of the matrices of all interfaces. For incident spin-up neutrons, the incident, reflected and transmitted components at top and bottom are given as,

$$\begin{bmatrix} 1 \\ r^{++} \\ 0 \\ r^{+-} \end{bmatrix} = \mathrm{M_{total}} \begin{bmatrix} t^{++} \\ 0 \\ t^{+-} \\ 0 \end{bmatrix}. \tag{A.39}$$

Similarly, for incident spin-down neutrons

$$\begin{bmatrix} 0 \\ r^{-+} \\ 1 \\ r^{--} \end{bmatrix} = \mathrm{M_{total}} \begin{bmatrix} t^{-+} \\ 0 \\ t^{--} \\ 0 \end{bmatrix}. \tag{A.40}$$

So we have

$$
\begin{aligned}
r^{++} &= (\mathrm{m}_{21}\mathrm{m}_{33} - \mathrm{m}_{23}\mathrm{m}_{31})/(\mathrm{m}_{11}\mathrm{m}_{33} - \mathrm{m}_{13}\mathrm{m}_{31}), && \text{(A.41)}\\
r^{+-} &= (\mathrm{m}_{41}\mathrm{m}_{33} - \mathrm{m}_{43}\mathrm{m}_{31})/(\mathrm{m}_{11}\mathrm{m}_{33} - \mathrm{m}_{13}\mathrm{m}_{31}), && \text{(A.42)}\\
r^{--} &= (\mathrm{m}_{43}\mathrm{m}_{11} - \mathrm{m}_{41}\mathrm{m}_{13})/(\mathrm{m}_{11}\mathrm{m}_{33} - \mathrm{m}_{13}\mathrm{m}_{31}), && \text{(A.43)}\\
r^{-+} &= (\mathrm{m}_{23}\mathrm{m}_{11} - \mathrm{m}_{21}\mathrm{m}_{13})/(\mathrm{m}_{11}\mathrm{m}_{33} - \mathrm{m}_{13}\mathrm{m}_{31}), && \text{(A.44)}
\end{aligned}
$$

The spin dependent reflectivities can be calculated using $\mathrm{R} = |r|^2$. It can also be shown that $|r^{+-}|^2 = |r^{-+}|^2$, so that $\mathrm{R}^{+-} = \mathrm{R}^{-+}$. In the special case that the magnetic moment is in the same direction as that of the incident spin of the neutrons, $\sin(\Theta) = 0$, r^{+-} and r^{-+} vanish. The 4×4 transfer matrix A.37 can be broken into two 2×2 matrices, and Eqn. (A.39) and Eqn. (A.40) can be reduced to Eqn. (A.20) for spin-up and down neutrons respectively.

BIBLIOGRAPHY

[1] J. M. Murduck, D. W. Capone II, I. K. Schuller, S. Foner, and J. B. Ketterson. *Appl. Phys. Lett.*, 52:504, 1988.

[2] E. Spiller. *Physics, Fabrication and Applications of Multilayered Structures*, edited by P. Dhez and C. Weisbuch, Plenum, New York, 1988, p. 271.

[3] F. Mezei. *Physics, Fabrication and Applications of Multilayered Structures*, edited by P. Dhez and C. Weisbuch, Plenum, New York, 1988, p. 310.

[4] S. Hashimoto and Y. Ochiai. *J. Magn. Magn. Mater.*, 88:211, 1990.

[5] M. N. Baibich, J. M. Broto, A. Fert, F. Nguyen Van Dau, and F. Petroff. *Phys. Rev. Lett.*, 61:2472, 1988.

[6] S. Ohnishi, A. J. Freeman, and M. Weinert. *Phys. Rev. B*, 28:6741, 1983.

[7] E. Wimmer, A. J. Freeman, and H. Krakauer. *Phys. Rev. B*, 30:3113, 1984.

[8] C. L. Fu and A. J. Freeman. *J. Magn. Magn. Mater.*, 69:L1, 1987.

[9] F. R. de Boer, R. Boom, W. C. M. Mattens, A. R. Miedema, and A. K. Niesse. *Cohesion in Metals.* North-Holland, Amsterdam, 1988.

[10] H. C. Snyman and G. H. Olsen. *J. Appl. Phys.*, 44:889, 1973.

[11] B. T. Jonker and G. A. Prinz. *Surf. Sci.*, 172:L568, 1986.

[12] B. T. Jonker, K. H. Walker, E. Kisker, G. A. Prinz, and C. Carbone. *Phys. Rev. Lett.*, 57:142, 1986.

[13] C. L. Fu, A. J. Freeman, and T. Oguchi. *Phys. Rev. Lett.*, 54:2700, 1985.

[14] R. Richter, J. G. Gay, and J. R. Smith. *Phys. Rev. Lett.*, 54:2704, 1985.

[15] J. A. C. Bland, C. Daboo, B. Heinrich, Z. Celinski, and R. D. Bateson. *Phys. Rev. B*, 51:258, 1995.

[16] C. L. Wooten, J. Chen, G. A. Mulhollan, J. L. Erskine, and J. T. Markert. *Phys. Rev. B*, 49:10023, 1994.

[17] S. Ohnishi, M. Weinert, and A. J. Freeman. *Phys. Rev. B*, 30:36, 1984.

[18] S. C. Hong, A. J. Freeman, and C. L. Fu. *Phys. Rev. B*, 38:12156, 1988.

[19] G. Lugert and G. Bayreuther. *Phys. Rev. B*, 38:11068, 1988.

[20] H. J. Elmers, G. Liu, and U. Gradmann. *Phys. Rev. Lett.*, 63:566, 1989.

[21] N. F. Berk and J. R. Schrieffer. *Phys. Rev. Lett.*, 17:433, 1966; S. Doniach and S. Engelsberg, *Phys. Rev. Lett.*, 17:750, 1966; J. R. Schrieffer, *J. Appl. Phys.*, 39:642, 1968.

[22] F. M. Mueller, A. J. Freeman, J. O. Dimmock, and A. M. Furdyna. *Phys. Rev. B*, 1:4617, 1970.

[23] F. E. Hoare and J. C. Matthews. *Proc. Roy. Soc. (London)*, A212:137, 1952; D. W. Budworth, F. E. Hoare and J. Preston, *Proc. Roy. Soc. (London)*, A257:250, 1960; A. J. Manuel and J. M. P. St Quinton, *Proc. Roy. Soc. (London)*, A273:412, 1963.

[24] L. Fritsche, J. Noffke, and H. Eckardt. *J. Phys. F: Met. Phys.*, 17:943, 1987.

[25] V. L. Moruzzi and P. M. Marcus. *Phys. Rev. B*, 39:471, 1989.

[26] H. Chen, N. E. Brener, and J. Callaway. *Phys. Rev. B*, 40:1443, 1989.

[27] M. B. Brodsky. *J. Magn. Magn. Mater.*, 35:99, 1983.

[28] R. L. Fink, C. A. Ballentine, J. L. Erskine, and J. A. Araya-Pochet. *Phys. Rev. B*, 41:10175, 1990.

[29] C. Liu and S. D. Bader. *Phys. Rev. B*, 44:12062, 1991.

[30] J. Crangle. *Phil. Mag.*, 5:335, 1960.

[31] R. M. Bozorth, P. A. Wolff, D. D. Davis, V. B. Compton, and J. H. Wernick. *Phys. Rev.*, 122:1157, 1961.

[32] J. Crangle and W. R. Scott. *J. Appl. Phys.*, 36:921, 1965.

[33] G. J. Nieuwenhuys. *Phys. Lett.*, 43A:301, 1973.

[34] F. W. Constant. *Phys. Rev.*, 36:1654, 1930.

[35] A. M. Clogston, B. T. Matthias, M. Peter, H. J. Williams, E. Corenzwit, and R. C. Sherwood. *Phys. Rev.*, 125:541, 1962.

[36] P. P. Craig, D. E. Nagle, W. A. Steyert, and R. D. Taylor. *Phys. Rev. Lett.*, 9:12, 1962.

[37] G. J. Nieuwenhuys. *Adv. Phys.*, 24:515, 1975.

[38] J. W. Cable, E. O. Woollan, and W. C. Koehler. *J. Appl. Phys.*, 34:1189, 1963.

[39] G. G. Low and T. M. Holden. *Proc. Phys. Soc.*, 89:119, 1966.

[40] M. F. Collins and G. G. Low. *Proc. Phys. Soc.*, 86:535, 1965.

[41] J. W. Cable, E. O. Woollan W. C. Koehler, and M. K. Wilkinson. *J. Appl. Phys.*, 33:1340, 1962.

[42] T. J. Hicks, G. G. Low, and T. M. Holden. *J. Phys. C*, 1:528, 1968.

[43] G. G. Low. *Adv. Phys.*, 18:371, 1969.

[44] B. H. Verbeek, G. J. Nieuwenhuys, and J. A. Mydosh. *Phys. Rev. B*, 22:5426, 1980.

[45] J. C. Ododo. *J. Phys. F: Met. Phys.*, 15:941, 1985.

[46] A. Oswald, R. Zeller, and P. H. Dederichs. *Phys. Rev. Lett.*, 56:1419, 1986.

[47] G. Bergmann. *Phys. Rev. B*, 23:3805, 1981.

[48] C. Liu and S. D. Bader. *Physica*, 161B:253, 1989.

[49] B. Hillebrands, A. Boufelfel, C. M. Falco, P. Baumgart, G. Gntherodt, E. Zirngiebl, and J. D. Thompson. *J. Appl. Phys.*, 63:3880, 1988.

[50] W. Weber, D. A. Wesner, G. Güntherodt, and U. Linke. *Phys. Rev. Lett.*, 66:942, 1991.

[51] O. Rader, C. Carbone, W. Clemens, E. Vescovo, S. Blgel, and W. Eberhardt. *Phys. Rev. B*, 45:13823, 1992.

[52] Z. Celinski, B. Heinrich, J. F. Cochran, W. B. Muir, A. S. Arrott, and J. Kirschner. *Phys. Rev. Lett.*, 65:1156, 1990.

[53] J. R. Childress, R. Kergoat, O. Durand, J. M. George, P. Galtier, J. Miltat, and A. Schuhl. *J. Magn. Magn. Mater.*, 130:13, 1994.

[54] E. E. Fullerton, D. Stoeffler, K. Ounadjel, B. Heinrich, Z. Celinski, and J. A. C. Bland. *Phys. Rev. B*, 51:6364, 1995.

[55] J. Vogel, A. Fontaine, V. Cros, F. Petroff, J. P. Kappler, G. Krill, A. Rogalev, and J. Goulon. *Phys. Rev. B*, 55:3663, 1997.

[56] S. Blügel, B. Drittler, R. Zeller, and P.H. Dederichs. *Appl. Phys. A, Solids Surf.*, A49:547, 1989.

[57] H. Nait-Laziz, S. Bouarab, C. Demangeat, A. Mokrani, and H. Dreysse. *J. Magn. Magn. Mater.*, 118:365, 1993.

[58] H. Huang, J. Hermanson, J.G. Gay, R. Richter, and J.R. Smith. *Surf. Sci.*, 172:363, 1986.

[59] D. Stoeffler, K. Ounadjela, J. Sticht, and F. Gautier. *Phys. Rev. B*, 49:299, 1994.

[60] X. Le Cann, C. Boeglin, B. Carrière, and K. Hricovini. *Phys. Rev. B*, 54:373, 1996.

[61] B. T. Thole, P. Carra, F. Sette, and G. van der Laan. *Phys. Rev. Lett.*, 68:1943, 1992; P. Carra, B. T. Thole, Massimo Altarelli and Xindong Wang, *Phys. Rev. Lett.*, 70:694, 1993.

[62] W. L. O'Brien and B. P. Tonner. *Phys. Rev. B*, 50:12672, 1994.

[63] C. J. Gorter. *Paramagnetic Relaxation.* Elsevier Phublishing Co., New York, 1947.

[64] K. J. Duff and T. P. Das. *Phys. Rev. B*, 3:192, 1971.

[65] M. B. Stearn. *Physica*, 92 B+C:37, 1977.

[66] J. Tersoff and L. M. Falicov. *Phys. Rev. B*, 26:6186, 1982.

[67] J. J. Vuillemin and M. G. Priestley. *Phys. Rev. Lett.*, 14:307, 1965; J. J. Vuillemin, *Phys. Rev.*, 144:396, 1966.

[68] N. Takano, T. Kai, K. Shiiki, and F. Terasaki. *Solid State Commun.*, 97:153, 1996.

[69] M. Born and E. Wolf. *Principles of Optics.* Pergamon, Oxford, 1964.

[70] B. Vidal and P. Vincent. *Applied Optics*, 23:1794, 1984.

[71] E. E. Fullerton, I. K. Schuller, H. Vanderstraeten, and Y. Bruynseraede. *Phys. Rev. B*, 45:9292, 1992.

[72] X. L. Zhou and S. H. Chen. *Physics Reports*, 257:223, 1995.

[73] Jean Daillant and Alain Gibaud. *X-ray and neutron reflectivity: principles and application.* Springer, New York, 1999.

[74] C. F. Majkrzak, J. F. Ankner, N. F. Berk, and D. Gibbs. *Magnetic Multilayers*, edited by L. H. Bennett and R. E. Watson, World Scientific, Singapore, 1994.

[75] O. Schäpf. *Neutron Spin Echo*, edited by F. Mezei, Springer, Berlin, 1980.

[76] Philipp Gütlich, Rainer Link, and Alfred Trautwein. *Mössbauer Spectroscopy and Transition Metal Chemistry.* Springer-Verlag, Berlin Heidelberg New York, 1978.

[77] T. Shinjo. *Mössbauer spectroscopic studies on superlattices*, edited by T. Shinjo and T. Takada, Elsevier, New York, 1987.

[78] B. K. Agarwal. *X-ray Spectroscopy.* Springer, Berlin, 1979.

[79] D. G. Stearns. *J. Appl. Phys.*, 65:491, 1989.

[80] R. Abdouche. *Effect of ion beam irradiation on interfacial structure in bilayers.* PhD thesis, McGill University, August 2000.

[81] A. Boufelfel, R. M. Emrick, and C. M. Falco. *Phys. Rev. B*, 43:13152, 1991.

[82] C. J. Gutierrez, M. D. Wieczorek, H. Tang, Z. Q. Qiu, and J. C. Walker. *J. Magn. Magn. Mater.*, 99:215, 1991.

[83] D. J. Keavney, M. D. Wieczorek, D. F. Storm, and J. C. Walker. *J. Magn. Magn. Mater.*, 121:49, 1993.

[84] G. Liu and U. Gradmann. *J. Magn. Magn. Mater.*, 119:99, 1993.

[85] P. J. Schurer, Z. Celinski, and B. Heinrich. *Phys. Rev. B*, 48:2577, 1993.

[86] P. J. Schurer, Z. Celinski, and B. Heinrich. *Phys. Rev. B*, 51:2506, 1995.

[87] F. A. Volkening, B. T. Jonker, J. J. Krebs, N. C. Koon, and G. A. Prinz. *J. Appl. Phys.*, 63:3869, 1988.

[88] J. C. Walker, H. Tang, M. D. Wieczorek, D. J. Keavney, D. F. Storm, C. J. Gutierrez, and Z. Q. Qiu. *Hyperfine Interact.*, 68:271, 1992.

[89] H. Tang, M. D. Wieczorek, D. J. Keavney, D. F. Storm, and J. C. Walker. *J. Magn. Magn. Mater.*, 104-107:1705, 1992.

[90] A. J. Freeman and R. E. Watson. *Magnetism*, volume II A, edited by G. T. Rado and H. Suhl, Academic, New York, 1965.

[91] P. W. Anderson and A. M. Clogston. *Bull. Am. Phys. Soc.*, 6:124, 1961.

[92] P. H. Christensen and S. Mørup. *J. Magn. Magn. Mater.*, 35:130, 1983.

[93] G. Bayreuther. *Hyperfine Interac.*, 47:237, 1989.

[94] U. Gradmann. *J. Magn. Magn. Mater.*, 6:173, 1977.

[95] C. J. Gutierrez, Z. Q. Qiu, H. Tang, M. D. Wieczorek, S. H. Mayer, and J. C. Walker. *Phys. Rev. B*, 44:2190, 1991.

[96] C. J. Gutierrez, Z. Q. Qiu, M. D. Wieczorek, H. Tang, J. C. Walker, and R. C. Mercader. *Hyperfine Interac.*, 66:299, 1991; C. J. Gutierrez and Z. Q. Qiu and M. D. Wieczorek and H. Tang and J. C. Walker, *J. Magn. Magn. Mater.*, 93:326, 1991; C. J. Gutierrez and Z. Q. Qiu and M. D. Wieczorek and H. Tang and J. C. Walker, *J. Appl. Phys.*, 69:5283, 1991; J. C. Walker and Z. Q. Qiu and C. J. Gutierrez and M. D. Wieczorek and H. Tang, *J. Magn. Magn. Mater.*, 104-107:1703, 1992.

[97] Z. Q. Qiu, S. H. Mayer, C. J. Gutierrez, H. Tang, and J. C. Walker. *Phys. Rev. Lett.*, 63:1649, 1989.

[98] R. Kariotis. *J. Phys.*, A22:2781, 1989.

[99] D.G. Stearns, R. S. Rosen, and S. P. Vernon. *J. Vac. Sci. Technol.*, A9:2662, 1991.

[100] M. B. Stearns, C. Chang, and D. G. Stearns. *J. Appl. Phys.*, 71:187, 1992.

[101] M. Li, X.D. Ma, C. B. Peng, J. G. Zhao, L.M. Mei, Y. S. Gu, W. P. Chai, Z. H. Mai, B. G. Shen, Y. H. Liu, and D. S. Dai. *Phys. Rev. B*, 50:10323, 1994.

[102] J. Thomassen, F. May, B. Feldmann, M. Wuttig, and H. Ibach. *Phys. Rev. Lett.*, 69:3831, 1992.

[103] Dongqi Li, M. Freitag, J. Pearson, Z. Q. Qiu, and S. D. Bader. *Phys. Rev. Lett.*, 72:3112, 1994.

[104] S. Müller, P. Bayer, C. Reischl, and K. Heinz. *Phys. Rev. Lett.*, 74:765, 1995.

[105] C. Liu and S. D. Bader. *J. Appl. Phys.*, 67:5758, 1990.

[106] M. T. Johnson, P. J. H. Bloemen, F. J. A. den Broeder, and J. J de Vries. *Rep. Prog. Phys.*, 59:1409, 1996.

[107] C. Liu and S. D. Bader. *Phys. Rev. B*, 44:2205, 1991.

[108] C. Boeglin, H. Bulou, J. Hommet, X. Le Cann, H. Magnan, P. Le Fèvre, and D. Chandesris. *Phys. Rev. B*, 60:4220, 1999.

[109] N. Hosoito, T. Shinjo, and T. Takada. *J. Phys. Soc. Jpn.*, 50:1903, 1981.

[110] C. Binns, C. Norris, Gwyn P. Williams, M. G. Barthes, and H. A. Padmore. *Phys. Rev. B*, 34:8221, 1986.

[111] J. Quinn, Y. S. Li, H. Li, D. Tian, F. Jona, and P. M. Marcus. *Phys. Rev. B*, 43:3959, 1991.

[112] R. Ingalls, F. Van der Woude, and G. A. Sawatzky. *Mössbauer Isomer Shifts*, chapter 7, page 365. Edited by G. K. Shenoy and F. E. Wagner, North-Holland Pub. Co., Amsterdam;New York, 1978.

[113] F. Bloch. *Z. Physik*, 61:206, 1930.

[114] M. J. Klein and R. S. Smith. *Phys. Rev.*, 81:378, 1951.

[115] R. S. Smith and M. J. Klein. *Phys. Rev.*, 109:288, 1958.

[116] A. Corciovei. *J. Phys. Chem. Solids*, 20:162, 1961.

[117] W. Döring. *Z. Natrforschung*, 16a:1008;1146, 1961.

[118] G. T. Rado. *Bull. Am. Phys. Soc.*, 2:127, 1957.

[119] J. Mathon. *Phys. Rev. B*, 34:1775, 1986.

[120] D. W. Lee, D. H. Ryan, Z. Altounian, and A. Kuprin. *Phys. Rev. B*, 59:7001, 1998.

[121] S. S. P. Parkin, N. More, and K. P. Roche. *Phys. Rev. Lett.*, 64:2304, 1990.

[122] S. S. P. Parkin. *Phys. Rev. Lett.*, 67:3598, 1991.

[123] Z. Shi and B. M. Klein. *Phys. Rev. B*, 52:12516, 1995.

[124] J. Wang, Y. J. Wang, J. Li, and T. Zhu. *Phys. Rev. B*, 59:11866, 1999.

[125] Z. Celinski, B. Heinrich, and J. F. Cochran. *J. Appl. Phys.*, 70:5870, 1991.

[126] R. J. Hicken, A. J. R. Ives, D. E. P. Eley, C. Daboo, and J. A. C. Bland. *Phys. Rev. B*, 50:6143, 1994.

[127] H. Yamamoto, T. Okuyama, H. Dohnomae, and T. Shinjo. *J. Magn. Magn. Mater.*, 99:243, 1991.

[128] Y.-P. Zhao, R. M. Gamache, G.-C. Wang, T.-M. Lu, G. Palasantzas, and J. Th. M. De Hosson. *J. Appl. Phys.*, 89:1325, 2001.

[129] V. I. Malyutin, V. E. Osukhovskii, Y. D. Vorobiev, A. G. Shishkov, and V. V. Yudin. *Phys. Status Solidi A*, 65:45, 1981.

[130] S. Z. Wu, G. J. Mankey, F. Huang, and R. F. Willis. *J. Appl. Phys.*, 76:6434, 1994.

[131] Q. Jiang, H.-N Yang, and G.-C Wang. *Surf. Sci.*, 373:181, 1997.

[132] Y. Wang, P. M. Levy, and J. L. Fry. *Phys. Rev. Lett.*, 65:2732, 1990.

[133] J. A. Borchers, J. F. Ankers, C. F. Majkzak, B. N. Engel, M. H. Wiedermann, R. A. van Leeuwen, and C. M. Falco. *J. Appl. Phys.*, page 6498, 1994.